Faculty of Electrical Engineering
Department of Radioelectronics

Doctoral Thesis
Detection of X-ray radiation in vacuum

Ing. Martin Urban

Prague, March 2023

ACKNOWLEDGEMENT

COPYRIGHT

ABSTRACT

The detection of X-rays is crucial to studying and understanding many astrophysical phenomena. However, the Earth's atmosphere significantly attenuates this type of radiation, so measurements must be made in Earth's orbit. This approach involves challenging conditions such as increased radiation, vacuum condition and extreme temperature changes. This thesis focuses on the effect of changing these conditions on the accuracy of radiation measurements using hybrid pixel detectors. These detectors have proven their capability on several space missions and have significant application potential.

Particular emphasis is placed on investigating the effect of temperature on measurement accuracy in different measurement modes, especially the impact on the detection of the energy of the incident X-ray radiation. The results are verified and validated in a thermal vacuum chamber. This thesis addresses the measurement principles, description and characterisation of the identified distortions in the energy spectra. In addition, two unique compensation methods are proposed that minimise the described temperature effects and thus provide accurate measurements over a wide temperature range. Finally, the possibility of generalising and extrapolating the proposed correction model is presented and verified.

The results of this research are relevant to further scientific and industrial applications of this type of detector and are already being used in the preparation of future space missions. This work provides valuable information and will help to improve the accuracy of X-ray measurements.

KEYWORDS

X-ray Detector, Ionizing Radiation, Thermal Distortion, Compensation, Space Missions

ANOTACE

Detekce rentgenového záření je klíčová pro výzkum a pochopení mnoha astrofyzikálních jevů, avšak zemská atmosféra značně absorbuje tuto formu záření, což vyžaduje provádění měření na oběžné dráze Země. Tento postup obnáší náročné podmínky, jako je zvýšená radiace, vakuum a extrémní změny teploty. Tato práce se zaměřuje na vliv změny těchto podmínek na přesnost radiačního měření pomocí hybridních pixelových detektorů. Tyto detektory prokázaly svou účinnost během několika vesmírných misí a mají významný aplikační potenciál.

Zvláštní důraz je kladen na výzkum vlivu teploty na přesnost měření, v různých měřicích režimech, zejména s cílem určit vliv na přesnost detekce energie dopadajícího rentgenového záření. Výsledky jsou ověřovány a validovány v termovakuové komoře. Tato práce zahrnuje principy měření, popis a charakterizaci zjištěných zkreslení energetických spekter. Dále jsou navrženy dvě unikátní metody kompenzace, které minimalizují popsané teplotní vlivy a umožní tak přesné měření v širokém teplotním rozsahu. V neposlední řade je ověřena i možnost zobecnění a extrapolování navrženého korekčního modelu.

Výstupy této studie jsou již využívány při přípravě budoucích vesmírných misí a mají význam pro další vědecké a průmyslové aplikace tohoto typu detektorů. Tato práce poskytuje cenné informace a pomůže zlepšit přesnost měření v oblasti rentgenového záření.

KLÍČOVÁ SLOVA

Rentgenový Detektor, Ionizující Záření, Tepelné Zkreslení, Kompenzace, Vesmírné Mise

Contents

List of Abbreviations

ADC . . . . analogue-to-digital converter
ASIC . . . . application-secific integrated circuit
BAT . . . . Burst Alert Telescope
CdTe . . . . Cadmium Telluride
CERN . . . . Conseil Européen pour la recherche nucléaire
CSA . . . . charge-sensitive amplifier
CTU . . . . Czech Technical University in Prague
EC . . . . Event counting
eROSITA . . . . extended ROentgen Survey with an Imaging Telescope Array
GaAs . . . . Gallium Arsenide
GRB . . . . gamma–ray burst
ISS . . . . International Space Station
LEO. . . . . low Earth orbit
MSL . . . . Mars Science Laboratory
Si . . . . Silicon
THL . . . . threshold
ToA . . . . Time-of-Arrival
ToT . . . . Time-over-Threshold
TPX3. . . . . Timepix3
TRL . . . . Technology Readiness Level
UWB . . . . University of West Bohemia
VZLU . . . . Czech Aerospace Research Centre
X–ray. . . . . X–radiation
XMM–Newton . . . . X–ray Multi–Mirror
XPS. . . . . X–ray photoelectron spectroscopy
XRD . . . . X–ray diffraction
XRF . . . . X–ray fluorescence
XRT . . . . X–ray Telescope

Chapter 1
Introduction

The measurement of X–radiations (X–rays) is a critical technique used in many scientific and industrial applications, as well as in the field of space exploration, where high-precision analysis of radiation fields, materials and structures is required. X–rays are widely used because of their ability to penetrate materials, provide high-resolution images of their internal structure and identify the types of materials/elements present. However, X–ray can be affected by scattering from air molecules, resulting in reduced accuracy and resolution. Therefore, X–ray measurements are often performed in a vacuum environment to minimise these effects.

X–ray photoelectron spectroscopy (XPS), X–ray diffraction (XRD) and X–ray fluorescence (XRF) are among the scientific and industrial applications of X–ray measurements. XPS is used to analyse the chemical composition of a material by measuring the energies of photoelectrons emitted when the material is exposed to X–rays. XRD is used to study the structure of materials by measuring the angles and intensities of X–rays diffracted by the material. Finally, XRF is used to identify individual elements.

In space, X–ray measurements are used, for example, to study the composition and structure of planetary bodies, to monitor solar activity, and to investigate the properties of radiation fields or interstellar bodies. One scientific example is the Mars Science Laboratory (MSL) mission, which includes the Curiosity rover [1]. The rover is designed to study the geological and environmental history of Mars [2], based not only on precise XRD analysis on board the rover [3].

On the other hand, X–ray telescopes are used for the observation and remote study of X–ray phenomena in space, such as various galactic and extragalactic X–ray sources, supernova outbursts, X–ray afterglows of gamma–ray bursts (GRBs) and solar flares. However, the Earth's atmosphere attenuates the radiation from these phenomena, making it difficult to accurately determine their parameters and properties. Therefore, X–ray telescopes need to be placed above the Earth's atmosphere to overcome this problem and allow more precise monitoring and analysis of X–ray phenomena. Several satellites have been launched for this purpose, including Chandra, X–ray Multi–Mirror (XMM–Newton) and extended ROentgen Survey with an Imaging Telescope Array (eROSITA) [4] or Swift, which consists of three instruments onboard, like X–ray Telescope (XRT) [5] and Burst Alert Telescope (BAT) [6]. Most of these missions use a CCD with a cooling system for thermal stabilisation and to improve detection characteristics such as thermal noise and spectral resolution.

The development and miniaturisation of X–ray measurement systems have made it possible to use the small CubeStats platform for space applications. One of these is the VZLUSAT-1 CubeSat [7, 8], which now operates in low Earth orbit for 6 years. CubeSats are standardised and small in size, typically a cube 10 cm on each side, stackable and weighing from a few hundred grams to a few kilograms. The standardised design of CubeSats makes them more accessible and cheaper to produce, making them a popular choice for universities, research organisations and commercial companies. They can be used for a variety of purposes, including Earth observation, scientific research, technology demonstration and even interplanetary missions. Despite their small size, CubeSats have huge potential to provide a platform for Earth observation, atmospheric research and space exploration.

Due to the specific requirements and characteristics of X–ray measurements in space, different approaches are required compared to standard ground-based laboratory measurements. System design specifications impose significant constraints on size, weight and power consumption due to the limitations on spacecraft and satellites. On-board systems must have robust mechanical strength and thermal stability to minimise temperature distortion caused, for example, by thermal cycling along the orbit.

Fig. 1.1: Illustration of outcomes of the thesis author's activities: X-ray measurements and thermal vacuum tests, as well as participating in and preparing space campaigns for radiation measurements.

This thesis presents the results of a study investigating the usage of position sensitive semiconductor detectors, specifically the Timepix3 (TPX3) type, for X-ray applications, with a primary focus on space research. The Timepix detector, which preceded the TPX3, was successfully deployed as a payload on the VZLUSAT-1 CubeSat. It is worth noting that this nanosatellite (as well as the detector) exceeded its expected operational lifetime by several years and that the author of this thesis was also involved in the design, commissioning, and testing of the spacecraft.

The introduction covers the basic principles of detection and the interaction of X–rays with matter, as well as the most common applications of X–rays in measurement and scientific research.

The subsequent chapters deal with the **research objectives of this thesis**, including the challenges related to the influence of environmental conditions on the accuracy of the results. The research findings have been published and selected papers form part of this thesis, the full list of authors' publications can be found in Appendix A.1.

The feasibility study of X–ray measurements with hybrid pixel detectors in a vacuum includes an investigation of the effect of temperature distortion and an analysis of the effect of temperature cycling on the properties of the detection system. Thermal distortion is a significant challenge in space applications due to the self-heating of the instrument, other parts of the spacecraft, and radiation from the Sun and other celestial sources with limited heat dissipation capabilities. The study identified significant data distortion after initial tests of the detection capability of the TPX3 detector under varying temperature conditions (see section 3.1) [9, 10].

Analysis and description of the effect of temperature cycling on the performance of the detection system. In order to carry out a detailed analysis, it was necessary to assemble a test set in order to obtain demonstrable results using different samples. This was followed by a series of further tests involving measurements with a variety of radiation sources, including characteristic XRF radiation and additional natural sources. The tests were carried out over a temperature range of $-40\,^\circ$C to $70\,^\circ$C, based on a combination of previous space project experience as well as space agency standards and construction capabilities. Independent tests investigated the behaviour of the detector in different measurement modes (see chapter 3). A drift in the measured energy spectra of the radiation was observed as a function of the magnitude of the incident energy radiation and the temperature cycle. This distortion can adversely affect measurement accuracy, increasing the relative measurement error by up to $30\,\%$ (sections 3.2 and 3.3) [11, 12].

Methods for characterising the detected effects and their compensating were investigated. Several compensation models have been proposed to suppress the introduced measurement errors. The presented methods allow to reduce the relative error of incident energy measurement to about $1\,\%$ over the whole energy range of tested sources, up to $100\,$keV. This reduction of the measurement error is significant, and even within a temperature drift of $-40\,^\circ$C to $80\,^\circ$C, a final measurement accuracy of about $99\,\%$ can be maintained [12, 13] (see section 3.3). Furthermore, achieving this level of accuracy eliminates the need for additional detector calibrations or the implementation of power/size/weight consuming additional cooling systems or thermal stabilisation of the detection system. In addition to these benefits, the compact size of the detector now provides opportunities for its use in a wide range of scientific applications and industries, increasing the potential of this type of detector in other fields and reducing the need for extensive calibration series and power sources for thermal stabilisation/cooling.

Applicability of detectors for space missions. Last but not least, there are several space missions that are already using or plan to use the Timepix/Timepix3 detectors on board [7, 14–16]. During these missions, the detectors are exposed to hostile environmental conditions (vacuum, radiation, temperature) that can significantly affect their functionality and accuracy. It is, therefore, necessary to study the system's behaviour under such conditions and their possible changes. Three mission examples are given in this section. A CubeSat and a sounding rocket have already been launched. From the data obtained, conclusions can be drawn about the conditions to which the detectors were exposed (rocket) or are still exposed (CubeSat). In addition, there is a planned mission that will carry a number of Timepix3 detectors on board. The detectors dedicated to this mission have a customised design and have already been tested and calibrated with respect to the research results presented in this thesis.

Chapter 2
X-ray interaction with matter

The interaction of X–radiation with matter is a fundamental aspect of X–ray science and detection technology. X–rays are high-energy electromagnetic waves that can penetrate matter, and their interaction with matter can lead to a variety of phenomena. The ability of X–rays to penetrate matter depends on their energy and the atomic and molecular structure of the matter they encounter.
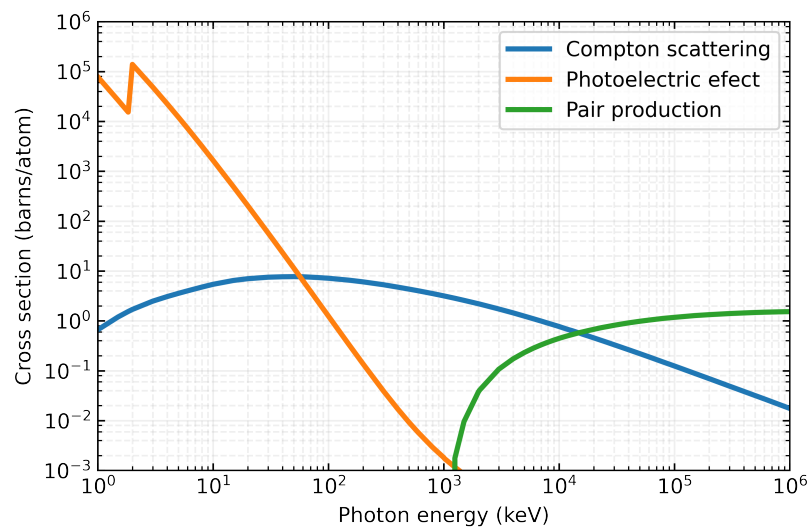

Fig. 2.2: Cross section of Silicon on and its contributions from photoelectric effect, Compton scattering and electron-positron pair production. The chart is based on the XCOM database [17].

One way of understanding the interaction of X–rays with matter is to examine the cross-section of a material, which represents the probability of an X–ray interacting with an atom or molecule as it passes through the material. Figure 2.2 shows an example of the cross-section of silicon as a function of X–ray energy. At low energies, X–rays are mainly absorbed by the photoelectric effect, in which an X–ray photon is absorbed by an inner-shell electron, causing it to be ejected from the atom. At higher energies, X–rays can also be scattered by the electrons in the material, either by Compton scattering. In addition, at very high energies, X–rays can interact with the atomic nucleus, resulting in the production of electron-positron pairs.

There are a large number of known interaction mechanisms, but these three main types, the photoelectric effect, Compton scattering and pair production, play an important role in the processes of interaction with matter and X–ray measurement. These effects are described in the following sections.

2.1 Photoelectric effect

The photoelectric effect is a process in which X–rays interact with matter, causing an electron to be ejected from an atomic shell. This process occurs when an X–ray photon with an energy greater than the binding energy of an electron in the atomic shell is absorbed. The absorbed photon transfers all of its energy to the electron, causing it to be ejected from the atom with a kinetic energy equal to the difference between the photon energy E_γ and the binding energy E_b of the electron. An electron ejected in this way is called a photoelectron with energy E_{e^-}

$$E_{e^-} = E_\gamma - E_b \tag{2.1}$$

where photon energy E_γ is

$$E_\gamma = h\nu = \frac{hc}{\lambda}, \tag{2.2}$$

$h \approx 4.136 \times 10^{-15}\,\mathrm{eV\,s}$ is Planck's constant, $c \approx 299.8 \times 10^6\,\mathrm{m/s}$ is the speed of light in vacuum, and the parameter of the photon is represented by the frequency ν or the wavelength λ of the radiation.

The vacancy in the shell of the ionised atom is immediately filled by the rearrangement of electrons from other shells and/or by the capture of free electrons from the medium. Rearrangement from other shells may result in one or more characteristic fluorescence photon emissions. If the vacancy is formed in one of the inner atomic shells, the characteristic X–ray photons can be re-absorbed, resulting in the release of the electron from the bound shell (Auger electrons) [18].
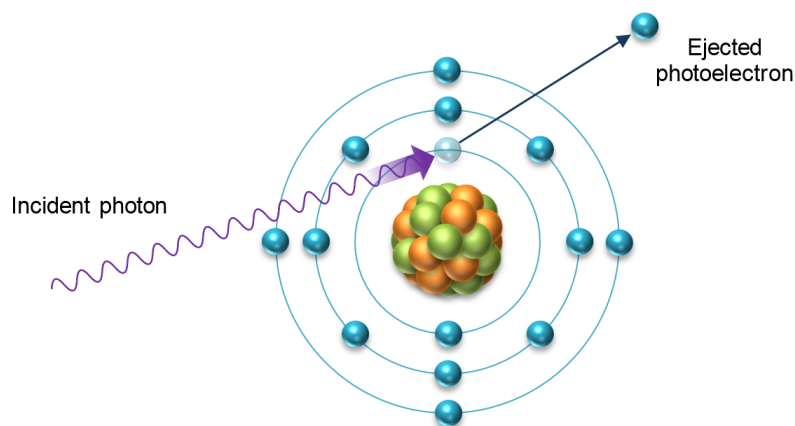

Fig. 2.3: The principle of the photoelectric effect [19].

The photoelectric effect is strongly dependent on the X–ray energy and the atomic number Z of the irradiated material. For X–ray energies up to $\approx 50\,\mathrm{keV}$, the photoelectric effect is the dominant mechanism of X–ray absorption in Silicon (Figure 2.2).

2.2 Compton scattering

Another type of interaction of X–ray photons with matter is Compton scattering. In this type of interaction, part of the photon's energy is transferred to the electron, causing a change in the direction and energy of the photon. Compton scattering occurs when an X–ray photon collides with an electron in the atomic shell, causing the electron, known as the recoiled electron, to be ejected and the photon to be scattered in a new direction. The scattered photon has a lower energy and therefore a longer wavelength than the original photon, while the recoiled electron has a kinetic energy E_e equal to the difference between the energy of the original photon E_γ and the energy of the scattered photon E_λ. The scattering angle θ and the energy shift of the scattered photon depend on the incident photon's energy and the angle between the incident photon and the direction of the ejected electron [18].

$$E_\lambda = \frac{E_\gamma}{1 + \frac{E_\gamma}{m_e c^2}(1 - \cos\theta)} = \frac{h\nu_\gamma}{1 + \frac{h\nu_\gamma}{m_e c^2}(1 - \cos\theta)} = h\nu_\lambda \tag{2.3}$$

Where $m_e c^2$ is the rest mass energy of the electron $(0.511\,\text{MeV})$ [18]. The kinetic energy of the recoil electron is therefore

$$E_e = E_\gamma - E_\lambda = \frac{E_\gamma^2 (\cos\theta - 1)}{E_\gamma (\cos\theta - 1) - m_e c^2} \tag{2.4}$$
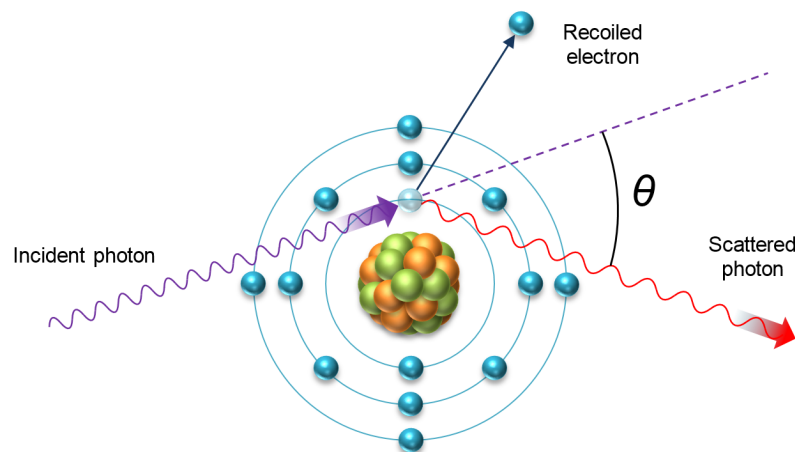

Fig. 2.4: Schematic representation of Compton scattering [19].

2.3 Pair production

The third significant gamma-ray interaction is pair production, the process by which high-energy photons, such as X–rays or gamma rays, interact with matter to produce an electron-positron pair. The process occurs when a photon with an energy at least two times greater than the rest mass energy of an electron ($\geq 2m_ec^2 \approx 1.022\,\text{MeV}$) interacts with an atomic nucleus. The photon is absorbed and its energy is converted into the kinetic energy of an electron-positron pair ($E_{e^-} + E_{e^+}$). When the energy of the positron becomes very low, the positron will annihilate or combine with a normal electron in the absorbing material and both particles will disappear. This produces two photons of energy, each of 511 keV. These annihilation photons can then interact further through processes such as Compton scattering or the photoelectric effect [18].

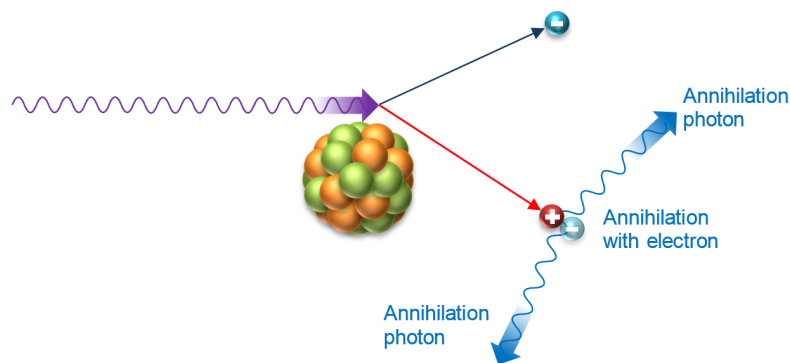$$E_{e^-} + E_{e^+} = E_\gamma - 2m_ec^2 \tag{2.5}$$

Fig. 2.5: Schematic representation of electron-positron pair production [19].

Chapter 3
Timepix3 detector

Timepix3 is a hybrid pixel detector based on the Medipix technology developed by Conseil Européen pour la recherche nucléaire (CERN) laboratories. This detector contains an array of 65 536 radiation-sensitive pixels arranged in a 256 px × 256 px sensor matrix with a pitch of 55 μm that detects particles such as electrons, photons and ions (Figure 3.6a).

Although the Timepix was originally developed for laboratory and scientific use [20], such as ATLAS [21], it has quickly found applications outside the laboratory environment. Its imaging capabilities [22, 23] have shown potential in medicine [24–27] and art [28], but also in X-ray inspection of materials and their joints, monitoring of the radiation environment and localisation of radioactive sources [29, 30].

Thanks to the hybrid structure of TPX3, different types of monolithic sensor layers such as Silicon (Si), Cadmium Telluride (CdTe) or Gallium Arsenide (GaAs) with different thicknesses can be integrated on the same TPX3 readout chip. The material used and its thickness typically ranges from 100 μm to 2 000 μm, depending on the application and its energy sensing range (Figure 3.7), but the thickness within the sensor is constant for manufacturing precision.

(a) Timepix3 chip[1]   (b) Schematic of one TPX3 pixel logic[2]
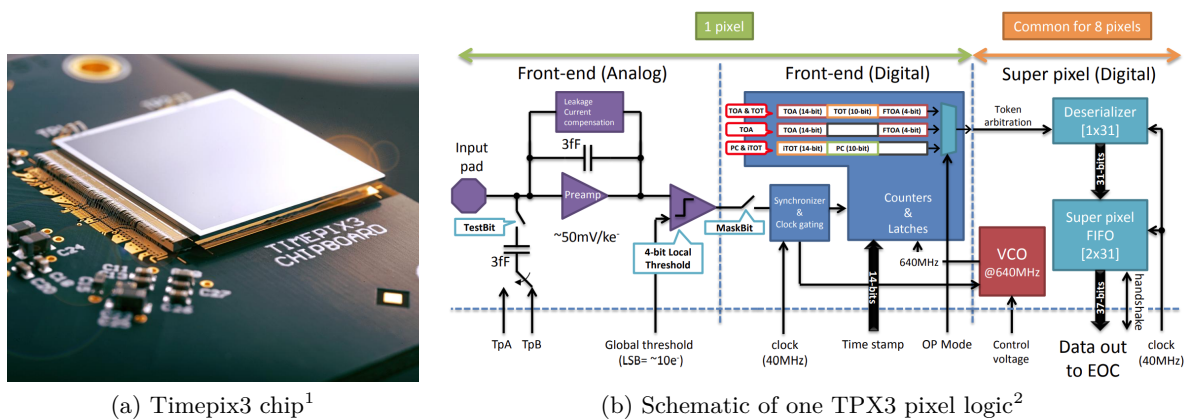
Fig. 3.6: Design of the Timepix3 detector.

An application-secific integrated circuit (ASIC) chip, onto which each of the pixels of the solid-state sensor is bump-bonded, contains the advanced sensing electronics of the detector. The signal electronics for each pixel, including a charge-sensitive amplifier (CSA), threshold discriminator, counters and a Wilkinson-type analogue-to-digital converter (ADC), are integrated within the ASIC chip. These components are contained in an analogue front-end which, together with the associated digital front-end, are individual for each pixel. The schematic of one pixel analogue and digital logic is shown in Figure 3.6b.

---

[1] "Timepix3" by *The Medipix3 Collaborations*
[2] "Pixel/SuperPixel diagram" by *Massimiliano De Gaspari*

Fig. 3.7: The detection efficiency of X–rays depends on the thickness and material of the sensor used.
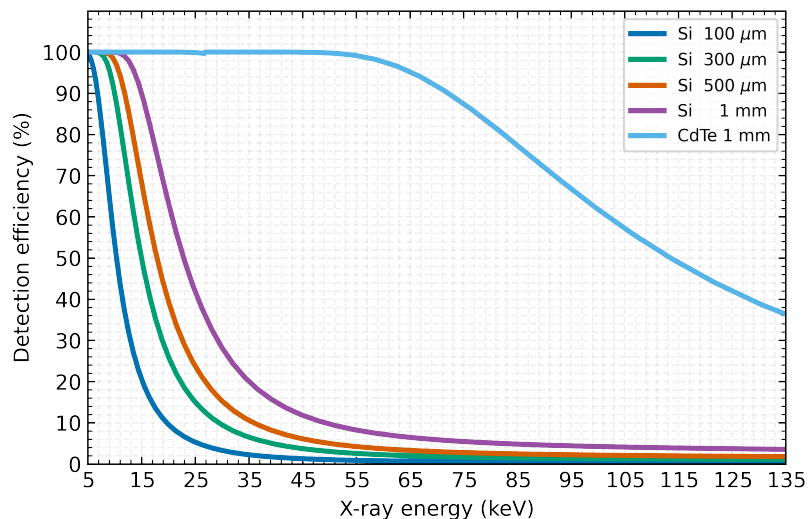
A significant advantage of a pixel detector with an integrated threshold (THL) discriminator is that the THL can be used to remove noise, allowing the detector to operate as an almost noise-free system. Assuming the detector has been calibrated and equalised correctly.

Unlike previous versions of Timepix detectors [31], which were only capable of reading data in Frame mode, where the signal value is read from all pixels at once after a set acquisition time, the Timepix3 can also read data in a method known as a Data-driven mode. This mode does not rely on a constant frequency and reads the signal from each individual pixel after exceeding the THL of the given pixel. A group of $2\,\mathrm{px} \times 4\,\mathrm{px}$ forms a so-called Super Pixel. This ensures the sequential reading of digital data from these 8 pixels. As a result, the global dead time for the whole detector is virtually zero with relatively short dead time per pixel, which is $\approx 475\,\mathrm{ns}$ [32]. Compared to the previous version of the detector, the output data stream is continuous and has a much better time resolution. Since only hit pixels are read out, the total amount of data is significantly lower. The radiation flux and occupancy matrix must be taken into account.

The TPX3 ASIC can operate all the $65\,536\,\mathrm{px}$ in one of the following modes:

Time-of-Arrival (ToA) - measurement of the particle impact time into the detector. That is, the time it takes to reach the THL level from the beginning of the exposure time.

Time-over-Threshold (ToT) & ToA - combination of simultaneous ToA and deposited energy measurements. The measurement of the deposited energy in a pixel from the incident particle is based on the Wilkinson-type ADC. The sensed energy depends on the number of clock ticks during which the signal is above the preset discrimination level (threshold). The Time-over-Threshold relies on the time (number of clock ticks) it takes to discharge the accumulated charge in each pixel by a constant current.

Event counting (EC) & integral ToT - the count of events and their integrated charge in each pixel during the common exposure time. Only events generating the charge above the discrimination level are sensed.

3.1   **Equalisation**

Pixelated radiation detectors consist of a large number of individual pixels, each of which records the energy deposited by a charged particle as it passes through the detector material. Due to manufacturing variations, amplifier gain differences or radiation damage effects, each pixel's response can vary, resulting in a non-uniform response across the array. This non-uniformity can lead to significant systematic errors in the measured data and limit the performance of the detector.

For this reason, the equalisation of the detection matrix is one of the first steps necessary for the correct operation of pixel detectors. Equalisation is a process used to correct these non-uniformities by adjusting the response of each pixel to be as uniform as possible. There are several different equalisation procedures, each consisting of a series of steps that can be performed with (signal equalisation) [33] or without (noise equalisation) [31] detector irradiation. This involves determining the response of each pixel to a reference source, such as a beam of monoenergetic particles, and applying correction factors to each pixel to ensure that they all respond equally to the same input. The aim of the equalisation is to ensure that the detector response is as uniform as possible across the pixel array, thereby improving the accuracy and precision of the measurements made with the detector. For this purpose, the Timepix3 detector has the ability to set a 4-bit THL adjustment for each pixel of the sensor matrix in the frame of the individual pixel electronics.

As part of the thermal vacuum tests, a series of equalisations and subsequent verifications were carried out over a temperature range of $-20\,°\text{C}$ to $80\,°\text{C}$, including comparison with a reference equalisation obtained at $20\,°\text{C}$.

No significant effect of the vacuum on the measurement results was observed during the tests. However, as the detector temperature increased, the global threshold had to be increased to suppress the noise in the matrix sufficiently. According to the verification, the distribution of equalised pixels across the detector gradually widens with both increasing and decreasing temperature, even at a difference of $10\,°\text{C}$. This can lead to further distortion of the sensed radiation [9, 10].

21ST INTERNATIONAL WORKSHOP ON RADIATION IMAGING DETECTORS
7–12 JULY 2019
CRETE, GREECE

Thermal vacuum testing of Timepix3 detector

M. Urban,[a,1] **D. Doubravova**[b] **and O. Nentvich**[a]

[a]*Czech Technical University in Prague, Faculty of Electrical Engineering,*
 Technicka 2, Prague, Czech Republic

[b]*Advacam, s.r.o.,*
 U Pergamenky 12, Prague, Czech Republic

 E-mail: martin-urban@fel.cvut.cz

ABSTRACT: The thermal dependence of semiconductor detectors is one of their critical properties. This paper presents the results of the Timepix3 detector thermal vacuum testing, with respect to the effects on its properties and sensitivity. The Timepix3 represents a new generation of Timepix chips of the Medipix family, and it is equipped with an event-based mode of detection allowing for simultaneous measurement of the position, time and energy of an incident particle. Due to their properties, Timepix3 detectors are very suitable for space applications.

Given that this is a relatively new device, the influence of temperature is not described in detail yet, especially for space usage. The operation of the device in a broad range of temperatures is required (e.q. QB50 mission on LEO from $-20°C$ to $+50°C$). Timepix detectors have been used already in space missions, e.g. VZLUSAT-1, LUCID and SATRAM missions. In space, thermal cycling of the detectors occurs and this results in measurement distortion because both the noise edge and energy spectra are affected by changes in temperature. The experiments were performed on a detector equipped with a $300\,\mu m$ thick Si sensor. The detector was equalised under various thermal conditions in vacuum and subsequently exposed to several energies of X-ray radiation corresponding to the characteristic radiation of 5 elements in the energy range of 4–24 keV. The results of these tests improve the knowledge regarding the behaviour of the essential components of the detector under extreme conditions. This new information can be used to improve measurements and thus minimise external influences, for example, in space applications but also in other fields where temperature stabilisation of the detector is very difficult or energy-consuming.

KEYWORDS: Detector cooling and thermo-stabilization; Solid state detectors; X-ray detectors

---

Corresponding author.

Contents

1 Introduction

Radiation measurement is important for a wide range of fields including security applications, medical applications and open space applications. In many of these applications, there are not ideal conditions for the operation of an X-ray detector. Space applications have some of the most challenging operating conditions due to the environment. However, these challenges are worth overcoming as the data obtained from X-ray detectors in space provides valuable scientific information.

Pixel detectors, which include the Timepix [1] family, provide information not only about the photon counts, but also the energy of the incident radiation. With these detectors, it is possible to attain additional information such as the shape of the trajectory of the impacted particle [2, 3]. Based on this and other information, it is possible to determine the type of an incident particle, its energy and thus classify its source. Accurate equalisation and calibration of the detector are essential for reliable detection and classification of particles and radiation.

Temperature stabilisation is very difficult and energy-consuming, especially in space because heat is not well dissipated in vacuum. As the detector is self-heating during its operation, this presents an issue as the detector noise edge and threshold is changing with temperature. Due to these issues, the measured results can be distorted and energy peaks will be spread out resulting in an inaccurate measurement. Other factors that heat the detector include when the detector is in orbit, or when it is exposed to unwanted radiation from nearby stars.

There are several satellites with Timepix based detectors on board. The SATRAM experiment is onboard of ESA's satellite Proba-V [4]. The following two missions exposed the Timepix detector to the open universe: Czech CubeSat VZLUSAT-1 [5–8], and the LUCID experiment onboard of British satellite TechDemoSat-1 [9, 10]. In these cases, thermal cycling of the detectors occurs. A summary of these and other related missions are available in [11].

The temperature condition of the CubeSat mission QB50 in the low Earth orbit (LEO), where was the VZLUSAT-1 nanosatellite part of, is from $-20°C$ to $+50°C$.

This manuscript presents the results of the thermal vacuum tests with the Timepix3 (a new generation of Timepix chips) detector equipped with a 300 μm thick Si sensor. Tests were performed under various thermal conditions from −20°C to +80°C in vacuum and exposed to X-ray characteristic radiation of 5 elements in the energy range of 4–24 keV.

1.1 Timepix3

The Timepix3 (TPX3) [12] is a hybrid pixel-particle-counting detector, which consists of a high-density matrix of 256 × 256 sensitive pixels with a pixel pitch of 55 μm. Thus the total sensitive area is 14.1 mm × 14.1 mm. This semiconductor detector is part of the Medipix family of chips. It consists of a semiconductor sensitive layer bump-bonded on the ASIC readout chip manufactured separately.

The important advantage of this design is the possibility to use a combination of different sensitive materials for the detection layer (Si, GaAs, CdTe, etc.) with the same readout chip. This layer is a monolithic piece of material with a common top bias electrode and a doped matrix at the bottom. The combination of materials with different thicknesses (from 100 μm up to 2000 μm) allow the change of the detection range according to the application.

The ASIC chip provides integrated signal electronics for each pixel, meaning that there is a charge sensitive preamplifier, threshold discriminator and a 14-bit counter for each pixel. This arrangement provides the possibility to operate each of the 65 536 pixels in one of the following modes: particle counting (Medipix mode), energy measurement (Time over-Threshold — ToT mode) and measurement of the interaction time (Time-of-Arrival — ToA mode).

Timepix3 introduces an additional mode that is capable of simultaneous time-of-arrival (ToA) and energy (ToT) measurements, therefore allowing unambiguous identification of pixel clusters that belong to the same X-ray interaction. The schematic arrangement of the Timepix detector is in figure 1.
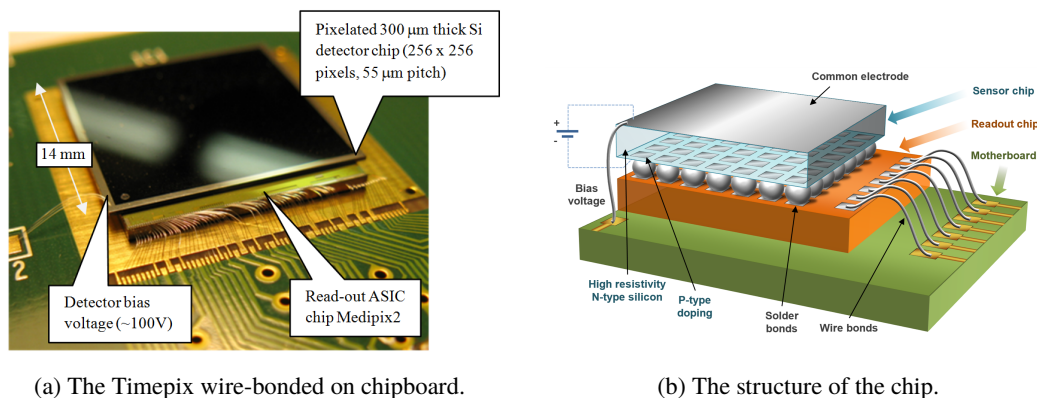

Pixelated 300 μm thick Si detector chip (256 x 256 pixels, 55 μm pitch)

14 mm

Detector bias voltage (~100V)

Read-out ASIC chip Medipix2

Common electrode

Sensor chip

Readout chip

Motherboard

Bias voltage

High resistivity N-type silicon

P-type doping

Solder bonds

Wire bonds

(a) The Timepix wire-bonded on chipboard.   (b) The structure of the chip.

Figure 1. The Timepix chip is a combination of a sensor material, which is bump-bonded to the ASIC chip.

2 Experimental setup

This experiment was performed on the Timepix3 detector with the AdvaPIX TPX3 read-out interface. The tested detector was equipped with a 300 μm thick Si sensor and the radiation-sensitive chip

was uncovered and its back-side (with a bump-bonded ASIC chip) was attached to the aluminium block (see figure 2). This block was thermally coupled to the TPX3 chip itself and thermally stabilised by a three-stage Peltier element, with the temperature feedback consisting of a Pt1000 thermometer. The entire ensemble was placed inside a vacuum chamber and an external water cooling system dissipated the waste heat. The TPX3 chip was stabilised at a stable temperature for at least 10 minutes before each measurement. The whole test was performed in the vacuum chamber under a reduced pressure of approximately 3.4×10^{-6} hPa.
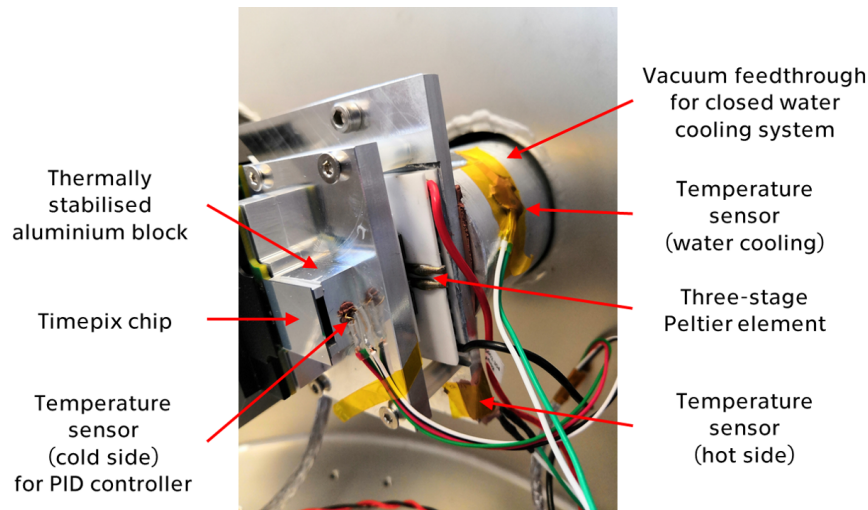

Figure 2. Detail of the detector's arrangement for thermal stabilisation in the vacuum chamber.

3 Equalisation

Threshold equalisation is a procedure which exploits the 4-bit threshold level (THL) adjustment for each pixel, and makes the overall threshold level as homogenous as possible. This procedure is used to compensate the pixel to pixel threshold variations and is necessary because each pixel, even without irradiation, generates a nonzero response (known as the dark current). This kind of current is individual for each pixel and causes noise in measurement values. The 4-bit threshold-adjustment prepares the individual response for each pixel. It finds a distribution of THLs for each adjustment value, and adjusts each pixel so that its threshold is as near as possible to the average of the threshold distribution. With respect to the detection range, the THL scan is performed in the range around the noise edge. A typical example of THL equalisation for the TPX3 detector can be seen in figure 3a.

The equalisation procedure consists of several steps and is performed without detector irradiation. In the first step, the 4-bit THL adjustment for all pixels is set to the minimum (0 ADU), and a progressive THL scan is performed where the number of new responsive pixels is noted for each THL. The distribution of this measurement can be seen in figure 3a ("Min". — red). The mean value (Min. M) in this case indicates that half of the pixels on the detector are above the THL. The next step of the measurement is performed with the maximum THL adjustment (15 ADU) for all pixels
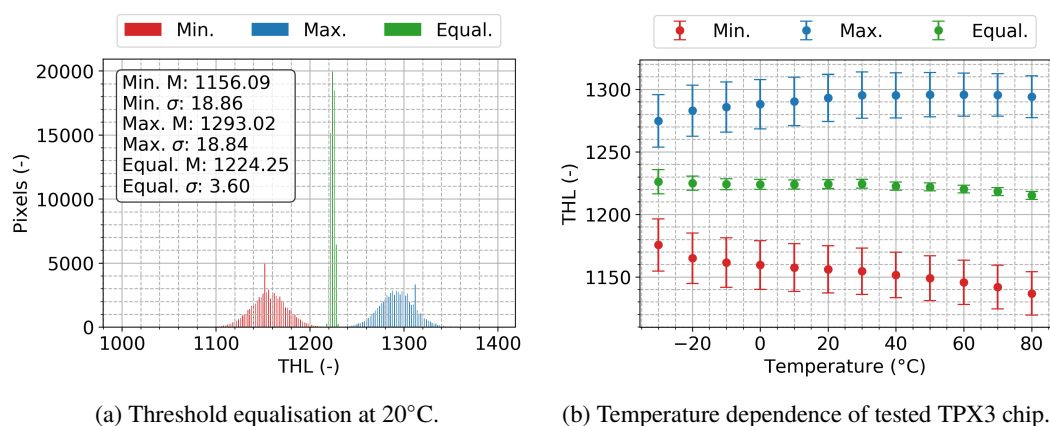
(a) Threshold equalisation at 20°C.

(b) Temperature dependence of tested TPX3 chip.

Figure 3. TPX3 chip threshold equalisation.

(figure 3a "Max". — blue). Then, using these values the whole detector is equalised, meaning that each pixel has an individually adjusted THL. This result is shown in figure 3a ("Equal". — green).

Due to the fact that the dark current of each pixel is highly temperature-dependent, this equalisation is only valid for measurements under the same temperature conditions. The influence of temperature changes on the equalisation results for TPX3 and its distribution are in figure 3b.

4 Threshold scan depending on the temperature and the radiation energy

A threshold scan with characteristic X-ray radiation was performed after the detector equalisation. The TPX3 detector was exposed to a series of X-ray radiation after stabilisation at each temperature. Discrete, narrow band X-ray radiation from X-ray fluorescence (XRF) was used, instead of wide-band bremsstrahlung radiation, for better detection of changes in detector's behaviour and its sensitivity. XRF yields radiation at the characteristic energies of the material (shown in table 1) from which the target was made.

Table 1. The characteristic lines of chosen elements.

Symbol	Element	Energy
Ti	Titanium	4,508 keV
Fe	Iron	6,398 keV
Cu	Copper	8,046 keV
Mo	Molybdenum	17,480 keV
Cd	Cadmium	23,106 keV

The THL was scanned while both varying the X-ray energy and detector temperature to establish a relationship between the two. The number of counts over a constant exposure time was recorded and the measured data is plotted in figure 4a with the Gauss and Error function (*gerf*) fit. Figure 4a shows an example of a radiation measurement at 8 keV (Cu) and at a stabilised temperature of 20°C, the temperature for which the TPX3 detector was equalised.
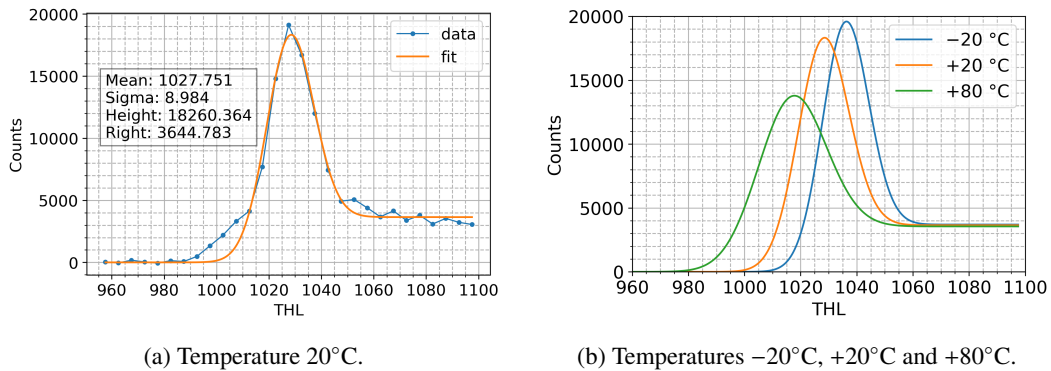
(a) Temperature 20°C.

(b) Temperatures −20°C, +20°C and +80°C.

Figure 4. Data and fits of THL scans based on characteristic XRF radiation of Cu at the different temperatures. A decrease in THL means an increase in the value of XRF energy. The offset in the right part of the plot is caused by the charge sharing effect.

The measured mean value annotated in figure 4a, corresponds to the maximum energy peak position for the characteristic target radiation. Values from measurements on several energies are then used for calibration of the detector. The sigma value is used to determine the threshold setting precision.

The data set for each energy consists of measurements under several temperatures in the range from −20°C to +80°C. Figure 4b shows chosen examples for room temperature (20°C), minimal reached temperature (−20°C) and maximal reached temperature (+80°C) measurements. The influence of temperature dependence on the THL maximum for radiation at 8 keV (Cu) is also evident.

The progression of the mean and sigma dependency for the copper target through the whole temperature range is shown in figure 5a. A comprehensive overview of the effect on the measured values for the used energies in the range of 4–24 keV (see table 1) and temperatures from −20°C to +80°C is provided in figure 5b. The graph shows the difference in measurement compared to the reference measurement at 20°C for the comparison of effects at different incident energies.

These results show an increasing dependence of the measured maximum energy on the detector temperature. Graph 5b also shows that the temperature effect has a more significant influence on the measurement with the increasing energy level of incident radiation.

An alternative perspective of the processed data are shown in figure 5c (resp. 5d), where the dependencies of the parameter changes as a function of radiation energy is plotted. Two curves for minimum and maximum temperature are used.

5 Conclusion and future work

The Timepix3 detector (300 μm Si) was tested in a wide range of temperatures (from −20°C to +80°C) under vacuum conditions to examine the detector behaviour under extreme conditions, which is essential for space applications. The temperature range was chosen according to requirements for Low-Earth-Orbit satellites. The first part of the testing was focused on the chip
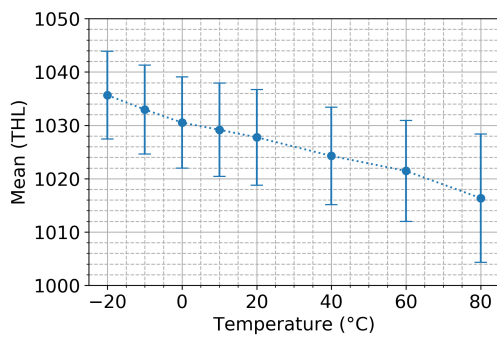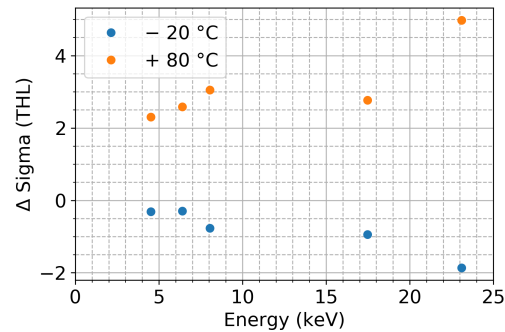
(a) Mean for Cu radiation depending on the chip temperature.
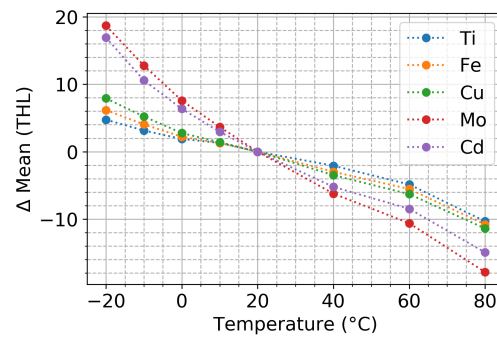
(b) Shift of the XRF Mean depending on the chip temperature.
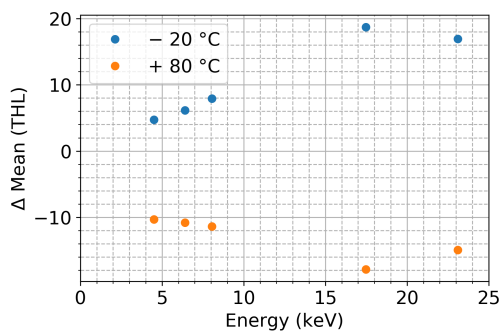
(c) Shift of Mean depending on the radiation energy.

(d) Shift of Sigma depending on the radiation energy.

Figure 5. Mean and Sigma, from the *gerf* fits of measured THL scan of exciting radiation by XRF for elements in the table 1. The reference value for the shift evaluation was measurement at standard room condition (20°C). Each point in figure 5a is based on an equivalent results as is shown in figure 4a. The standard deviation of values is ∼ 1%. Based on the accuracy of the measurements shown in figure 5a, the uncertainty of determining the difference for the figures 5b–5d is better than 10% is considered using the T-test.

equalisation without radiation, and a shift of noise level was observed with temperature change. Also, the validity of the chip normal-conditions-setting was deeply studied. In the next step, the measurement of characteristic X-ray radiation of selected elements (Ti, Fe, Cu, Mo, Cd) was performed. The shift of the fluorescence peaks and the peak width were measured.

The results show the dependence of the used Timepix3 detector on the chip temperature as well as the incident energy. The character of dependency changes its parameters with respect to both these variables (temperature and energy). The consequence is a distortion of the measured quantities, which may affect the overall evaluation of the incident radiation. For this reason, it is recommended to use this type of detector under stable temperature or with the temperature stabilisation system.

There are applications where meeting this requirement for measurement conditions is very challenging and/or expensive, such as space measurements. Thus, the goal of future work is to study the Time-over-Threshold (per pixel energy) calibration and its validity under specific conditions in order to get the overall knowledge necessary for the usage of Timepix3 detectors in

future space missions, as well as more detailed measurements at points of interest (change of the slope dependency between the 17 keV and 23 keV incident energy) and on the broader energy range.

Based on the knowledge of detector behaviour, a procedure (an algorithm) can be designed to minimise this effect of distortion while maintaining the reduced requirements for temperature stabilisation and cooling.

Acknowledgments

References

[1] X. Llopart, R. Ballabriga, M. Campbell, L. Tlustos and W. Wong, *Timepix, a 65 k programmable pixel readout chip for arrival time, energy and/or photon counting measurements*, *Nucl. Instrum. Meth.* **A 581** (2007) 485 [*Erratum ibid.* **A 585** (2008) 106].

[2] T. Holy, E. Heijne, J. Jakubek, S. Pospisil, J. Uher and Z. Vykydal, *Pattern recognition of tracks induced by individual quanta of ionizing radiation in Medipix2 silicon detector*, *Nucl. Instrum. Meth.* **A 591** (2008) 287.

[3] C. Granja et al., *Energy loss and online directional track visualization of fast electrons with the pixel detector Timepix*, *Radiat. Meas.* **59** (2013) 245.

[4] C. Granja et al., *The SATRAM Timepix spacecraft payload in open space on board the Proba-V satellite for wide range radiation monitoring in LEO orbit*, *Planet. Space Sci.* **125** (2016) 114.

[5] T. Baca et al., *Miniaturized X-ray telescope for VZLUSAT-1 nanosatellite with Timepix detector*, 2016 *JINST* **11** C10007.

[6] M. Urban, O. Nentvich, V. Stehlikova, T. Baca, V. Daniel and R. Hudec, *VZLUSAT-1: Nanosatellite with miniature lobster eye X-ray telescope and qualification of the radiation shielding composite for space application*, *Acta Astronaut.* **140** (2017) 96.

[7] V. Daniel et al., *In-Orbit Commissioning of Czech Nanosatellite VZLUSAT-1 for the QB50 Mission with a Demonstrator of a Miniaturised Lobster-Eye X-Ray Telescope and Radiation Shielding Composite Materials*, *Space Sci. Rev.* **215** (2019) 40.

[8] T. Baca et al., *Timepix in LEO Orbit onboard the VZLUSAT-1 Nanosatellite: 1-year of Space Radiation Dosimetry Measurements*, 2018 *JINST* **13** C11010.

[9] W. Furnell, A. Shenoy, E. Fox and P. Hatfield, *First results from the LUCID-Timepix spacecraft payload onboard the TechDemoSat-1 satellite in Low Earth Orbit*, *Adv. Space Res.* **63** (2019) 1523 [arXiv:1810.12876].

[10] P. Hatfield et al., *IRIS opens pupils' eyes to real space research*, *Astron. Geophys.* **60** (2019) 1.22.

[11] R. Filgas, *Space radiation monitoring with Timepix*, *Astron. Nachr.* **339** (2018) 386.

[12] T. Poikela et al., *Timepix3: a 65 K channel hybrid pixel readout chip with simultaneous ToA/ToT and sparse readout*, 2014 *JINST* **9** C05013.

3.2 Event counting mode

The Event counting mode is one of the core modes of the Timepix3 detector. This measurement principle has already been used in the predecessor of the Timepix detectors, the Medipix detectors. This mode is widely used in medical imaging, X–ray microscopy and imaging of material samples using transmission X–ray imaging.

The principle of EC measurement is to count the number of times the signal received from the CSA exceeds the set THL. Each time such an event occurs, a one is added to the counter register of the hit pixel. This can occur multiple times within a single continuous exposure and even within Frame readout mode. In the case of multiple hits, there is no pile-up and, therefore, no distortion of the acquired data, as in the case of Time-over-Threshold energy measurement. Thus, this measurement provides information about the value of the incident flux on individual pixels within the resulting frame.

However, if used correctly, the EC mode can also be used to measure the energy of the incident radiation. This is known as the Threshold scan method. This method requires a constant flux of incident radiation throughout the acquisition time and consists of a sequence of individual measurement frames. For these scans, the value of the global THL setting is gradually increased. The energy spectrum of the radiation is then obtained by sequentially evaluating the difference between the individual frames. This method is also used in the detector calibration procedure to obtain an energy value equivalent to the threshold setting.

The effects already identified when testing the temperature stability of the equalisation [9, 10] suggested that the values obtained using the Timepix3 detector in EC mode would be affected depending on the environmental conditions. The influence of detector temperature variation on EC data, evaluated by XRF energy spectra, has been analysed in the following publication.

As indicated above, the TPX3 hybrid pixel detector is sensitive to temperature distortion. This was tested in a thermo-vacuum chamber at a pressure of 3.4×10^{-4} Pa within a temperature range of $-20\,°C$ to $80\,°C$. A spectral drift towards higher energies with increasing detector temperature is clearly visible at the energies defined by the used X–ray fluorescence targets. The intensity of this drift depends on the energy of the incident radiation. In the energy range under investigation, it causes a $2\,\%$ relative error in accuracy for a temperature change of $\pm20\,°C$ and a relative error of up to $10\,\%$ in the measured energy of the XRF radiation with the detector stabilised at $80\,°C$.

The EC mode requires a long measurement time to acquire the sequence of frames needed to evaluate the radiated energy spectrum. Therefore, it is unsuitable for spectral analysis of unstable, faint or short-lived energy sources such as GRBs and other sources in space. However, it can be used in X–ray imaging applications where information about the energy of the incident radiation is not required. However, it should be noted that in this case, there will also be a thermal drift of the detector, which will affect its THL setting. In this case, this will affect the measured flux of the source.

Timepix3: Temperature influence on X-ray measurements in counting mode with Si sensor

Martin Urban [a,*], Daniela Doubravová [b]

[a] *Faculty of Electrical Engineering, Czech Technical University in Prague, Prague, Technická 2, 166 27 Prague 6, Czech Republic*
[b] *Advacam, s.r.o., U Pergamenky 1145/12, 170 00 Prague 7, Czech Republic*

ARTICLE INFO

ABSTRACT

The Timepix3 radiation imaging and particle tracking detector is the direct successor to the Timepix semiconductor detector developed in CERN. The Timepix ASIC chip (256×256 pixels with a pitch of $55\,\mu m$) provides the possibility to operate each of the 65 536 pixels in one of the following modes: (1) event counting (Medipix mode); (2) energy measurement (Time over Threshold — ToT mode); and (3) measurement of the interaction time (Time of Arrival — ToA mode). The Timepix3 chip of the new generation introduces the ability to measure ToT and ToA simultaneously and also the event-based readout where each hit pixel is read out immediately after the hit. This detector can be used in a variety fields of science including particle physics, X-ray imaging as well as medicine and space science. With regards to the wide application possibilities of this detector, we investigate the properties of the detector in the temperature range from $-20\,°C$ to $+80\,°C$. This temperature range spans the majority of laboratory conditions as well as requirements for most of outer space missions. This paper describes thermal-vacuum testing of the most common $300\,\mu m$ Si detector with AdvaPIX readout interface in the counting mode. The detector was stabilised under various thermal conditions in a thermal vacuum chamber and subsequently exposed to characteristic X-ray radiation of 5 elements in the energy range of $4–24\,keV$. It was found that the absolute measurement accuracy of higher energies is more affected by higher temperature (up to $0.8\,keV\,@\,17.48\,keV$) and relative error of Timepix3 accuracy is inversely proportional to the incident X-ray energy. The relative precision is kept in the range of $6\,\%$ for temperatures from $-20\,°C$ to $+60\,°C$ with significant change at $+80\,°C$.

1. Introduction

Temperature stability and known temperature dependence are one of the most critical parameters of modern semiconductor sensors, among which Timepix3 (TPX3) is no exception. The properties of these sensors and detectors, together with the accuracy of the measurement, are usually closely linked to the conditions under which the measurement was performed. For this reason, various methods of sensor/detector calibration are introduced, which are mostly valid under the same (or very similar) measurement conditions. These detectors usually require constant operating conditions utilising, e.g. temperature stabilisation.

Due to the fact that X-ray radiation measurement is widespread in a wide range of fields, it is often challenging to provide these conditions. Detectors from the Timepix/Medipix family are often used for imaging (Dudak, 2020), dosimetry or as radiation environment monitor. Their applications range from medicine (Procz et al., 2019), such as mammography (Ávila et al., 2017) or dental imaging (Watt

et al., 2003), to homeland security applications, such as the localisation of radiation sources (Baca et al., 2020), to scientific instruments like ATLAS (Bergmann et al., 2019) and many more. The predecessors of TPX3 were even used on several satellites: the SATRAM experiment (Granja et al., 2016; Gohl et al., 2019, 2016) onboard of ESA's satellite PROBA-V (Dierckx et al., 2014; Francois et al., 2014); British satellite TechDemoSat-1 (Foti et al., 2015; Unwin et al., 2016) with LUCID experiment (Whyntie and Harrison, 2014, 2015; Hatfield et al., 2018; Furnell et al., 2019), RISESAT microsatellite (Filgas et al., 2019; Filgas, 2018) and last but not least the Czech CubeSat VZLUSAT-1 (Baca et al., 2016; Urban et al., 2017; Daniel et al., 2019; Baca et al., 2018) and Rocket experiment (Urban et al., 2020b; Stehlikova et al., 2017; Dániel et al., 2017; Daniel et al., 2019) onboard the suborbital rocket campaign (Miles et al., 2017) in combination with X-ray optics.

In all these branches, detectors undergo thermal changes, which should be compensated and the detector should be stabilised at a constant temperature that corresponds to its calibration and operating conditions. Achieving these conditions can be problematic, depending on
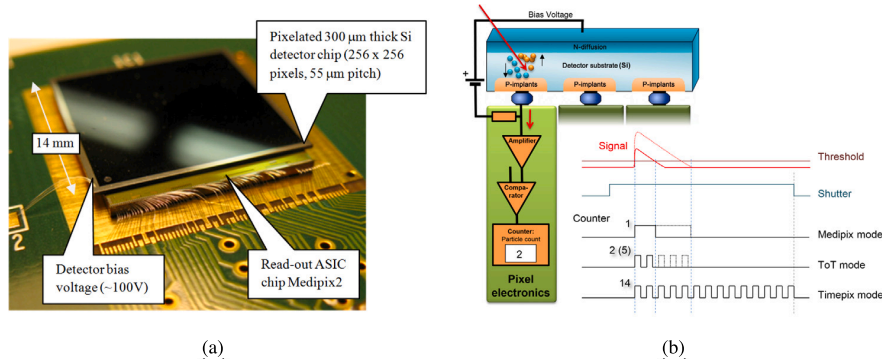
Fig. 1. (a) The Timepix sensor consists of an 300 μm Si detector; the ASIC read-out chip provides the radiation images in 256 × 256 px resolution (Granja et al., 2016), (b) Simplified diagram of Timepix function in different modes of operation.

the application. Thermal stabilisation could be even too demanding and expensive in case of space application. Nevertheless, the requirement for accurate and stable measurements remains relevant and important in many respects. The description of the temperature dependence and its minimisation is therefore highly desirable. Due to the wide range of applications mentioned above, the temperature range for testing and analysing the detector was chosen as wide as possible to cover the majority of applications.

The used TPX3 detector with 300 μm silicon was tested in the temperature range from −20 °C to +80 °C which also meets the requirements for low Earth orbit missions according to QB50 mission (Gill et al., 2013) (in which VZLUSAT-1 is included), i.e. from −20 °C to +50 °C.

Timepix devices are hybrid pixel particle counting detectors, which consist of a square matrix of 256 × 256 pixels with a pixel pitch of 55 μm (Llopart et al., 2007). The detector consists of a semiconductor sensitive layer bump-bonded to an Application Specific Integrated Circuit (ASIC) readout chip. The ASIC chip provides integrated signal electronics for each individual pixel, including a charge-sensitive amplifier, threshold discriminator, 14-bit counter and Wilkinson type analogue-to-digital converter (ADC).

This arrangement allows each of the 65 536 pixels to be operated independently in one of the following modes: Medipix mode — the number of impacts during the exposure time above the discrimination level; ToT mode — the measurement of the deposited energy of the incident particle using the Wilkinson type ADC, where the duration (number of clock ticks) above the discrimination level (threshold) is recorded during the linear discharge of the signal; ToA/Timepix mode — the measurement of the particle impact time, i.e. the time of exceeding the discrimination level (threshold). The descriptive picture of the sensor with the ASIC and simplified diagram of operation modes are shown in Fig. 1.

Timepix3 chips (Poikela et al., 2014) are operated in event-based (also known as data-driven) mode, where the complete information about particle interaction is obtained immediately after the hit. In this mode, a continuous stream of data (pixel coordinates, ToA and ToT) is generated.

Due to their hybrid structure, detectors of the Medipix family can be made of different semiconductor or semi-insulating materials (Si, GaAs, CdTe, CZT, etc.) used for the sensitive layer with the same ASIC readout chip. The sensor is a monolithic sensitive layer with a common bias electrode on top and a doped bump-bonded pixel matrix on the bottom side. Depending on the application and energy range of the radiation, the thickness of the material can vary, typically in the range from 100 μm to 2000 μm. The maximum deposited energy of particles increases together with the photon detection efficiency with thickness of the selected material.

This manuscript presents the results of thermal vacuum tests of the Timepix3 detector equipped with a 300 μm thick silicon sensor and

the AdvaPIX interface. This detector had been tested in a temperature range from −20 °C to +80 °C, which meets the required conditions for LEO (QB50; Gill et al., 2013). Testing was performed using X-ray fluorescence, where the detector was irradiated with characteristic radiation of 5 elements in the energy range of 4–24 keV.

2. Description of measurement and threshold calibration

The experiment was performed with a Timepix3 detector (AdvaPIX TPX3 device) placed in a vacuum chamber under pressure of approximately $3.4 \cdot 10^{-6}$ hPa. A detector equipped with a 300 μm thick Si sensor was attached to an aluminium block, which was thermally coupled and stabilised using a three-stage Peltier element (Fig. 2) at a series of temperatures in the range −20 °C to +80 °C. After reaching the target temperature, the detector was stabilised for at least 10 minutes before each measurement. The set temperature is feedback-controlled using a platinum thermometer located just under the Timepix chip. Waste heat from the warm side of the Peltier element was dissipated through the water cooling system outside of the vacuum chamber.
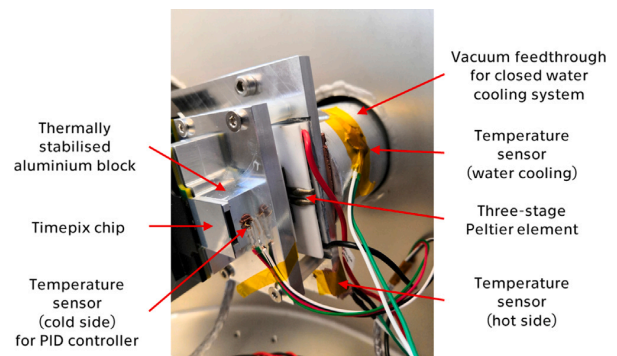
Fig. 2. Detector arrangement for thermal stabilisation in the vacuum chamber (Urban et al., 2020a).

The detector was exposed to a series of characteristic X-ray radiation generated by X-ray fluorescence (XRF). The main advantage of XRF is the generation of characteristic X-ray radiation on precisely determined energy lines. The energies are determined by a material of the anode target. The target materials and their respective XRF yields radiation energies are listed in Table 1.

By using the defined energy value of incident radiation, it is possible to define the change in the response of the detector to different, predetermined, radiation energies and therefore calibrate the detector. However, before starting the measurement and subsequent calibration of the detector, it is first necessary to perform threshold equalisation

Table 1

List of targets with characteristic lines.

Symbol	Element	Energy
Ti	Titanium	4,508 keV
Fe	Iron	6,398 keV
Cu	Copper	8,046 keV
Mo	Molybdenum	17,480 keV
Cd	Cadmium	23,106 keV

of the detector (van der Boog, 2013; Uher and Jakubek, 2011; Urban et al., 2020a). Each pixel in the chip responds in a different way to an incoming radiation and, even without irradiation, generates some signal (known as the dark current) due to fabrication mismatches and non-uniformities of the detector. This current causes a slightly different noise in each pixel. The threshold equalisation procedure configures the 4-bit threshold fine adjustment of each pixel and compensates these variations and non-uniformities. The result of the equalisation procedure is to provide the pixel matrix as homogeneous as possible and obtain a more uniform response with the narrowest possible distribution of pixel threshold levels across the chip. The detector can be calibrated only after such equalisation of all pixels. A global calibration method, instead of per pixel, has been used in this article.

A Threshold scan method is applied for the global calibration of the energy threshold (THL) of the detector after its equalisation. The THL scan consists of a collection of many measurements with a sequential change of the THL value for each measurement. In this way, a cumulative radiation spectrum is created for each target (monochrome).

Every absorbed photon with energy exceeding the Threshold is counted in the bin of the THL. The spectrum is then obtained by discrete differentiation of the cumulative distortion with the respect to the THL. The Fig. 3 shows the resulting spectrum. As can also be seen from Fig. 3, the higher value of electronic THL settings is for lower energy values, depending on the used type of readout circuit.
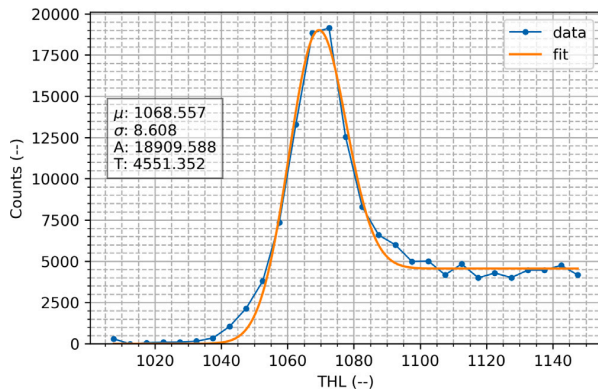

Fig. 3. The XRF global spectrum of radiation with Iron target measured with the TPX3 detector at 20 °C. The values of μ - Mean, σ - Standard Deviation, A - Magnitude and right Tail T are marked in the figure. The function according to Eq. (1), which parameters are explained in the text, was used as a fit function.

The incident particles (mainly photons, in this case) generate an electron–hole cloud in the sensor material. Because of the thermal diffusion effect, these charge carriers move in a random direction, not only in the direction perpendicular to the electrodes (according to the electric field) but also transversely. Therefore, the generated charge carries spread into neighbouring pixels from the place of origin. The charge, shared across multiple pixels, creates a seemingly valid signal of multiple lower-energy photons. This phenomenon is called the charge sharing effect and it causes the asymmetry tail (T) of the measured spectrum, which is significant in the right part of Fig. 3. It can also cause the final peak position is shifted from the real value of the XRF

energy level because not all the generated charge is gathered by a single pixel.

The measured spectrum is then approximated by a combination of a Gaussian function and the Error function

$$gerfc(x) = A_1 \cdot e^{\frac{-(x-\mu)^2}{2\sigma^2}} + A_2 \cdot f_{erfc}\left(\frac{x-\mu}{\sigma\sqrt{2}}\right), \tag{1}$$

where x is the THL, and f_{erfc} is the complementary Error function

$$f_{erfc}(x) = 1 - \frac{2}{\sqrt{\pi}}\int_0^x e^{-t^2}dt. \tag{2}$$

The approximation is used to determine the position of the maximum of the sensed radiation (XRF energy), its standard deviation and magnitude is determined, including a description of the value of the charge sharing effect. They are referred to as μ - Mean, σ - Standard Deviation, A - Magnitude ($A_1 + A_2$) and right Tail as $T = 2A_2$ in Fig. 3.

By successively measuring the values for all calibration materials (Table 1), a description of the dependence of the set THL on the energy of the incident radiation is obtained (Fig. 4). This dependence is affine and can, therefore, be described by two parameters a, b:

$$THL = a \cdot E + b \tag{3}$$

where THL is the value of the set threshold, E is the radiation energy, a is the slope of the regression line, and b is its offset.
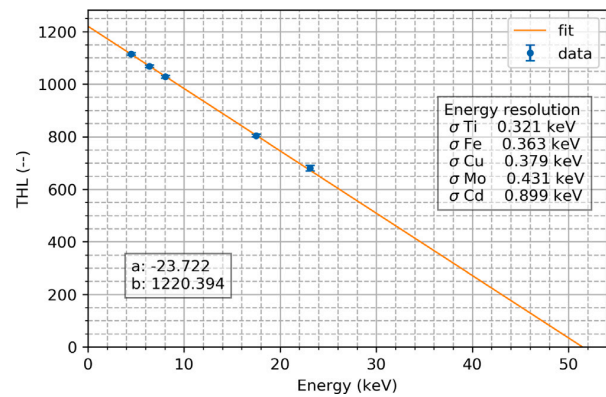

Fig. 4. Threshold calibration and energy resolution for calibrated XRF energies at 20 °C.

The resolution of the detector threshold level for individual XRF energies can be determined from the known parameters of the calibration curve (a and b) and the σ of the measured signal.

3. Temperature effect

The effect of different temperatures of the detector affects its detection properties, and due to the shift of the calibration curves, the recorded signal is distorted. We found that the amount of distortion depends not only on the temperature of the detector but also on the energy of the incident radiation. A combined graph of the measured spectra for the temperature extremes −20 °C and +80 °C together with the reference value +20 °C is shown in Fig. 5. For clarity, the measured data are shown using Gaussian fits with the charge sharing effect being subtracted.

The normalised signals show that due to temperature change causes a significant shift of the measured spectra and change in their width. The series of THL scan measurements were performed in several temperature steps and evaluated based on calibration values obtained at +20 °C as already mentioned (see Table 2). The detector temperature of +20 °C is used as the reference for further evaluation.

Table 2

Comparison of the influence of detector temperature on sensed radiation energies using TPX3.

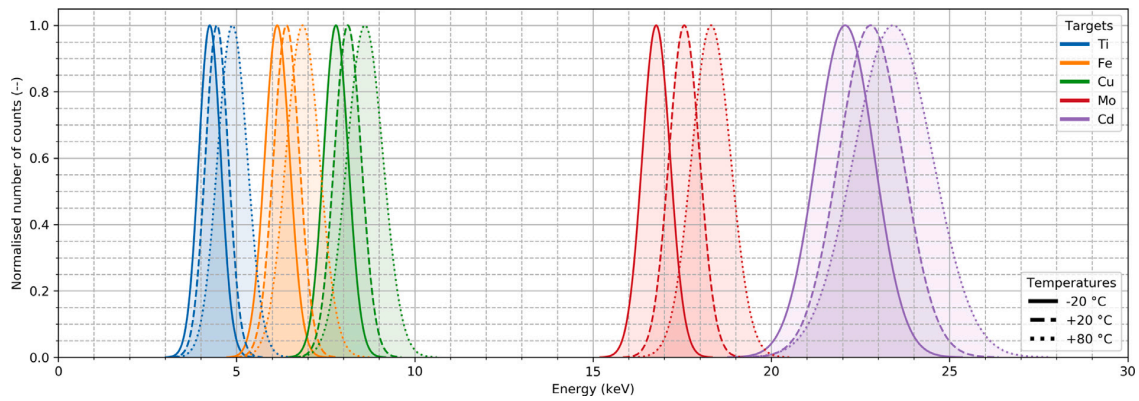| Material	Energy	Evaluated energy (keV)				
	(keV)	−20 °C	0 °C	+20 °C	+60 °C	+80 °C
Ti	4.508	4.249 ± 0.308	4.369 ± 0.305	4.449 ± 0.321	4.654 ± 0.347	4.884 ± 0.419
Fe	6.398	6.141 ± 0.351	6.307 ± 0.356	6.401 ± 0.363	6.634 ± 0.389	6.856 ± 0.472
Cu	8.046	7.788 ± 0.346	8.005 ± 0.360	8.121 ± 0.379	8.386 ± 0.400	8.601 ± 0.507
Mo	17.480	16.771 ± 0.392	17.239 ± 0.404	17.559 ± 0.431	18.006 ± 0.471	18.311 ± 0.548
Cd	23.106	22.071 ± 0.821	22.517 ± 0.848	22.785 ± 0.899	23.142 ± 0.981	23.415 ± 1.109

Fig. 5. Comparison of the spectra measured using THL scans for different detector temperatures and incident radiation energy. A calibration at +20 °C was applied; the resulting data were approximated with Gaussians and normalised. The charge sharing effect was subtracted.
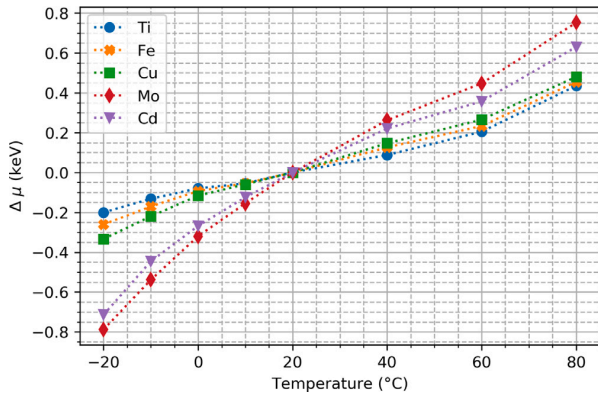

Fig. 6. Dependence of absolute measurement accuracy on the detector temperature for different energies of incident radiation.
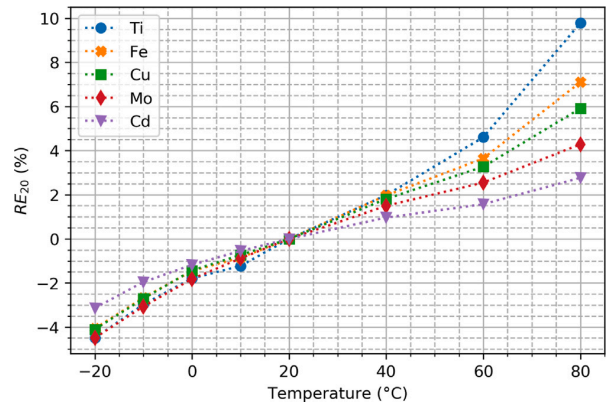

Fig. 7. Evolution of relative measurement accuracy depending on the detector temperature for different energies of incident radiation.

Several indicators such as the absolute shift of the spectrum

$$\Delta\mu = \mu_x - \mu_{20}, \quad (4)$$

Relative error (RE) of measurement

$$RE_{20} = \frac{\mu_x - \mu_{20}}{\mu_{20}} \cdot 100, \quad (5)$$

Coefficient of Variation (CV_X) ratio measured of each temperature for the reference value (+20 °C - CV_{20})

$$CV_x/CV_{20} = \frac{\sigma_x}{\mu_x} \cdot \frac{\mu_{20}}{\sigma_{20}}, \quad (6)$$

and Relative Standard Deviation (RSD)

$$RSD = \frac{\sigma_x}{\mu_x} \quad (7)$$

are compared. The subscript of variables is used as a label for the temperature of measurement, i.e. μ_x is the peak position measured at temperature x, σ_{20} is the standard deviation for a detector stabilised at 20 °C and etc.

The data suggest that the absolute measurement accuracy (Eq. (4)) of the TPX3 detector with 55 μm Si sensor is more pronounced with increasing value of the incident radiation energy (Fig. 6).
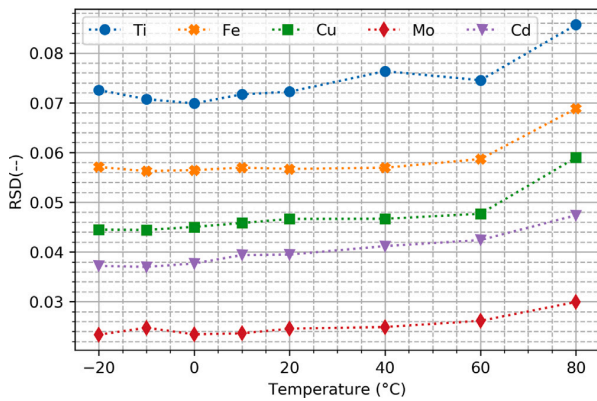
4

Fig. 8. Temperature dependence of the relative standard deviation for different XRF target and detector temperatures.

Fig. 10. Evolution of relative measurement precision using the Coefficient of Variation ratio for the tested and reference temperature.
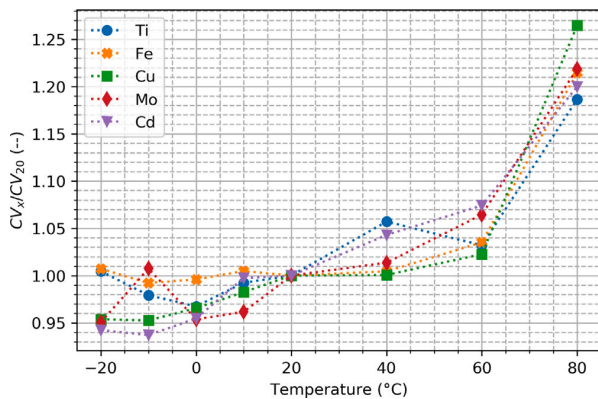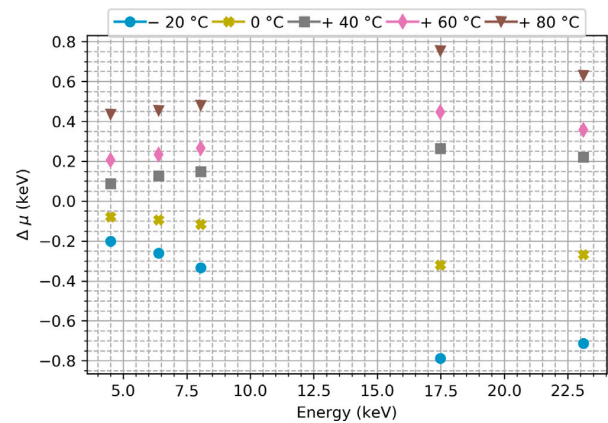

Fig. 9. Evolution of relative measurement precision using the Coefficient of Variation ratio for the tested and reference temperature.

However, the relative measurement accuracy (Eq. (5)) is negatively correlated to the incident energy (Fig. 7). This temperature dependence of the detector causes a relative accuracy of approx. 2% when the temperature changes by 20 °C and up to 10% when the detector temperature changes by 60 °C (it is at a temperature of 80 °C).

According to the graph of RSD (Fig. 8) and Eq. (7), the dispersion evolution of the sensed energy distribution is observed. It can be seen that the value of the measurement precision, for the individual energies of the incident radiation, is approximately constant with a slight increase in dispersion with increasing temperature. This increase can be attributed to thermal noise in the detector.

Looking on a finer scale with the dependence of the CV_x/CV_{20} ratio (Eq. (6)) on the temperature (Fig. 9), it can be read that the change in relative precision is kept in the range of approx. 6% in the tested temperature range from −20 °C to 60 °C, however, for a temperature of 80 °C there is a significant increase of more than 18% compared to precision at +20 °C.

The graph 10 shows the dependence of the absolute measurement accuracy, i.e. the displacement of the measured μ, on the energy of the XRF radiation for individual materials under the different detector temperatures.

Significant variations in behaviour for the detection of Molybdenum XRF radiation were observed. This phenomenon will be subject to further research.

Last but not least, as the temperature increases, the σ and μ of the detected signal increase and its A decreases. This phenomenon is

shown in Fig. 11a) for the temperature extremes (−20 °C and +80 °C) and a reference temperature of +20 °C. This finding could also mean a change in the Photon Detection Efficiency (PDE) of the detector, which is defined as probability of photon interaction in the sensor. For this reason, the change in Relative Photon Detection Efficiency (RPDE) for each temperature and energy was evaluated as the ratio of the integrated number of measured counts to the reference measurement (see Fig. 11b). The exposure time of all measurements was constant, as was the energy range for each target material and X-ray tube settings.

Although there is a significant decrease in A, this change is sufficiently compensated by the increase in σ (Fig. 11a) and the integrated number of measured counts is therefore almost unchanged. The results show that there is no significant change in RPDE for any of the tested energies, and there is no apparent temperature dependence (Fig. 11b). Recorded fluctuations of ±5% may be caused by measurement inaccuracies and slight fluctuations in the intensity of the X-ray lamp with the same setting.

4. Conclusion

This paper provides results from temperature testing of the 55 μm silicon sensor in close connection with complex signal processing electronics like Timepix3 ASIC. The AdvaPIX interface was used as readout. Testing was performed under reduced pressure of approximately $3.4 \cdot 10^{-6}$ hPa in the temperature range from −20 °C to +80 °C. This temperature range spans the majority of TPX3 applications as well as requirements for most of low Earth orbit space missions. The research aimed to determine the temperature effect on the ability to record the number of individual X-ray events (counts) - counting mode - on the detector. The course of measurement and the threshold calibration in the range of 4–24 keV was described in detail. The presented results show changes caused by the temperature change of the combination of the complex ASIC and the 55 μm silicon sensor. Based on the obtained data, it was shown that the relative measurement accuracy is negatively correlated to the incident energy and causes a 2% relative accuracy error when the temperature changes by 20 °C or up to 10% when the detector temperature reached 80 °C. Nevertheless, the variance of the individual measurements with respect to the value of the incident energy thus the precision of the measurements is almost constant over the entire range of tested temperatures with a slight increase in dispersion at 80 °C. The relative precision change of the Timepix3 measurement is kept up to 6% up to 60 °C with a significant increase to 20% at 80 °C. There was no significant change in the Photon Detection Efficiency of the detector for individual XRF energies or for different measurement temperatures. The subject for the future research is proposing a correction method to minimise the temperature effect on the TPX3 detector performance.
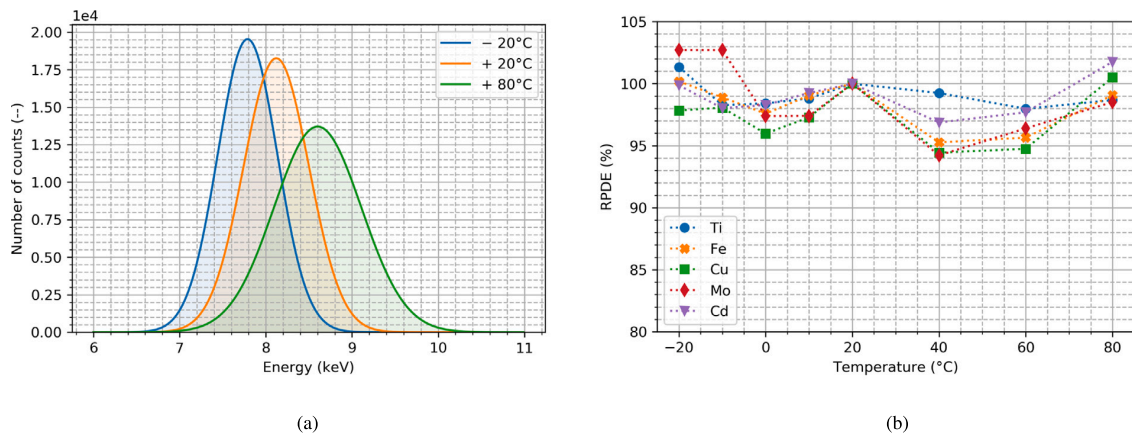
(a)   (b)

Fig. 11. Photon Detection Efficiency and its temperature dependence; (a) change of the measured radiation spectrum at constant X-ray source settings with Cu target and different detector temperatures, (b) Relative Photon Detection Efficiency for individual energies (target materials) over all tested temperatures. Measurement at 20 °C was used as a reference value.

Declaration of competing interest

One of the co-authors, Daniela Doubravová, works in a company focusing on radiation detectors. However, this fact did not affect the processing and interpretation of the measured data and published results. There was no influence of results or distortion of the presented data.

References

Ávila, C.A., Mendoza, L.M., Roque, G.A., Loaiza, L., Racedo, J., Rueda, R., 2017. Feasibility study of a TIMEPIX detector for mammography applications. In: Romero, E., Lepore, N., Brieva, J., García, J.D. (Eds.), 13th International Conference on Medical Information Processing and Analysis, Vol. 10572. SPIE, pp. 302–312. http://dx.doi.org/10.1117/12.2285910.

Baca, T., Jilek, M., Vertat, I., Urban, M., Nentvich, O., Filgas, R., Granja, C., Inneman, A., Daniel, V., 2018. Timepix in LEO orbit onboard the VZLUSAT-1 nanosatellite: 1-year of space radiation dosimetry measurements. J. Instrum. 13 (11), C11010. http://dx.doi.org/10.1088/1748-0221/13/11/C11010.

Baca, T., Platkevic, M., Jakubek, J., Inneman, A., Stehlikova, V., Urban, M., Nentvich, O., Blazek, M., McEntaffer, R., Daniel, V., 2016. Miniaturized X-ray telescope for VZLUSAT-1 nanosatellite with Timepix detector. J. Instrum. 11 (10), C10007. http://dx.doi.org/10.1088/1748-0221/11/10/C10007.

Baca, T., Stibinger, P., Doubravova, D., Turecek, D., Solc, J., Rusnak, J., Saska, M., Jakubek, J., 2020. Gamma radiation source localization for micro aerial vehicles with a miniature single-detector compton event camera. arXiv:2011.03356.

Bergmann, B., Billoud, T., Leroy, C., Pospisil, S., 2019. Characterization of the radiation field in the ATLAS experiment with timepix detectors. IEEE Trans. Nucl. Sci. 66 (7), 1861–1869. http://dx.doi.org/10.1109/TNS.2019.2918365.

Dániel, V., Inneman, A., Pína, L., Zadražil, V., Báča, T., Stehlíková, V., Nentvich, O., Urban, M., Maršíková, V., McEntaffer, R., Tutt, J., Schulz, T., 2017. In: Hudec, R., Pina, L. (Eds.), X-ray Lobster Eye All-sky Monitor for Rocket Experiment. 1023503. http://dx.doi.org/10.1117/12.2277515.

Daniel, V., Inneman, A., Vertat, I., Baca, T., Nentvich, O., Urban, M., Stehlikova, V., Sieger, L., Skala, P., Filgas, R., Zadrazil, V., Linhart, R., Masopust, J., Jamroz, T., Pina, L., Marsikova, V., Mikulickova, L., Belas, E., Pospisil, S., Vykydal, Z., Mora, Y., Pavlica, R., 2019. In-orbit commissioning of czech nanosatellite VZLUSAT-1 for the QB50 mission with a demonstrator of a miniaturised lobster-eye X-Ray telescope and radiation shielding composite materials. Space Sci. Rev. 215 (5), 40. http://dx.doi.org/10.1007/s11214-019-0589-7.

Dierckx, W., Sterckx, S., Benhadj, I., Livens, S., Duhoux, G., Van Achteren, T., Francois, M., Mellab, K., Saint, G., 2014. PROBA-V mission for global vegetation monitoring: standard products and image quality. Int. J. Remote Sens. 35 (7), 2589–2614. http://dx.doi.org/10.1080/01431161.2014.883097.

Dudak, J., 2020. High-resolution X-ray imaging applications of hybrid-pixel photon counting detectors timepix. Radiat. Meas. 137, 106409. http://dx.doi.org/10.1016/j.radmeas.2020.106409.

Filgas, R., 2018. Space radiation monitoring with Timepix. Astron. Nachr. 339 (5), 386–390. http://dx.doi.org/10.1002/asna.201813511.

Filgas, R., Malich, M., Kuwahara, T., Broulím, J., Holík, M., Sakal, M., Murata, Y., Tomio, H., Gohl, S., Pineda T., J.M., 2019. RISEPix—A Timepix-based radiation monitor telescope onboard the RISESAT satellite. Astron. Nachr. 340 (7), 674–680. http://dx.doi.org/10.1002/asna.201913674.

Foti, G., Gommenginger, C., Jales, P., Unwin, M., Shaw, A., Robertson, C., Roselló, J., 2015. Spaceborne GNSS reflectometry for ocean winds: First results from the UK techdemosat-1 mission. Geophys. Res. Lett. 42 (13), 5435–5441. http://dx.doi.org/10.1002/2015GL064204.

Francois, M., Santandrea, S., Mellab, K., Vrancken, D., Versluys, J., 2014. The PROBA-V mission: the space segment. Int. J. Remote Sens. 35 (7), 2548–2564. http://dx.doi.org/10.1080/01431161.2014.883098.

Furnell, W., Shenoy, A., Fox, E., Hatfield, P., 2019. First results from the LUCID-Timepix spacecraft payload onboard the TechDemoSat-1 satellite in Low Earth Orbit. Adv. Space Res. 63 (5), 1523–1540. http://dx.doi.org/10.1016/j.asr.2018.10.045.

Gill, E., Sundaramoorthy, P., Bouwmeester, J., Zandbergen, B., Reinhard, R., 2013. Formation flying within a constellation of nano-satellites: The QB50 mission. Acta Astronaut. 82 (1), 110–117. http://dx.doi.org/10.1016/j.actaastro.2012.04.029.

Gohl, S., Bergmann, B., Evans, H., Nieminen, P., Owens, A., Posipsil, S., 2019. Study of the radiation fields in LEO with the space application of Timepix radiation monitor (SATRAM). Adv. Space Res. 63 (5), 1646–1660. http://dx.doi.org/10.1016/j.asr.2018.11.016.

Gohl, S., Bergmann, B., Granja, C., Owens, A., Pichotka, M., Polansky, S., Pospisil, S., 2016. Measurement of particle directions in low earth orbit with a Timepix. J. Instrum. 11 (11), C11023. http://dx.doi.org/10.1088/1748-0221/11/11/C11023.

Granja, C., Polansky, S., Vykydal, Z., Pospisil, S., Owens, A., Kozacek, Z., Mellab, K., Simcak, M., 2016. The SATRAM Timepix spacecraft payload in open space on board the Proba-V satellite for wide range radiation monitoring in LEO orbit. Planet. Space Sci. 125, 114–129. http://dx.doi.org/10.1016/j.pss.2016.03.009.

Hatfield, P., Furnell, W., Shenoy, A., Fox, E., Parker, R., Thomas, L., 2018. The LUCID-Timepix spacecraft payload and the CERN@school educational programme. J. Instrum. 13 (10), C10004. http://dx.doi.org/10.1088/1748-0221/13/10/C10004.

Llopart, X., Ballabriga, R., Campbell, M., Tlustos, L., Wong, W., 2007. Timepix, a 65k programmable pixel readout chip for arrival time, energy and/or photon counting measurements. Nucl. Instrum. Methods Phys. Res. A 581 (1–2), 485–494. http://dx.doi.org/10.1016/j.nima.2007.08.079.

Miles, D.M., McEntaffer, R.L., Schultz, T.B., Donovan, B.D., Tutt, J.H., Yastishock, D., Steiner, T., Hillman, C.R., McCoy, J.A., Wages, M., Hull, S., Falcone, A., Burrows, D.N., Anderson, T., McQuaide, M., Chattopadhyay, T., 2017. An introduction

to the water recovery x-ray rocket. In: Siegmund, O.H. (Ed.), UV, X-Ray, and Gamma-Ray Space Instrumentation for Astronomy XX. SPIE, p. 28. http://dx.doi.org/10.1117/12.2274249.

Poikela, T., Plosila, J., Westerlund, T., Campbell, M., Gaspari, M.D., Llopart, X., Gromov, V., Kluit, R., van Beuzekom, M., Zappon, F., Zivkovic, V., Brezina, C., Desch, K., Fu, Y., Kruth, A., 2014. Timepix3: a 65K channel hybrid pixel readout chip with simultaneous ToA/ToT and sparse readout. J. Instrum. 9 (05), C05013. http://dx.doi.org/10.1088/1748-0221/9/05/C05013.

Procz, S., Avila, C., Fey, J., Roque, G., Schuetz, M., Hamann, E., 2019. X-ray and gamma imaging with Medipix and Timepix detectors in medical research. Radiat. Meas. 127, 106104. http://dx.doi.org/10.1016/j.radmeas.2019.04.007.

Stehlikova, V., Urban, M., Nentvich, O., Daniel, V., Sieger, L., Tutt, J., 2017. Hard X-ray Vela supernova observation on rocket experiment WRX-R. Contributions Astron. Obs. Skalnaté Pleso 47 (2), 165–169.

Uher, J., Jakubek, J., 2011. Equalization of Medipix2 imaging detector energy thresholds using measurement of polychromatic X-ray beam attenuation. J. Instrum. 6 (11), C11012. http://dx.doi.org/10.1088/1748-0221/6/11/c11012.

Unwin, M., Jales, P., Tye, J., Gommenginger, C., Foti, G., Rosello, J., 2016. Spaceborne GNSS-reflectometry on TechDemoSat-1: Early mission operations and exploitation. IEEE J. Sel. Top. Appl. Earth Obs. Remote Sens. http://dx.doi.org/10.1109/JSTARS.2016.2603846.

Urban, M., Doubravova, D., Nentvich, O., 2020a. Thermal vacuum testing of Timepix3 detector. J. Instrum. 15 (03), C03040. http://dx.doi.org/10.1088/1748-0221/15/03/C03040.

Urban, M., Nentvich, O., Baca, T., Vertat, I., Marsikova, V., Doubravova, D., Daniel, V., Inneman, A., Pina, L., McEntaffer, R.L., Schultz, T.B., Miles, D.M., Tutt, J.H., 2020b. REX: X-ray experiment on the water recovery rocket. arXiv:2011.10072 (Preprint).

Urban, M., Nentvich, O., Stehlikova, V., Baca, T., Daniel, V., Hudec, R., 2017. VZLUSAT-1: Nanosatellite with miniature lobster eye X-ray telescope and qualification of the radiation shielding composite for space application. Acta Astronaut. 140, 96–104. http://dx.doi.org/10.1016/j.actaastro.2017.08.004.

van der Boog, R.P.M., 2013. Energy calibration procedure of a pixel detector (Ph.D. thesis). The Hague University of Applied Sciences, p. 42.

Watt, J., Davidson, D., Johnston, C., Smith, C., Tlustos, L., Mikulec, B., Smith, K., Rahman, M., 2003. Dose reductions in dental X-ray imaging using Medipix. In: Proceedings of the 6th International Conference on Position-Sensitive Detectors. Nucl. Instrum. Methods Phys. Res. A 513 (1), 65–69. http://dx.doi.org/10.1016/j.nima.2003.08.003.

Whyntie, T., Harrison, M., 2014. Simulation and analysis of the LUCID experiment in the Low Earth Orbit radiation environment. J. Phys. Conf. Ser. 513 (2), 022038. http://dx.doi.org/10.1088/1742-6596/513/2/022038.

Whyntie, T., Harrison, M., 2015. Full simulation of the LUCID experiment in the Low Earth Orbit radiation environment. J. Instrum. 10 (03), C03043. http://dx.doi.org/10.1088/1748-0221/10/03/C03043.

3.3   Energy mode

Timepix detectors are capable of measuring the deposited energy of radiation in individual pixels of the radiation-sensitive sensor used. This capability is achieved in the Time-over-Threshold mode of measurement, where the required discharge time of the deposited charge is measured within the electronics of each pixel. This time value can then be converted by a known transformation, the output of the energy calibration of the detector, into information about the energy of the radiation, thus providing a spectral analysis of the incident radiation. For this reason, several calibration methods have been described, e.g. using X–ray fluorescence and low energy gamma ray sources [34], internal test pulses [35, 36], protons [37–39] or alpha particles [40, 41]. In this study, the detectors were equipped with a conventional per-pixel calibration using XRF sources. This calibration method provides good coverage of the energy range up to about 500 keV. In this range the ToT and the energy follow a linear relationship. This is not the case for low energies up to about 10 keV to 15 keV [39, 41], where the conversion characteristic is strongly non-linear (see Figure 3.8).
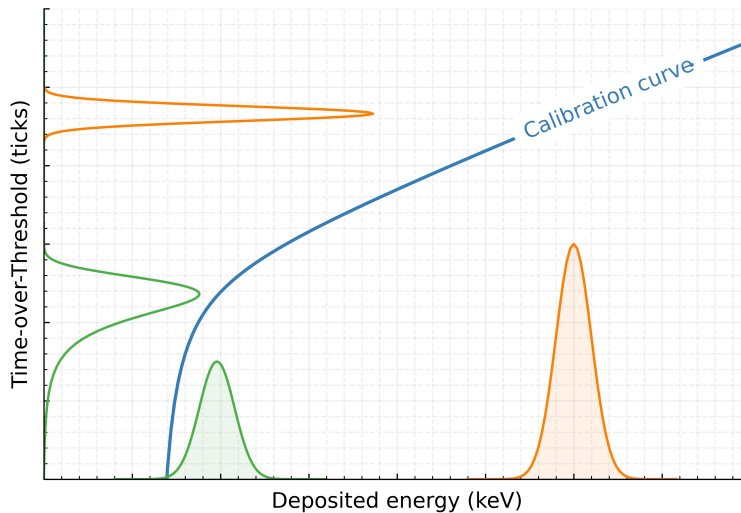
Fig. 3.8: Dependence on particle energy of the Time-over-Threshold signal.

With the ToT measurement mode, there is a risk that the measured energy spectrum will be distorted by multiple hits to the same pixel during an acquisition time. At this point, a pile-up occurs and the read data cannot uniquely identify the true value of the particle energy interaction. In the hybrid pixel detectors, there are two types of the pile-up. A digital pile-up occurs when another particle hits the same pixel before the value of the previous measurement is read. The second type is analogue pile-up, which occurs when the CSA signals from two or more particles overlap and are consequently evaluated as a single pulse. In both cases, the energy of the individual hits cannot be correctly distinguished. This is the most common source of distortion when measuring ToT in frame mode.

The TPX3 detector provides a data-driven approach to reading ToT data. In this case, the measured data from each pixel is transferred as a data stream as soon as it is registered. This measurement method has great potential not only for spectral analysis but also for imaging within a single measurement if the data is appropriately processed. Therefore, Time-over-Threshold was chosen to focus on for further applied research.

The initial phase involved functional testing and thermal analysis of this particular type of detector. The tests were carried out over a wide range of operating temperatures, from $10\,°\text{C}$ to $70\,°\text{C}$, using characteristic XRF radiation and radionuclides in the energy range from $8\,\text{keV}$ to $81\,\text{keV}$. During individual measurements, a deviation in the detected energy values of the detector was observed, which was attributed to temperature fluctuations of the detector. The results indicated that the spectral drift trend did not match the detected drift in the case of the EC measurement mode. Specifically, a shift towards higher energy values was observed with increasing temperature. In contrast, in the case of the Time-over-Threshold measurement mode, the observed energy spectrum shifted towards lower energies. Consequently, the relative error of the measurement was found to exceed $-30\,\%$.

After analysing the observed dependencies, a new method for correcting the measured energy deviation was proposed. This compensation method was found to be efficient as it significantly reduces the temperature drift of the energy spectrum when the detector is subjected to a constant temperature difference during the measurement compared to the calibration temperature. By applying this method to the Europium spectrum, the absolute measurement accuracy error improved from $-3.07\,\text{keV}$ to $0.04\,\text{keV}$ for a detector temperature of $40\,°\text{C}$, and from $-11.99\,\text{keV}$ to $0.28\,\text{keV}$ for a temperature of $70\,°\text{C}$. Correspondingly, the relative measurement error decreased from $-7.7\,\%$ and $-30.0\,\%$ to $0.1\,\%$ and $0.7\,\%$, respectively.

M. Urban, O. Nentvich, L. Marek, R. Hudec, and L. Sieger, "Timepix3: Temperature Influence on Radiation Energy Measurement with Si Sensor," *Sensors*, vol. 23, no. 4, p. 2201, Feb. 2023. DOI: `10.3390/s23042201`

In order to perform a more comprehensive analysis of the Timepix3 detector, an expanded set of detectors and radiation sources were used in this study. Thermal vacuum tests were also conducted to extend the temperature range to below zero ($-40\,°\text{C}$). The results confirmed previous findings but revealed that at lower temperatures, the dependence of the spectral drift on temperature lost its monotonicity and the direction of the drift was reversed.

Using this more detailed dataset, the TPX3 detector was characterised, and a new correction function was proposed. This correction function not only considers the thermal analysis results but also takes into account the energy dependence of the drift. By mathematically characterising these two dependencies and substituting them, it is possible to recover the proper values of the energy spectrum based on measured data, temperature information, and several constants. This correction method was verified on a set of examined detectors over the entire temperature and radiation energy range. Applying the new complex method reduces the relative measurement error from over $-30\,\%$ to less than $1.5\,\%$ over the whole range without temperature stabilisation. For example, the correction of the relative error measured by the XRF Tantalum target ($57.53\,\text{keV}$) has improved from $-24.49\,\%$ to $-0.97\,\%$ at $60\,°\text{C}$ on the detector. In other words, the absolute error has decreased from almost $15\,\text{keV}$ to less than $0.6\,\text{keV}$.

M. Urban, O. Nentvich, L. Marek, D. Hladik, R. Hudec, and L. Sieger, "Timepix3: Compensation of Thermal Distortion of Energy Measurement," *Sensors*, vol. 23, no. 6, p. 3362, Mar. 2023. DOI: `10.3390/s23063362`

Furthermore, a generalisation of the correction model was proposed and tested for applications beyond the measured range. The results were verified on a detector outside the training set and in a vacuum chamber. Overall, this study provides a new complex correction method for thermal distortion of energy measurement in TPX3 detectors, which can improve energy measurement accuracy in a wide temperature range.

sensors

MDPI

Article

Timepix3: Temperature Influence on Radiation Energy Measurement with Si Sensor

Martin Urban [1,*] , **Ondrej Nentvich** [1] , **Lukas Marek** [2,3] , **Rene Hudec** [1] **and Ladislav Sieger** [1]

1   Faculty of Electrical Engineering, Czech Technical University in Prague, Technicka 2,
     166 27 Prague 6, Czech Republic
2   Faculty of Mathematics and Physics, Charles University, V Holesovickach 2, 180 00 Prague 8, Czech Republic
3   Advacam, s.r.o., U Pergamenky 1145/12, 170 00 Prague 7 , Czech Republic
*   Correspondence: martin-urban@fel.cvut.cz

Abstract: The Timepix3 readout ASIC chip is a hybrid pixelated radiation detector, designed at CERN, which contains a 256 px×256 px matrix. Each of the 65,536 radiation-sensitive pixels can record an incoming particle, its energy deposition or time of arrival and measure them simultaneously. Since the detector is suitable for a wide range of applications from particle physics, national security and medicine to space science, it can be used in a wide range of temperatures. Until now, it has to be calibrated every time to the operating point of the application. This paper studies the possibility of energy measurement with Timepix3 equipped with a 500 μm thick silicon sensor and MiniPIX readout interface in the temperatures between 10 °C and 70 °C with only one calibration. The detector has been irradiated by X-ray fluorescence photons in the energy range from 8 keV to 57 keV, and 31 keV to 81 keV photons from the ^{133}Ba radioactive source. A deviation of 5% in apparent energy value may occur for a 10 °C change in temperature from the reference point, but, with the next temperature change, it can reach up to −30%. Moreover, Barium photons with an energy of 81 keV appear as deposited energy of only 55 keV at a detector temperature of 70 °C. An original compensation method that reduces the relative measurement error from −30% to less than 1% is presented in this paper.

Keywords: Timepix3; X-ray detector; energy measurement; temperature effects; compensations

check for **updates**

1. Introduction

Due to the Timepix3 (TPX3) hybrid structure, these detectors may be used in a wide range of scientific and industrial fields. Detectors from the Medipix and Timepix family are often used for X-ray imaging [1], dosimetry, or as an environmental radiation monitor. The detectors' high-resolution imaging capabilities are applicable to the analysis of paintings and sculptures [2,3] as well as mammography [4], dental imaging [5] and CT scans [6]. Significant applications include X-ray inspection of material joints and faults and the localisation of radiation sources [7,8]. The TPX3 detector, in combination with a suitable converter, can also be used for neutron detection of both D-D and D-T sources. This has been demonstrated in previous research studies [9,10], which have shown its effectiveness in detecting both fast and thermal neutrons.

The predecessors of TPX3 were used in scientific instruments such as ATLAS [11], the suborbital rocket campaign [12–14] and the following satellites: PROBA-V with SATRAM experiment [15–17]; British TechDemoSat-1 with LUCID experiment [18]; Czech CubeSat VZLUSAT-1 [19–21] and RISEPix on the RISESAT microsatellite [22].

In many applications, the detectors undergo thermal changes in the environment and thus in the detector's structure. Temperature stability and known dependence of device behaviour on temperature are important in the case of the TPX3 detector as well as in the case of most modern semiconductor sensors.

The accuracy of the resulting energy measurements is closely related to the conditions under which the measurement was made or their likeness to the conditions under which

the detector was calibrated. For this reason, several calibration methods have already been described, e.g., using X-ray fluorescence (XRF) and low-energy gamma rays radiation sources [23], internal test pulses [24,25], protons [26,27], or alpha particles [28,29].

Since the detector can be used in many applications and in various environments, significant changes in operating temperatures of up to tens of degrees Celsius can occur. Achieving standard measurement conditions (identical to calibration conditions) can be challenging. Temperature stabilisation in the target application can also be very power-demanding, especially for space usage. The characterisation of the detector and the description of its temperature dependencies are essential to minimising the distortion of the measured data.

Many articles mention the possible applications of TPX3; however, there are only a few papers that describe the characterisation of the detector in a variable environment or on measurement mode [30,31]. This manuscript presents the results of temperature tests during radiation energy measurements performed with the MiniPIX Timepix3 detector. The tests were conducted over a wide operating temperature range from 10 °C to 70 °C. The characterisation was realised using XRF and a radiation source in the energy range from 8 keV to 81 keV. Based on the observed dependencies, a linear correction of the measured energy deviation was proposed and presented in the final part of this paper.

The remaining part of the article is divided into several sections. Section 2 contains a brief description of the detector and the detection principle. Next, Section 3 describes the setup, materials, radiation sources and methods used. Section 4 presents the detector's temperature dependence and the effect of temperature drift on the acquired energy spectra using several parameters, such as the accuracy of the measurement. Section 5 presents and proposes a novel method for linear correction of the detected temperature distortion of the energy spectra. Section 6 is devoted to a final summary of the observed phenomena, properties and presented methods.

2. Detector Description

The TPX3 is a hybrid active pixel detector with a semiconductor detection layer. This detection chip was developed at CERN as a successor to the Timepix chip [32] in the Medipix collaboration. The TPX3 is a Complementary Metal–Oxide–Semiconductor (CMOS) type of detector with a square matrix of 256 px×256 px and a pixel pitch of 55 µm [33]. The device contains a readout Application-Specific Integrated Circuit (ASIC) chip on which a semiconductor sensor layer is bump-bonded. Within the ASIC, there are integrated electronics to sense and evaluate the signal from each pixel. The energy threshold discriminator, integrated in ASIC, is used to eliminate noise (identified as low energy events); therefore, it is possible to generate a noise-free system when the calibration and equalisation are performed.

The ASIC allows independent reading of individual pixels in data-driven readout mode, where only the hit pixels are read out continuously during the exposure time. In this readout mode, the detector can have virtually zero dead time, but individual pixels still have about 475 ns dead/readout time, extended with time for the discharging of accumulated charge.

The TPX3 ASIC can operate all the 65,536 px in one of the following modes:

Time-of-Arrival (ToA) mode —measurement of the particle impact time to the detector. That is, the time it takes to reach the Threshold (THL) level from the beginning of the exposure time.

Time-over-Threshold (ToT) and ToA mode—combination of simultaneous ToA and deposited energy measurements. The measurement of the deposited energy in a pixel from the incident particle is based on the Wilkinson-type Analogue-to-Digital Converter (ADC). The sensed energy depends on the number of clock ticks during which the signal is above the preset discrimination level (Threshold). The Time-over-Threshold relies on the time (number of clock ticks) it takes to discharge the accumulated charge in each pixel by a constant current.

Event counting and integral ToT mode—the count of events and their integrated charge in each pixel during the common exposure time. Only events generating the charge above the discrimination level are sensed.

This paper examines the effect of temperature on the measurement of deposited energy in the ToT and ToA mode via data-driven readout. A simplified diagram of the measurement principle is shown in Figure 1.
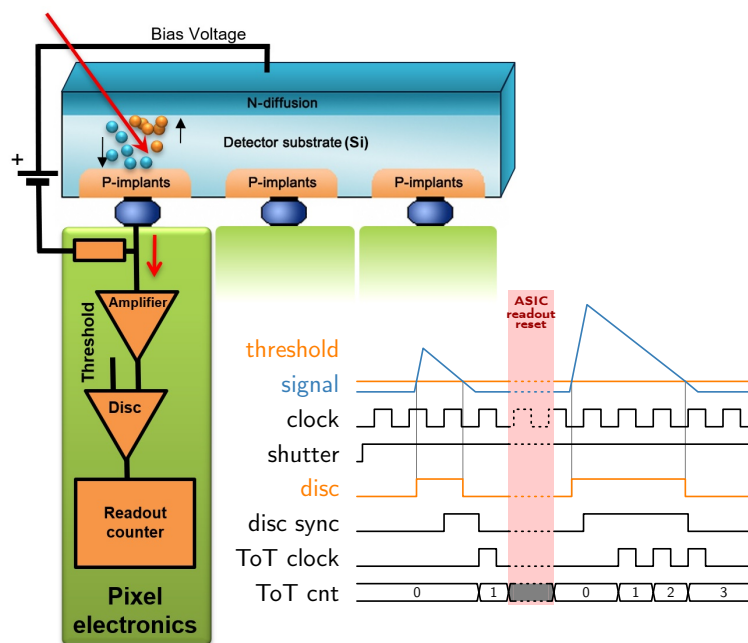

Figure 1. Schematic representation of Timepix3 detector function in Time-over-Threshold measurement.

One of the advantages of Timepix3 operated in the data-driven readout mode is the possibility of acquiring complete information about the interaction of the particles immediately after its impact to the detector [33]. Within the collected data stream, the ToA, ToT values and pixel coordinate information are available for each interaction in the presented case. The detection layer for the Medipix/Timepix detector family can be made of different semiconducting or semi-insulating materials, such as Si, GaAs, CdTe, CZT, etc., in combination with the same ASIC chip due to their hybrid structure. The monolithic sensing layer can have various thicknesses, typically ranging from $100\,\mu m$ to $2000\,\mu m$, depending on the application and its energy detection range, but the thickness within the sensor is constant with respect to manufacturing precision.

3. Measurement and Methods

The data presented in this paper were collected during measurements with three MiniPIX TPX3 detectors equipped with a $500\,\mu m$ Si sensor with $200\,V$ bias voltage applied. The detectors were thermally coupled to the Peltier plate using a thermally conductive tape between the detector and the cold/heat plate, and the whole mounting was secured by Kapton tape. Temperature stabilisation of the cold/heat plate was conducted at several temperatures in a range from $10\,°C$ to $70\,°C$ with $10\,°C$ steps. This temperature range is suitable for testing radiation detectors as it covers a wide range of temperatures representative of different environments and hence a significant part of their applications such as laboratory, medical, industrial, outdoor and some applications in space. The temperature of the cold/heat plate was controlled and monitored by a feedback temperature sensor. Since the thermometers provided by the manufacturer in the Timepix3 ASIC are uncalibrated, the sensed values throughout the tested detectors were inaccurate by several degrees of Celsius. Therefore, an external thermometer connected by the four-wire method

was chosen for temperature measurement, which was thermally coupled to minimise the potential temperature gradient. After reaching the target temperature, the detectors were temperature stabilised for at least 10 min before each set of measurements was performed. Each measurement set contains a series of energy spectrum measurements in the ToT and ToA data-driven mode for individual sources of radiation. During the measurements, the setup was placed in a shielded X-ray box equipped with an X-ray tube and holder for X-ray fluorescence targets. The arrangement of the experiment, including details of the measurement setup, is shown in Figure 2.
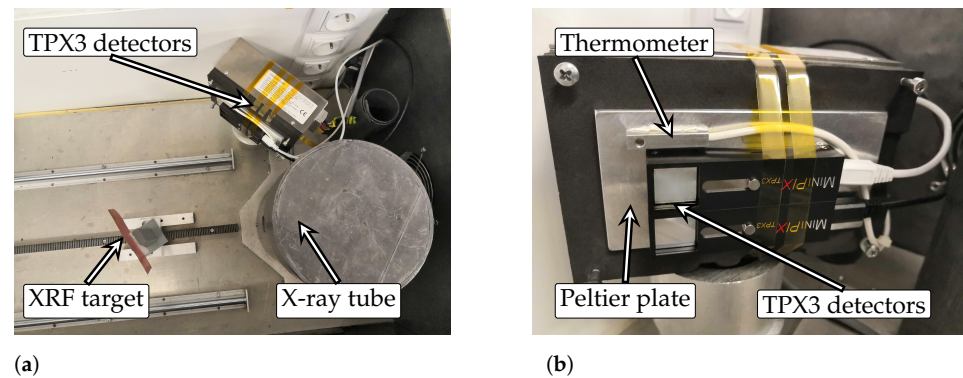

(**a**) (**b**)

Figure 2. Detector arrangement for thermal testing of the Timepix3 detectors. (**a**) arrangement configuration for X-ray fluorescence measurement; (**b**) details of the detector placement on the Peltier module with feedback thermometer.

Four materials (Cu, Mo, In, Ta) were selected as targets for the generation of the characteristic radiation generated by X-ray fluorescence. The advantage of XRF is its precise definability of the individual spectral lines. The fifth (last) tested source is a radioisotope of Barium which adds spectral peaks in the tested energy range. All used sources of radiation and their characteristic energies are listed in Table 1.

Table 1. List of radiation sources and target materials with their characteristic energies.

Symbol	Element	Energy
Cu	Copper	8.046 keV
Mo	Molybdenum	17.480 keV
In	Indium	24.209 keV
Ta	Tantalum	57.532 keV
^{133}Ba	Barium	30.973 keV
		80.998 keV

With the usage of a well-defined radiation source, it is possible to measure and determine changes in the detector's response to clearly defined stimuli and thus establish its dependence on external conditions such as temperature. The spectral peaks (Figure 3) are fitted by a $G_{erfc(x;A_1,A_2,\mu,\sigma)}$ (Equation (1)) function which is a combination of Gaussian $G_{(x;A_1,\mu,\sigma)}$ (Equation (2)), which represents radiation peak, with complementary error function $E_{rfc}(x)$ (Equation (3)) as a representation of decreasing characteristics of the measured energy spectrum. This approximation is used to determine the position of the peak centre μ and σ as its standard deviation. The x is the value of deposited energy:

$$G_{erfc(x;A_1,A_2,\mu,\sigma)} = G_{(x;A_1,\mu,\sigma)} + A_2 \cdot E_{rfc}\left(\frac{x-\mu}{\sigma\sqrt{2}}\right) \tag{1}$$

where

$$G_{(x;A_1,\mu,\sigma)} = A_1 \cdot e^{\frac{-(x-\mu)^2}{2\sigma^2}} \tag{2}$$

and

$$E_{rfc}(x) = 1 - \frac{2}{\sqrt{\pi}} \int_0^x e^{-t^2} dt. \tag{3}$$
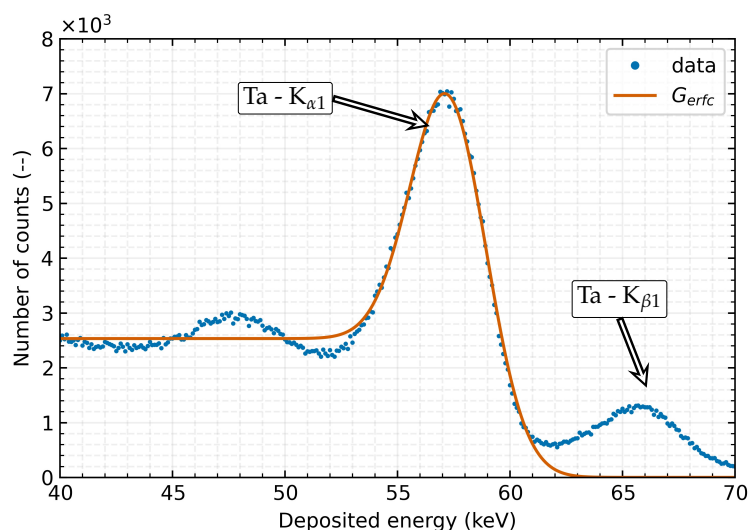

Figure 3. Measured spectral peak generated by the X-ray fluorescence of a tantalum target. The measured data (blue line), together with the result of the applied G_{erfc} function fit on the Ta-$K_{\alpha1}$ XRF peak (orange line), are shown on the graph. The TPX3 detector with a 500 µm Si detection layer was stabilised at 30 °C throughout the measurement.

The procedure for obtaining the measured energy spectra includes clustering of each event, which takes into account multi-pixel clusters and reconstructs their original energy. The examined detectors were calibrated as part of the standard manufacturing procedure before the characterisation starts. The calibration procedure consists of several steps such as threshold equalisation, which compensates for non-uniformities within the pixel matrix. This is followed by a global calibration of the threshold energy, which consists of a measurement series depending on the sequential change of the applied threshold for several monochromatic radiation energies, and Time-over-Threshold calibration for per pixel energy measurement. The THL calibration procedure is described in Urban and Doubravová [31] as well as ToT energy calibration in Jakubek [23].

4. Thermal Dependency

This chapter describes some of the main parameters such as *Absolute measurement accuracy*, *Relative error of measurement*, and *Relative energy resolution* of the Timepix3 detectors equipped with a Si sensor and their temperature dependence. Several sets of measurements were used for the evaluation. Temperature fluctuations during the measurement affect the detector output and distort the evaluated data. The used data sets include measurements of energy spectra from XRF sources as well as from natural sources (see Table 1), and all tested detectors were sequentially thermally stabilised in several steps (10 °C, 20 °C, ..., 70 °C).

The measured set for one detector, one measured energy (same XRF target) with constant X-ray tube setting and different temperatures is shown in Figure 4a. For a more explicit presentation of the thermal effect on the accuracy of the energy measurement at different energies, see Figure 4b. For clarity, the individual spectral peaks are represented by a normalised Gaussian curve, making recognising the resulting distortion in the energy spectrum clearer.
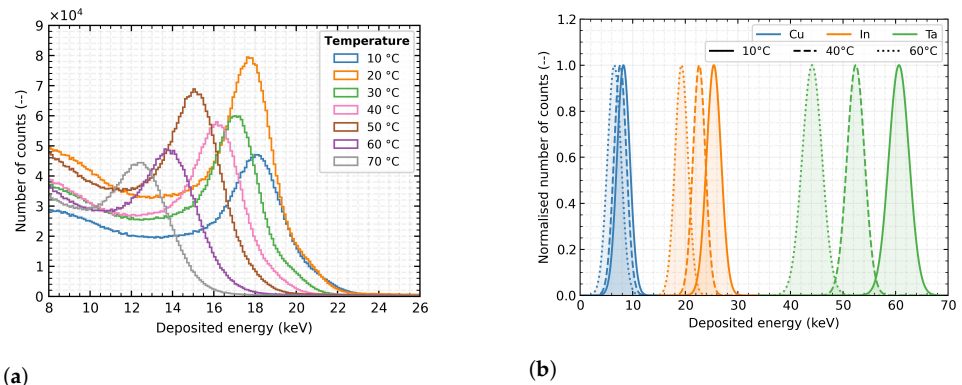
(**a**)   (**b**)

Figure 4. The thermal influence on energy measurement. (**a**) the set of spectral measurements depends on the detector temperature from 10 °C to 70 °C for constant settings of the X-ray tube with the Molybdenum XRF target; (**b**) visualisation of the temperature effect on the measured incident radiation energy. Normalised Gaussian curves represent the individual spectral peaks for better clarity. The detector was calibrated for 20 °C.

According to the manufacturer, the most common calibration of these detectors is performed at a temperature of 20 °C. Therefore, the measurements at this temperature are used as a reference for the subsequent evaluation. The numerical subscripts given in the formulas below are used as a reference for the measurement temperature.

4.1. Absolute Measurement Accuracy

The first evaluated parameter is the absolute measurement accuracy, which is defined as the absolute shift of the measured energy of the incident radiation (Equation (4)), where μ_x is the position of the measured peak centre at temperature x and μ_{20} is the mean position at 20 °C:

$$\Delta\mu = \mu_x - \mu_{20} \tag{4}$$

The results indicate that, with increasing detector temperature, the sensed energy shifts toward lower values. Thus, the accuracy of the measurement decreases, and this effect is more significant as the energy of the incident radiation increases (see Figure 5). As can be seen, when the detector was heated up to 70 °C from the reference 20 °C, the measured energy peaks were shifted by -2.10 keV at 8.05 keV, -9.67 keV at 30.85 keV, and -27 keV at 81 keV.
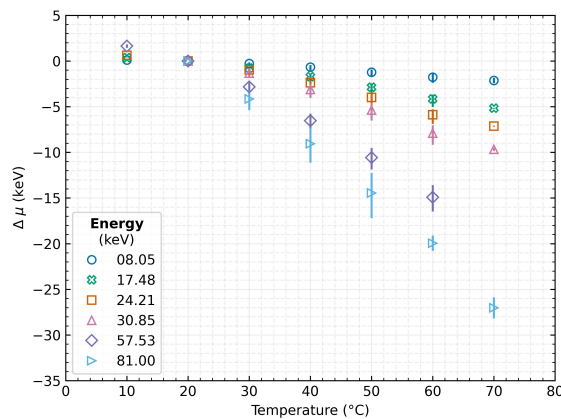

Figure 5. Absolute shift of the spectral peak for a given energy with respect to the detector's temperature. The data represent the mean values over the tested detectors, and the error bars indicate their minimum and maximum value.

4.2. Relative Error of Measurement

Following the change in the absolute accuracy of the measurements, the relative percentage error of the measurements for the individual energies was also evaluated:

$$RE_{20} = \frac{\mu_x - \mu_{20}}{\mu_{20}} \cdot 100\% \tag{5}$$

This evaluation (see Figure 6) led to the finding that the resulting accuracy of the measurement is not as significantly dependent on the energy of the incident radiation as it might appear from Figure 5. However, the energy dependence still persists, and the temperature change has a more significant effect at higher energies (for 30 °C −3.36% at 8.0 keV vs. −4.79% at 57 keV). Therefore, the relative error of the measurement is within 5% when the detector is warmed by 10 °C. However, as the temperature rises, the distortion of the detected peak increases as well, up to −26.8% at 8.0 keV and −32.4% at 81 keV at 70 °C. According to the results presented in this section, it is evident that the percentage error in measurement accuracy increases rapidly with rising detector temperature and reaches 30% when a sensor is heated to 70 °C.
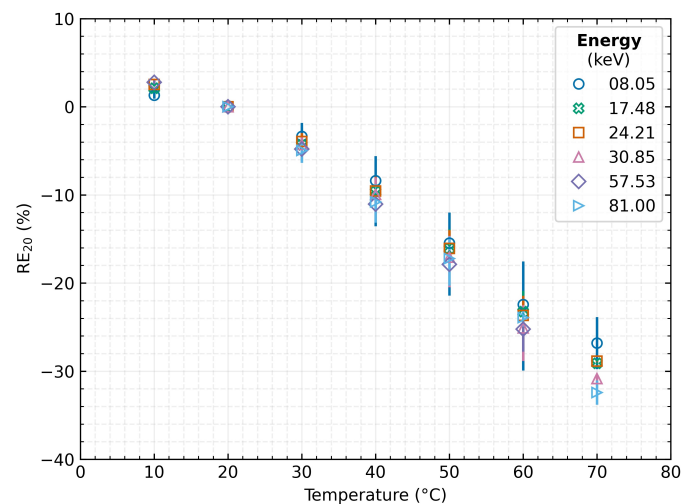

Figure 6. Dependence of the relative measurement error on the detector temperature for different energies of incident radiation. The plotted data represent the mean values over the tested detectors, and the error bars indicate their minimum and maximum value.

4.3. Relative Energy Resolution

Finally, the energy resolution was evaluated according to Equation (6) as well as its dependence on temperature. The definition of energy resolution implies that the lower the percentage value of the quantity, the better the resulting resolution. For the calculation, the accurate material energy E and evaluated Full Width at Half Maximum (FWHM) of the measured peak is always used from each measurement set. For the purpose of this evaluation, the FWHM is defined as $FWHM_x = 2\sqrt{2\ln 2}\sigma_x$, i.e., $\approx 2.35\sigma_x$. The subscript x represents, the same as in the previous cases, the temperature corresponding to the particular measurement:

$$Re = \frac{FWHM_x}{E} \cdot 100\% \tag{6}$$

The characteristics in Figure 7a represent the dependence of energy resolution on sensor temperature for several radiation sources.

In the range from 20 °C to 40 °C, there is only a minor effect of the sensor temperature on the spectral resolution of the measured signal. Change of the energy resolution is within

0.5% over the entire tested spectral range. As the temperature increases, the spectral peaks widen, so the energy resolution gradually decreases.

Nevertheless, the energy resolution improves significantly with increasing radiation energy (Figure 7b), which is consistent with the theoretical assumptions and confirms measurements in Nowak et al. [30]. This figure is also expanded by comparison of the trends at two measured temperatures, where there is a clear tendency of declining spectral resolution with dependence on increasing detector temperature.
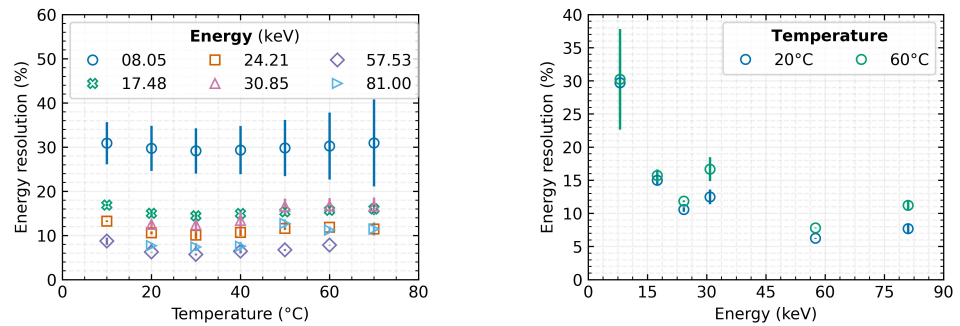
(**a**) (**b**)

Figure 7. The energy resolution of Timepix3 detector with 500 μm Si sensor. The plotted data represent the mean values over the tested detectors, and the error bars indicate their minimum and maximum value. (**a**) dependence on detector temperature; (**b**) dependence on radiation energy.

5. Linear Compensation

Based on the presented energy dependencies of the MiniPIX TPX3 detector, a global correction of the energy spectra can be proposed. The correction method is based on the knowledge of the measurement accuracy evolution depending on the detector temperature for individual incident radiation energies (see Section 4.1).

As can be seen in Figure 8, a linear function can be established for different stable temperatures of operation. A control measurement was performed to validate the proposed method with the detector stabilised at 40 °C and 70 °C and using the ^{152}Eu radionuclide (39.91 keV) as the radiation source. This radiation source is not included in the data set of measurements based on which the correction function was determined.
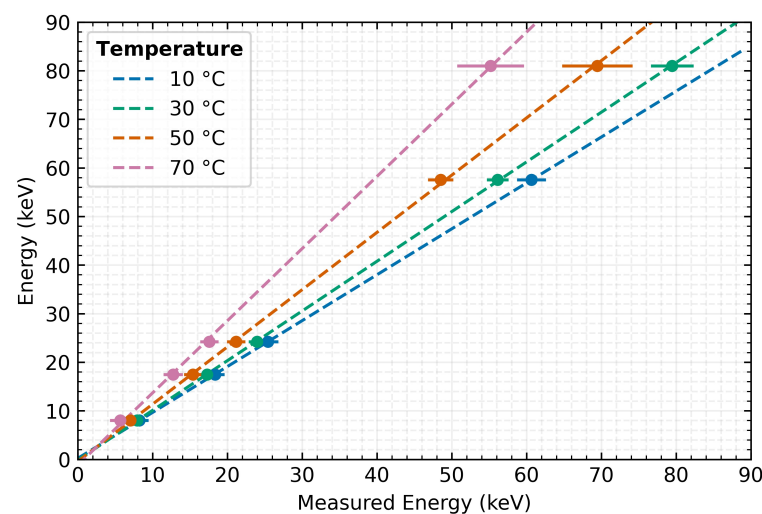

Figure 8. The correction functions for the global energy spectra of one of the tested detectors. Error bars represent the standard deviation of the measured value of the energy maximum.

Figure 9 clearly shows the influence of measuring the same radiation source at different temperatures and indicates the effect of the correction on the measured spectra. The same already presented fit model as in the previous cases is used for the evaluation. The results show that the application of the correction successfully compensates for the temperature distortion of the measurement accuracy. Applying the proposed linear correction method to the measured data improved the absolute measurement accuracy error from $-3.07\,\text{keV}$ to $0.04\,\text{keV}$ for $40\,^\circ\text{C}$ detector temperature and from $-11.99\,\text{keV}$ to $0.28\,\text{keV}$ for $70\,^\circ\text{C}$. Corresponding to these changes, the relative measurement error decreases from -47.7% and -30.0% to 0.1% and 0.7%, respectively. However, even after the application of the correction, the energy resolution is degraded by rising detector temperature causing an increasing FWHM of the spectral peak. In the above case, the change in resolution (after correction) is from 16% at $40\,^\circ\text{C}$ to 24% at $70\,^\circ\text{C}$. The obtained energy spectrum at the validation temperatures corresponds persistently to the radiation energy of the applied radiation source.
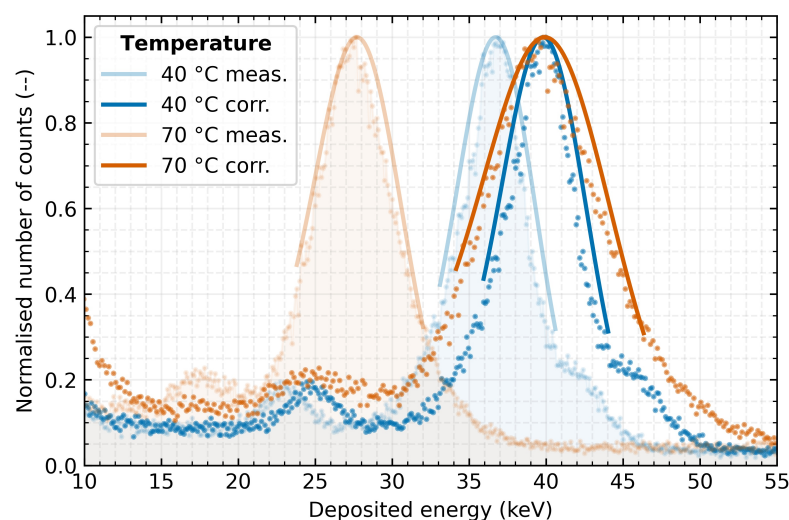

Figure 9. Measurement of the Europium radionuclide energy spectrum with the detector at $40\,^\circ\text{C}$ and $70\,^\circ\text{C}$. Comparison of measured energy spectra before (light curves) and after linear correction (dark curves) according to dependencies in Figure 8.

6. Conclusions

This manuscript presents the results of the Time-over-Threshold response characterisation of Timepix3 detectors with the MiniPIX readout interface, exposed to various temperature and radiation conditions. The tested detectors were equipped with a $500\,\mu\text{m}$ thick silicon sensor and stabilised at various temperatures in the range from $10\,^\circ\text{C}$ to $70\,^\circ\text{C}$, where they were exposed to X-ray radiation in the energy range from $8\,\text{keV}$ to $81\,\text{keV}$.

Based on the performed experiments, it was found that the distortion of the measured signal does not depend only on the detector temperature but also on the energy of the incident radiation. It was observed that, as the temperature increases, the measured energy spectrum systematically drifts towards lower energy values of sensed energy. The absolute energy shift is dependent on the energy value of the incident particles and becomes more significant as their energy increases. This shift can cause an absolute error of several tens of kilo-electron volts, which means a relative measurement error of up to -30% in the tested energy/temperature set.

According to Mazziotta [34], the temperature dependence of the electron–hole pair creation in the presented temperature range was found to be at most 0.55%. This suggests that the change in the pair creation energy has a minimal impact.

Analysis of the energy resolution, which provides information about the detector's ability to distinguish two close spectral lines, shows that the energy resolution strongly depends on the incident energy. As the value of relative resolution decreases, the ability to recognise tight spectral lines from each other grows as the energy of the impacting particles increases. Based on the analysis, it can be noticed that the detected deviation of the energy resolution over the tested X-ray fluorescence energies does not exceed 2% for temperatures from 20 °C to 40 °C, respectively 5% over the whole range of tested temperatures. Therefore, this kind of detector proves significant spectral resolution stability over a 20 °C temperature range, with only minor changes.

Previous studies indicate that an increase in temperature difference, both positive and negative, can result in a disruption of the homogeneity of the equalisation matrix [35,36] because of differences in leakage current in each pixel and its effect on electronics, leading to a non-uniform distribution of pixel noise throughout the full frame and possibly a widening of peaks in the energy spectrum.

Other important elements that can affect energy measurement are noise sources. The most significant noise sources include shot noise, thermal noise and flicker noise. In dependence on the type and the noise generation method, its intensity and other characteristic properties may depend on the device's temperature [37–39].

To the best of our knowledge, this paper is the first which describes the temperature dependence of the energy measurement using the Timpeix3 detector and, based on its characterisations, is the first in the literature to propose and describe the correction method for the constant offset from the calibration temperature. The fast and efficient correction method uses the observed linear dependence of the measurement error. The presented method allows for reducing the degradation of the absolute accuracy of the measurement below 0.5 keV. For the validation measurement on the ^{152}Eu sample, which was not included in the modelling set, a reduction of the relative measurement error to 0.7% from the original -30% was achieved with this method. However, there is still a degradation of FWHM with increasing temperature.

Based on the presented results and the fact that mainly the position of each energy peak changes (change of the measurement accuracy), it can be inferred that the primary source of measurement variation is the electronics and the ASIC chip rather than the semiconductor sensor itself. The characteristics of the observed detector's distortion suggest that the change in temperature may cause a shift in the threshold or a gain in the detection system. One of the potential sources of inaccuracies might be the temperature instability of the voltage reference in combination with the temperature drift of integrated semiconductor components such as transistors and operational amplifiers within the ASIC chip. The complex combinations of these effects can cause a self-rising value of the applied threshold on the measurement (number of clock ticks) and thus lead to a detected drift of the measured energies towards lower values.

For future research, it is recommended to focus on the identification of the source of the detected distortions and minimise it, for example, by successive testing of a separate readout chip or simulating its temperature sensitivity in collaboration with the designers. The stability of the electronics, in addition to proposing a complex correction method to minimise the effect of temperature, could be another target.

The presented results show the importance of recording the temperature during the experiment and its impact on the overall result and accuracy of the measurements. It should be noted that some measurements under presented environmental conditions are outside the manufacturer's stated operating temperature range but may occur in some of the more demanding applications, and detectors' responses to environmental parameters may reveal different dependencies for different materials and thicknesses, which were not part of the study. Nevertheless, results indicate that TPX3 has potential not only for the laboratory but also in homeland security applications and space research.

References

1. Jakubek, J.; Cejnarova, A.; Holy, T.; Pospisil, S.; Uher, J.; Vykydal, Z. Pixel detectors for imaging with heavy charged particles. *Nucl. Instrum. Methods Phys. Res. Sect. Accel. Spectrometers Detect. Assoc. Equip.* **2008**, *591*, 155–158. [CrossRef]
2. Dudak, J. High-resolution X-ray imaging applications of hybrid-pixel photon counting detectors Timepix. *Radiat. Meas.* **2020**, *137*, 106409. [CrossRef]
3. Zemlicka, J.; Jakubek, J.; Kroupa, M.; Hradil, D.; Hradilova, J.; Mislerova, H. Analysis of painted arts by energy sensitive radiographic techniques with the Pixel Detector Timepix. *J. Instrum.* **2011**, *6*, C01066. [CrossRef]
4. Loaiza, L.; Roque, G.A.; Avila, C.A.; Mendoza, L.M.; Rueda, R.J.; Racedo, J.M. Feasibility study of a TIMEPIX detector for mammography applications. In Proceedings of the 13th International Conference on Medical Information Processing and Analysis, San Andres Island, Colombia, 5–7 October 2017; p. 30. [CrossRef]
5. Watt, J.; Davidson, D.; Johnston, C.; Smith, C.; Tlustos, L.; Mikulec, B.; Smith, K.; Rahman, M. Dose reductions in dental X-ray imaging using Medipix. *Nucl. Instrum. Methods Phys. Res. Sect. Accel. Spectrometers Detect. Assoc. Equip.* **2003**, *513*, 65–69. [CrossRef]
6. Dudak, J.; Zemlicka, J.; Krejci, F.; Polansky, S.; Jakubek, J.; Mrzilkova, J.; Patzelt, M.; Trnka, J. X-ray micro-CT scanner for small animal imaging based on Timepix detector technology. *Nucl. Instrum. Methods Phys. Res. Sect. Accel. Spectrometers Detect. Assoc. Equip.* **2015**, *773*, 81–86. [CrossRef]
7. Baca, T.; Stibinger, P.; Doubravova, D.; Turecek, D.; Solc, J.; Rusnak, J.; Saska, M.; Jakubek, J. Gamma Radiation Source Localization for Micro Aerial Vehicles with a Miniature Single-Detector Compton Event Camera. In Proceedings of the 2021 International Conference on Unmanned Aircraft Systems (ICUAS), Athens, Greece, 15–18 June 2021; pp. 338–346. [CrossRef]
8. Stibinger, P.; Baca, T.; Saska, M. Localization of Ionizing Radiation Sources by Cooperating Micro Aerial Vehicles With Pixel Detectors in Real-Time. *IEEE Robot. Autom. Lett.* **2020**, *5*, 3634–3641. [CrossRef]
9. Rubovič, P.; Bonasera, A.; Burian, P.; Cao, Z.; Fu, C.; Kong, D.; Lan, H.; Lou, Y.; Luo, W.; Lv, C.; et al. Measurements of D–D fusion neutrons generated in nanowire array laser plasma using Timepix3 detector. *Nucl. Instrum. Methods Phys. Res. Sect. Accel. Spectrometers Detect. Assoc. Equip.* **2021**, *985*, 164680. [CrossRef]
10. Granja, C.; Uhlar, R.; Chuprakov, I.; Alexa, P.; Sansarbayar, E.; Gledenov, Y.; Poklop, D.; Olsansky, V.; Marek, L.; Vuolo, M.; et al. Detection of fast neutrons with the pixel detector Timepix3. *J. Instrum.* **2023**, *18*, P01003. [CrossRef]
11. Bergmann, B.; Billoud, T.; Leroy, C.; Pospisil, S. Characterization of the Radiation Field in the ATLAS Experiment with Timepix Detectors. *IEEE Trans. Nucl. Sci.* **2019**, *66*, 1861–1869. [CrossRef]
12. Miles, D.M.; McEntaffer, R.L.; Schultz, T.B.; Donovan, B.D.; Tutt, J.H.; Yastishock, D.; Steiner, T.; Hillman, C.R.; McCoy, J.A.; Wages, M.; et al. An introduction to the water recovery x-ray rocket. In Proceedings of the International Conference on UV, X-Ray, and Gamma-Ray Space Instrumentation for Astronomy XX, San Diego, CA, USA, 6–8 August 2017; p. 28. [CrossRef]

13. Dániel, V.; Inneman, A.; Pína, L.; Zadražil, V.; Báča, T.; Stehlíková, V.; Nentvich, O.; Urban, M.; Maršíková, V.; McEntaffer, R.; et al. X-ray Lobster Eye all-sky monitor for rocket experiment. In Proceedings of the International Conference on EUV and X-ray Optics: Synergy between Laboratory and Space V, Prague, Czech Republic, 26–27 April 2017; p. 1023503. [CrossRef]

14. Urban, M.; Nentvich, O.; Báča, T.; Veřtát, I.; Maršíková, V.; Doubravová, D.; Dániel, V.; Inneman, A.; Pína, L.; Sieger, L.; et al. REX: X-ray experiment on the water recovery rocket. *Acta Astronaut.* **2021**, *184*, 1–10. [CrossRef]

15. Granja, C.; Polansky, S.; Vykydal, Z.; Pospisil, S.; Owens, A.; Kozacek, Z.; Mellab, K.; Simcak, M. The SATRAM Timepix spacecraft payload in open space on board the Proba-V satellite for wide range radiation monitoring in LEO orbit. *Planet. Space Sci.* **2016**, *125*, 114–129. [CrossRef]

16. Gohl, S.; Bergmann, B.; Granja, C.; Owens, A.; Pichotka, M.; Polansky, S.; Pospisil, S. Measurement of particle directions in low earth orbit with a Timepix. *J. Instrum.* **2016**, *11*, C11023. [CrossRef]

17. Gohl, S.; Bergmann, B.; Evans, H.; Nieminen, P.; Owens, A.; Posipsil, S. Study of the radiation fields in LEO with the Space Application of Timepix Radiation Monitor (SATRAM). *Adv. Space Res.* **2019**, *63*, 1646–1660. [CrossRef]

18. Furnell, W.; Shenoy, A.; Fox, E.; Hatfield, P. First results from the LUCID-Timepix spacecraft payload onboard the TechDemoSat-1 satellite in Low Earth Orbit. *Adv. Space Res.* **2019**, *63*, 1523–1540. [CrossRef]

19. Daniel, V.; Inneman, A.; Vertat, I.; Baca, T.; Nentvich, O.; Urban, M.; Stehlikova, V.; Sieger, L.; Skala, P.; Filgas, R.; et al. In-Orbit Commissioning of Czech Nanosatellite VZLUSAT-1 for the QB50 Mission with a Demonstrator of a Miniaturised Lobster-Eye X-Ray Telescope and Radiation Shielding Composite Materials. *Space Sci. Rev.* **2019**, *215*, 40. [CrossRef]

20. Urban, M.; Nentvich, O.; Stehlikova, V.; Baca, T.; Daniel, V.; Hudec, R. VZLUSAT-1: Nanosatellite with miniature lobster eye X-ray telescope and qualification of the radiation shielding composite for space application. *Acta Astronaut.* **2017**, *140*, 96–104. [CrossRef]

21. Baca, T.; Jilek, M.; Vertat, I.; Urban, M.; Nentvich, O.; Filgas, R.; Granja, C.; Inneman, A.; Daniel, V. Timepix in LEO Orbit onboard the VZLUSAT-1 Nanosatellite: 1-year of Space Radiation Dosimetry Measurements. *J. Instrum.* **2018**, *13*, C11010. [CrossRef]

22. Filgas, R.; Malich, M.; Kuwahara, T.; Broulím, J.; Holík, M.; Sakal, M.; Murata, Y.; Tomio, H.; Gohl, S.; Johan, M.; et al. RISEPix—A Timepix-based radiation monitor telescope onboard the RISESAT satellite. *Astron. Nachrichten* **2019**, *340*, 674–680. [CrossRef]

23. Jakubek, J. Precise energy calibration of pixel detector working in time-over-threshold mode. *Nucl. Instrum. Methods Phys. Res. Sect. Accel. Spectrometers Detect. Assoc. Equip.* **2011**, *633*, S262–S266. [CrossRef]

24. Turecek, D.; Jakubek, J.; Kroupa, M.; Soukup, P. Energy calibration of pixel detector working in Time-Over-Threshold mode using test pulses. In Proceedings of the 2011 IEEE Nuclear Science Symposium Conference Record, Valencia, Spain, 23–29 October 2011; pp. 1722–1725. [CrossRef]

25. Kroupa, M.; Jakubek, J.; Soukup, P. Optimization of the spectroscopic response of the Timepix detector. *J. Instrum.* **2012**, *7*, C02058. [CrossRef]

26. Kroupa, M.; Campbell-Ricketts, T.; Bahadori, A.; Empl, A. Techniques for precise energy calibration of particle pixel detectors. *Rev. Sci. Instrum.* **2017**, *88*, 033301. [CrossRef]

27. George, S.; Kroupa, M.; Wheeler, S.; Kodaira, S.; Kitamura, H.; Tlustos, L.; Campbell-Ricketts, T.; Stoffle, N.; Semones, E.; Pinsky, L. Very high energy calibration of silicon Timepix detectors. *J. Instrum.* **2018**, *13*, P11014. [CrossRef]

28. Holik, M.; Ahmadov, G.; Broulim, J.; Zich, J.; Berikov, D.; Mora, Y.; Kopatch, Y.; Nuruyev, S.; Abbaszada, N.; Zhumadilov, K. Alpha calibration of the Timepix pixel detector exploiting energy information gained from a common electrode signal. *J. Instrum.* **2019**, *14*, C06022. [CrossRef]

29. Sommer, M.; Granja, C.; Kodaira, S.; Ploc, O. High-energy per-pixel calibration of timepix pixel detector with laboratory alpha source. *Nucl. Instrum. Methods Phys. Res. Sect. Accel. Spectrometers Detect. Assoc. Equip.* **2022**, *1022*, 165957. [CrossRef]

30. Nowak, M.; Tlustos, L.; Carbonez, P.; Verdun, F.; Damet, J. Characterisation of the impacts of the environmental variables on Timepix3 Si sensor hybrid pixel detector performance. *Nucl. Instrum. Methods Phys. Res. Sect. Accel. Spectrometers Detect. Assoc. Equip.* **2020**, *981*, 164502. [CrossRef]

31. Urban, M.; Doubravová, D. Timepix3: Temperature influence on X-ray measurements in counting mode with Si sensor. *Radiat. Meas.* **2021**, *141*, 106535. [CrossRef]

32. Llopart, X.; Ballabriga, R.; Campbell, M.; Tlustos, L.; Wong, W. Timepix, a 65k programmable pixel readout chip for arrival time, energy and/or photon counting measurements. *Nucl. Instrum. Methods Phys. Res. Sect. Accel. Spectrometers Detect. Assoc. Equip.* **2007**, *581*, 485–494. [CrossRef]

33. Poikela, T.; Plosila, J.; Westerlund, T.; Campbell, M.; Gaspari, M.D.; Llopart, X.; Gromov, V.; Kluit, R.; van Beuzekom, M.; Zappon, F.; et al. Timepix3: A 65K channel hybrid pixel readout chip with simultaneous ToA/ToT and sparse readout. *J. Instrum.* **2014**, *9*, C05013. [CrossRef]

34. Mazziotta, M. Electron–hole pair creation energy and Fano factor temperature dependence in silicon. *Nucl. Instrum. Methods Phys. Res. Sect. Accel. Spectrometers Detect. Assoc. Equip.* **2008**, *584*, 436–439. [CrossRef]

35. Urban, M.; Nentvich, O.; Doubravova, D.; Petr, O.; Inneman, A.; Hudec, R.; Sieger, L. Timepix: Influence of temperature and vacuum on equalisation of x-ray detector and its verification. In Proceedings of the International Conference on UV, X-Ray, and Gamma-Ray Space Instrumentation for Astronomy XXI, San Diego, CA, USA, 11–13 August 2019; Volume 11118. [CrossRef]

36. Urban, M.; Doubravova, D.; Nentvich, O. Thermal vacuum testing of Timepix3 detector. *J. Instrum.* **2020**, *15*, C03040. [CrossRef]

37. Liu, Z.; Peters, J.; Kim, J.I.; Das, S.; McCall, K.M.; Wessels, B.W.; He, Y.; Lin, W.; Kanatzidis, M.G. Noise sources and their limitations on the performance of compound semiconductor hard radiation detectors. *Nucl. Instrum. Methods Phys. Res. Sect. Accel. Spectrometers Detect. Assoc. Equip.* **2019**, *916*, 133–140. [CrossRef]
38. Schön, R.; Alfonsi, M.; van Bakel, N.; van Beuzekom, M.; Koffeman, E. Cool Timepix – Electronic noise of the Timepix readout chip down to $-125\,°\mathrm{C}$. *Nucl. Instrum. Methods Phys. Res. Sect. Accel. Spectrometers Detect. Assoc. Equip.* **2015**, *771*, 74–77. [CrossRef]
39. Wilamowski, B.M.; Irwin, J.D. (Eds.) *Fundamentals of Industrial Electronics: The Industrial Electronics Handbook*, 2nd ed.; CRC Press: London, UK, 2011.

Article

Timepix3: Compensation of Thermal Distortion of Energy Measurement

Martin Urban [1,*] , **Ondrej Nentvich** [1] , **Lukas Marek** [2,3], **David Hladik** [1] , **Rene Hudec** [1] and **Ladislav Sieger** [1]

1   Faculty of Electrical Engineering, Czech Technical University in Prague, Technicka 2,
    166 27 Prague 6, Czech Republic
2   Faculty of Mathematics and Physics, Charles University, V Holesovickach 2, 180 00 Prague 8, Czech Republic
3   Advacam, s.r.o., U Pergamenky 1145/12, 170 00 Prague 7, Czech Republic
*   Correspondence: martin-urban@fel.cvut.cz

Abstract: The Timepix3 is a hybrid pixellated radiation detector consisting of a $256\,px \times 256\,px$ radiation-sensitive matrix. Research has shown that it is susceptible to energy spectrum distortion due to temperature variations. This can lead to a relative measurement error of up to 35 % in the tested temperature range of 10 °C to 70 °C. To overcome this issue, this study proposes a complex compensation method to reduce the error to less than 1 %. The compensation method was tested with different radiation sources, focusing on energy peaks up to 100 keV. The results of the study showed that a general model for temperature distortion compensation could be established, where the error in the X-ray fluorescence spectrum of Lead (74.97 keV) was reduced from 22 % to less than 2 % for 60 °C after the correction was applied. The validity of the model was also verified at temperatures below 0 °C, where the relative measurement error for the Tin peak (25.27 keV) was reduced from 11.4 % to 2.1 % at −40 °C. The results of this study demonstrate the effectiveness of the proposed compensation method and models in significantly improving the accuracy of energy measurements. This has implications for various fields of research and industry that require accurate radiation energy measurements and cannot afford to use power for cooling or temperature stabilisation of the detector.

Keywords: Timepix3; X-ray detector; energy measurement; temperature effects; compensations

1. Introduction

Timepix3 (TPX3) is a hybrid single photon counting pixel detector with semiconductor sensors. Due to its hybrid structure, which allows various combinations of thickness and material types of the semiconducting sensor with the same electronics of the readout chip, in dependence on the desired application, it is a handy, popular, and widespread detector in several different scientific and industrial fields [1]. Typical applications of this type of detector include usage in medicine [2,3], art [4], quality control and material properties, as well as neutron detection [5–7] or radiation source localisation and monitoring of the radiation environment [8,9]. Timepix detectors are also frequently used in the scientific domain, such as the ATLAS experiment [10], suborbital rockets [11,12], and applications in space [13], either on board the International Space Station [14,15] or as part of a separate satellite [16–18] or CubeSat mission [19–24] to monitor space weather, solar flares [25,26] or other scientifically significant radiation phenomena.

Furthermore, the novel X-ray and high-energy space experiments focusing on X-rays require suitable focal detectors to record the images provided by the X-ray optics of these devices. Albeit there are several possibilities, the pixel detectors play an important and increasing role because they meet the requirements to be used on miniature satellites such as CubeSats: they are small, lightweight, energy-efficient, and less expensive than other options. However, such an application requires the detector's working temperature range to be broad, −20 °C to 60 °C.

Due to the widespread use of detectors with the TPX3 chip, it can be challenging to maintain all the standard environmental conditions for measurements. Namely, the operating temperature of the detector. The TPX3 with Silicon detection layer has been shown to be highly dependent on the operating temperature [27,28].

In situations where it is not possible or economically realistic to stabilise the operating temperature of the detector, it is necessary to compensate for its influence. This article deals with the possibilities and methodology of how to approach this compensation and the evaluation of the effectiveness of such compensation.

This article is divided into several parts. In Section 2, a brief description of the detector and its principle of operation is given, followed by a description of the measurement methods, including the applied energies of radiation and the issue of the measurement accuracy using the internal temperature sensor, which is essential for further correction. The following section summarises the observed temperature effect and its distortion of energy measurements. Section 4 proposes and presents a comprehensive method for the correction of temperature distortion in the energy spectrum. Section 5 outlines the possibility of generalising the proposed model, including verification on a test sample. Finally, the penultimate Section 6 of the manuscript is devoted to testing over a wide range of temperatures, allowing a more expansive application field and testing the possibility of extrapolating the obtained model. The last section summarises and discusses the presented results and possible future research areas.

2. Material and Methods

As part of this research, several detectors were used and subjected to a series of experiments with radiation sources and different operating temperatures. The following sections provide a description of used instruments and methods.

2.1. Device Description

The Timepix3 is a hybrid pixel radiation detector as the successor to the widely used Timepix detector and the next addition to the Timepix/Medipix family of chips that were developed in the CERN laboratories. Compared to the previous model Timepix [29], TPX3 has better time resolution, adds functionalities, and improves on various electrotechnical specifications.

It is a square-shaped detector with a size of $1.98\,\text{cm}^2$ capable of measuring a broad range of ionising particles. There are (256×256) single pixels and a pitch of $55\,\mu\text{m}$, which makes it $65\,536$ individual pixels in total (see Figure 1). Each pixel is connected to the detector chip by a method called bump-bonding. At the same time, there is a set of integrated electronics for each pixel on the Application-Specific Integrated Circuit (ASIC) chip. It is mainly an analogue amplifier, a threshold discriminator, and an Analogue-to-Digital Converter (ADC). A great advantage of a pixel detector with an integrated Threshold (THL) discriminator is the possibility of using the THL to remove noise and thus operate the detector in near-noise-free mode. Unlike previous versions of Timepix detectors, which were able to read data only in the frame mode, when after the set acquisition time, the signal value is read from all pixels at once, TPX3 is also able to read data in the so-called data-driven mode. This mode does not rely on a uniform frequency and reads the signal from each individual pixel immediately after exceeding the Threshold of the given pixel. The data stream is thus continuous and with a much better time resolution. Since only hit pixels are read out, the total volume of data is significantly lower. The data stream is limited only by the dead time of individual pixels integrated electronics. Thus, its minimal value is, theoretically, $475\,\text{ns}$ for low hit rates and matrix occupancy. When sensor occupancy is equal to or greater than $50\,\%$, the frame driven mode may be a better option than the data-driven mode in terms of readout time [30]. However, the data-driven mode will typically outperform the frame-driven mode for tracking individual particle tracks where no pileups are required. It is worth noting that the energy counter in the data-driven mode is limited to 1022 counts (approximately $500\,\text{keV}$ per pixel), whereas in frame mode the

integral energy counter has a range of up to 16,384 counts, making it more suitable for imaging applications with high photon or particle flux or measurements of highly ionising particles. The minimum threshold limit depends on the type and thickness of the used detection layer material and the internal noise of the ASIC chip. Typical detection layers can be Silicon (Si), Cadmium Telluride (CdTe), or Gallium Arsenide (GaAs) in various thicknesses [31,32]. For the Si detection layer, which was used in the presented work, the minimum threshold value is as low as 2 keV [33].
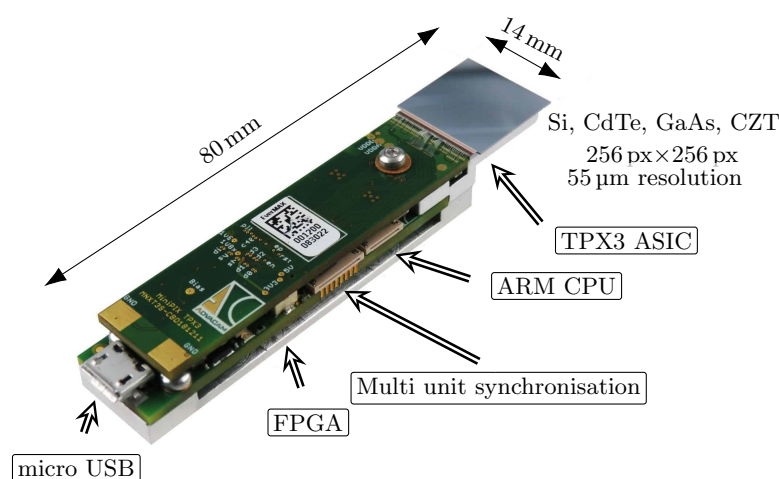
Figure 1. Illustration and description of the MiniPIX Timepix3 detector without a protective case.

There are various measurement modes that suit different applications, allowing users to obtain information about various parameters of particles.

The Event Counting (EC) mode is a simple counting method that records the number of particles that hits a particular pixel. In this mode, the digital output of each pixel is monitored, and the count of rising edges (above the threshold) is recorded. This mode provides basic information about the particle flux and can be used for radiation mapping and dose rate monitoring.

The Time-of-Arrival (ToA) mode is a measurement mode that records the exact arrival time of incoming particles to each pixel. In this mode, the detector uses a time-stamping mechanism to record the time the particle crosses the threshold voltage level. ToA is a time indication of how much time has passed between the start of the measurement and the impact of the particle.

The Time-over-Threshold (ToT) mode involves the measurement of the duration of a signal generated by a particle exceeding a specified threshold voltage level. This mode implements an indirect energy measurement method based on the Wilkinson-type ADC, where the analogue signal from each pixel is continuously monitored. Whenever the signal exceeds the threshold voltage, a timer is triggered to start counting. The timer stops when the signal, which is being discharged through a constant current, falls below the threshold voltage. After calibration, the recorded time is proportional to the energy deposited by the particle in the pixel.

The Timepix3 detector can operate in one of three measurement modes (ToA, ToA & ToT, and EC & integralToT) [30], which combine above-mentioned principles and allow simultaneous measurement of some of the parameters. The frame-based readout mode allows measurement in the combination mode EC & integralToT, ToA & ToT and only ToA. This is different from the data-driven mode, which allows measurement in ToA & ToT, only ToA and only ToT.

The instruments used in this work were equipped with a readout interface called MiniPIX (see Figure 1). It is characterised by compact size, low power consumption, micro-USB connection, and the synchronisation of several units if required, and is equipped with

Field Programmable Gate Array (FPGA) for fast data processing and detector handling. A set of five identical TPX3 detectors equipped with a 500 μm silicon sensor and a MiniPIX interface was created and will be further investigated in this paper.

2.2. Methods Descriptions

Two types of radiation sources were used to obtain data for radiation energy measurements. Radiation sources of the first type use the effect of X-ray fluorescence (XRF) to generate characteristic radiation. The XRF generates precise energy lines corresponding to the target material. The lines depend on the electron orbitals that are characteristic of atoms of a given element used as the target. The materials of the targets with corresponding emission lines used in this manuscript are listed in the first five rows of Table 1.

Due to the possibility of polychromatic background radiation from scattered radiation in a radiation-shielded box, the overall measured energy spectrum is complex. In addition to the mentioned specific energy lines, the spectrum includes X-rays produced by the X-ray fluorescence of the materials in the shielding box, mainly Lead, as well as photons that have undergone additional scattering either in the sensor or in the X-ray box itself, detected as Compton events. The measured spectrum also includes a continuous spectrum produced by the X-ray tube.

Two radionuclides Barium and Europium were used as a second type of radiation source. Their use provides sufficiently dense coverage of the energy spectrum up to 100 keV, which was chosen as the maximum reasonable value taking into account the detection efficiency of the sensors used. It should be noted that the detection efficiency of a 500 μm silicon sensor decreases sharply with increasing energy. It reaches about 50 % at 20 keV, but is only 10 % at 30 keV and continues to decrease with increasing incident energy. For this reason, the measurement time was extended with respect to the measurement energy of the peak under investigation and the efficiency of the sensor material. The radionuclide energy values that have been taken into account are listed in the last two rows of the table of sources used (Table 1).

Table 1. List of radiation sources and target materials with their characteristic energies.

Symbol	Element/Radiation Source	Energy
Cu	Copper	8.046 keV
Mo	Molybdenum	17.480 keV
In	Indium	24.209 keV
Ta	Tantalum	57.532 keV
Pb	Lead	74.969 keV
^{152}Eu	Europium	39.910 keV
^{133}Ba	Barium	30.973 keV 80.998 keV

Each of these methods requires a different measurement arrangement. Therefore, two setups were prepared. To measure the energies generated by XRF, it was necessary to use an X-ray tube and a different geometrical arrangement compared to the application with radionuclides. Both setups use a holder for samples, and the whole arrangement was placed inside a radiation-shielded box. The schematic layouts are shown in Figure 2.

All detectors were placed and thermally coupled to a Peltier plate for their thermal stabilisation at each measurement phase. The energy measurements (ToT & ToA measurement in data-driven mode) of the individual samples were performed in temperature steps of 10 °C over a temperature range of 10 °C to 70 °C. Sufficient time for thermal stabilisation of the measurement setup was kept before each measurement started.
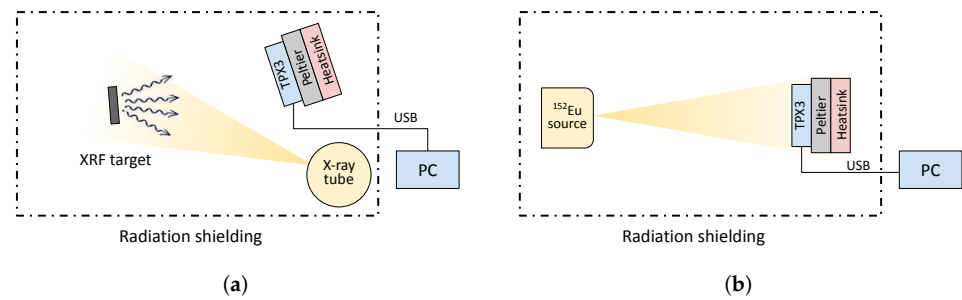
Figure 2. Schematic arrangement for measuring the energy spectrum of radiation. (**a**) X-ray fluorescence; (**b**) Radionuclides.

The evaluation methodology is based on the procedure presented in [28], where a combination of Gaussian $G_a(x)$ and complementary error function $E_{rfc}(x)$ is used (Equation (1)).

$$G_e(E, A_1, A_2, \mu, \sigma) = G_a(E, A_1, \mu, \sigma) + A_2 \cdot E_{rfc}\left(\frac{E - \mu}{\sigma\sqrt{2}}\right) \tag{1}$$

The function $G_a(E, A_1, \mu, \sigma)$ stands for the Gaussian

$$G_a(E, A_1, \mu, \sigma) = A_1 \cdot e^{\frac{-(E-\mu)^2}{2\sigma^2}} \tag{2}$$

and complementary error function is defined as

$$E_{rfc}(x) = 1 - \frac{2}{\sqrt{\pi}} \int_0^x e^{-t^2} dt. \tag{3}$$

The following notation is used for the energy (E), the intensity of the error function (A_2) or intensity of the spectral peak (A_1) and its mean energy (μ) as well as the energy noise (σ). Figure 3 shows an example of the evaluation procedure where function (Equation (1)) (green line) is applied over the range of measured data (blue markers) to provide an initial estimation of the input parameters for the accurate determination of the measured energy peak parameter.

The obtained values can then be used to automatically determine a suitable evaluation range and input parameters to accurately fit the Gaussian function (Equation (2)) of the energy peak near its maximum intensity, see orange line in Figure 3.

Goodness of fit and its quality are assessed using Pearson's chi-square (χ^2) test (Equation (4)), respectively, reduced chi-square (χ_ν^2) statistic (Equation (5)). It is possible to fine-tune the position of the mean (μ_{χ^2}) of the examined energy peak according to the distribution of $\chi^2(\mu)$, particularly the position of its minimum, under the conditions of the fit acceptability $\chi_\nu^2 \approx 1$.

$$\chi^2 = \sum_i \frac{(M_i - F_i)^2}{\sigma_i^2} \tag{4}$$

$$\chi_\nu^2 = \frac{\chi^2}{\nu} \tag{5}$$

The variable i defines the evaluation interval, which in this case corresponds to the range of the Gaussian fit, M_i represents the number of measured counts in the i-th energy bin, F_i is the value of the expected flux based on the estimated Gaussian fit, and σ_i^2 represents the variance of the individual counts. The χ_ν^2 is defined as the proportion of χ^2 and the degrees of freedom (ν), where $\nu = |i| - 3$ with $|i|$ as the cardinality of the evaluated interval i.

According to the procedure described, the position of the energy peak (see purple dashed-dotted line in Figure 3) at 57.072 keV can be determined with an uncertainty of 10 eV

from the given data of the Ta-$K_{\alpha 1}$ line measurement, and the Full Width at Half Maximum (FWHM) is determined to 4.51 keV.

The variation of these parameters, in particular, the drift of the peak mean (absolute measurement accuracy, relative error of measurement) and its width (relative energy resolution), are further compared and evaluated. The reference values for absolute measurement accuracy and relative error of measurement are obtained from measurements at 20 °C, the temperature at which the manufacturer calibrates the detectors.
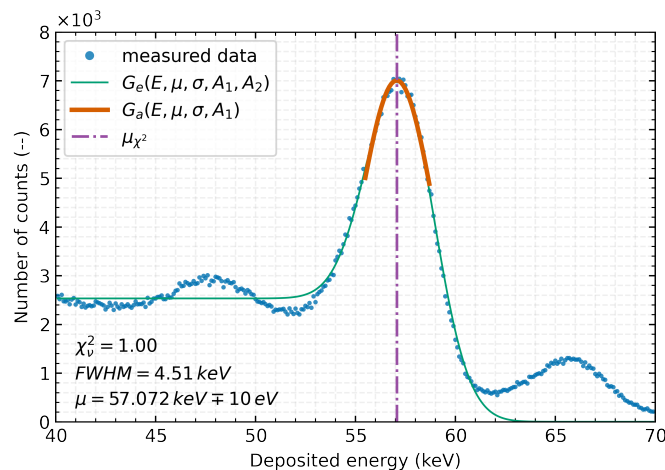

Figure 3. Part of the measured energy spectrum of the radiation produced by the X-ray fluorescence of a Tantalum target with a 500 µm Si Timepix3 detector without temperature stabilisation. Measured data (blue markers) together with the $G_e(E, A_1, A_2, \mu, \sigma)$ function (combination of Gaussian and complementary error function—green line) and with the result of the final fit of the $G_a(E, A_1, \mu, \sigma)$ function (orange line) to the Ta-$K_{\alpha 1}$ line. The resulting position of the μ_{χ^2} of the evaluated peaks determined by χ^2 minimisation is 57.072 keV (purple dashed dotted line). Considering the statistically significant number of observed events, the maximum size of statistical uncertainties was determined to be <80 counts in the range shown, the individual error bars are not plotted to the measured points for clarity.

2.3. Internal Temperature Sensor

The stability of the measured energy spectrum is crucial and is achieved by maintaining a constant or known temperature. The internal thermometer on the chip should provide sufficient thermal accuracy, and the calibration of this thermometer is necessary for the proper energy shift compensation. This chapter discusses the verification of the linearity of the internal thermometer using an external reference PT1000 thermometer. The several selected temperatures in the range of 10 °C to 70 °C were chosen to be relevant to the operational temperature range of the TPX3 detector.

Timepix3 detector has two places on-board to measure temperature. The first and most crucial is in the TPX3 ASIC chip, and the second is an internal thermometer of the processing microcontroller. Both integrated circuits were thermally coupled to the Peltier plate and stabilised on the desired temperature in the range from 10 °C to 70 °C and controlled by an external device until the measured temperature was stable on all three thermometers. It takes about 10 min to stabilise the plate at each point.

During the thermal cycling process for spectral characterisation, temperature data was collected from all detectors. The results of the investigation indicated that all thermometers exhibited a linear progression in their readings, with a slight offset compared to the preset temperature. Therefore, the relative error of temperature measurement was noted to be between 1 % and 40 % depending on the specific device and the measured temperature.

A linear regression calculation was performed for the ASIC chip, resulting in the regression between 0.94 and 1.02 for all five measured detectors, as stated in the row slope

in Table 2, which follows the preset temperature linearly but with a constant offset. The constant offset was estimated to range from −6.06 °C to 0.8 °C and the coefficient of determination R-squared (R^2) was found to be nearly 1 for all measured detectors, which indicates that linear regression is a suitable fit for the internal thermometer.

Table 2. Measured linearity, offset and coefficient of determination (R^2) of the temperature dependence of five Timepix3 detectors on preset temperature by an external device.

	Chip A	**Chip B**	**Chip C**	**Chip D**	**Chip E**
Slope	1.01	1.00	0.94	0.99	1.02
Offset	−4.13	−0.76	0.80	−3.10	−6.06
R^2	0.999 9	0.999 9	0.999 7	1.000 0	0.999 7

In case the estimated value of slope differs from 1 in the linear regression, the deviation from the set and measured temperature will vary if not corrected. Based on the coefficients listed in Table 2, it is possible to determine the correction function for the internal thermometers. Given the linear dependence, it is sufficient to measure the temperature at two points, such as room temperature and 50 °C for example, to determine the linear function. This step is crucial in obtaining accurate information about the detector temperature during measurement because, as shown further in the article, the detector's thermal variation significantly affects the resulting energy spectrum and information about its value is critical for the correction.

3. Temperature Effects

Based on the measured and processed data from all examined detectors, radiation sources, and temperature stages, the temperature dependence of the Timepix3 detectors [28] was verified. The results in Figure 4 represent the significant temperature dependence of the radiation energy measurements in the Time-over-Threshold mode of the detectors.
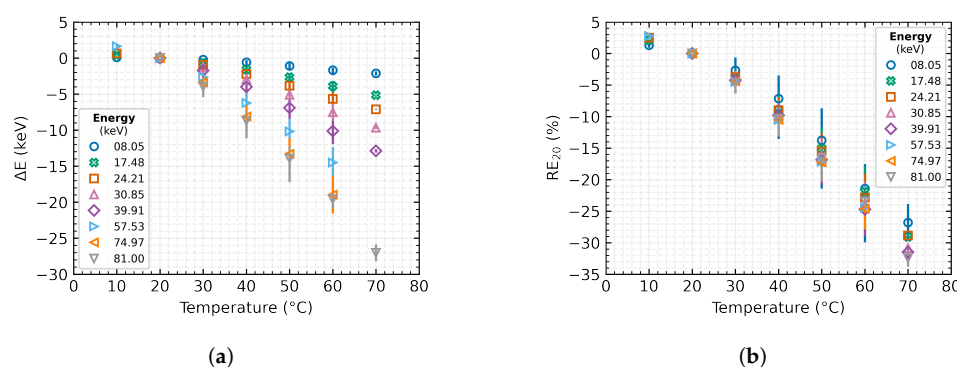
Figure 4. Influence of temperature change of the MiniPIX Timepix3 detectors equipped with 500 µm Si sensor on the obtained energetic spectrum measured by Time-over-Threshold in data-driven mode. The plotted data represent the mean values over the tested detectors, and the error bars indicate their minimum and maximum value: (**a**) Absolute measurement accuracy; (**b**) Relative error of measurement.

The results show that the energy spectrum drifts with the temperature changes. With increasing temperature, the energy spectrum nonlinearly shifts towards lower energies, this offset is more significant with increasing incident energy. Already with a 10 °C change of the detector temperature, a relative measurement error of about 4 % occurs. A further change in temperature from the reference point at 20 °C, e.g., due to the influence of the environment or the detector self-heating, may cause a displacement of the energy spectrum of up to tens of kiloelectronvolts. This drift causes an error of more than 30 %, in the case of heating the detector to 70 °C.

Table 3 shows the resulting values for selected radiation sources and detector temperatures from the tested interval.

Table 3. Temperature influence on radiation energy measurement with 500 µm silicon MiniPIX Timepix3 detectors in Time-over-Threshold mode. Where ΔE is the absolute measurement accuracy, RE is the relative error of measurement, and Res. is the relative energy resolution.

Energy	17.48 keV			24.21 keV			57.53 keV		
Param.	ΔE (keV)	RE (%)	Res. (%)	ΔE (keV)	RE (%)	Res. (%)	ΔE (keV)	RE (%)	Res. (%)
10 °C	0.37	2.11	16.88	0.62	2.52	13.24	1.64	2.79	8.70
30 °C	−0.68	−3.83	17.02	−0.92	−3.73	12.72	−2.67	−4.50	6.48
60 °C	−3.89	−21.95	18.66	−5.66	−22.87	15.20	−14.51	−24.49	8.85

4. Compensation Method

As was written in the recently published paper, a simplified linear compensation [28] can be used for the initial compensation of the detector's temperature drift. This compensation method is effective for the constant temperature difference of the detector during measurement from the calibration temperature. The linear compensation method indeed finds its use; however, if the detector is permanently exposed to different but constant conditions, performing a complete recalibration of the device under these conditions is preferable. Nevertheless, if the condition varies frequently, this approach is not appropriate. A new method of complex temperature compensation is proposed, which is based on the analysis of the collected data, the results, and the observed dependencies. This method utilises a temperature distortion model applicable to a continual change not only of the detector temperature but also of the incident radiation energy.

The examination of the measured data and subsequent processing (Figure 4) suggests a definable temperature dependence of the energy spectrum drift. Further processing allows us to describe the dependence of the measured energy on temperature (Figure 5a) and thus to establish Equation (6).

$$E_{meas} = mT^2 + nT + o \tag{6}$$

where E_{meas} is measured energy by the detector, T is detector temperature during measurement and m, n, o are function parameters.

However, the parameters of this dependency are highly variable concerning the energy of the incident radiation. Therefore, it was necessary to define the interdependence of this function on the radiation energy. Gradually, it became apparent that the individual parameters of the Equation (6) have a linear dependence with regard to the radiation energy (Figure 5b) and, therefore, can be described by linear regression, see Equation (7).

$$x = x_1 E + x_2 \tag{7}$$

where x represents one of the parameters m, n, o in Equation (6), E is the energy of radiation, and x_1, x_2 are parameters of the dependence.

The mutual substitution of these two functions yields a model of the temperature distortion of the measurement accuracy of the energy spectrum with the TPX3 detector. The expression E leads to a function (Equation (8)) that contains the constants m, n, and o obtained from the model and the two variables E_{meas} as the measured energy and T as the temperature of the measurement.

$$E = \frac{E_{meas} - m_2 T^2 - n_2 T - o_2}{m_1 T^2 + n_1 T + o_1} \tag{8}$$
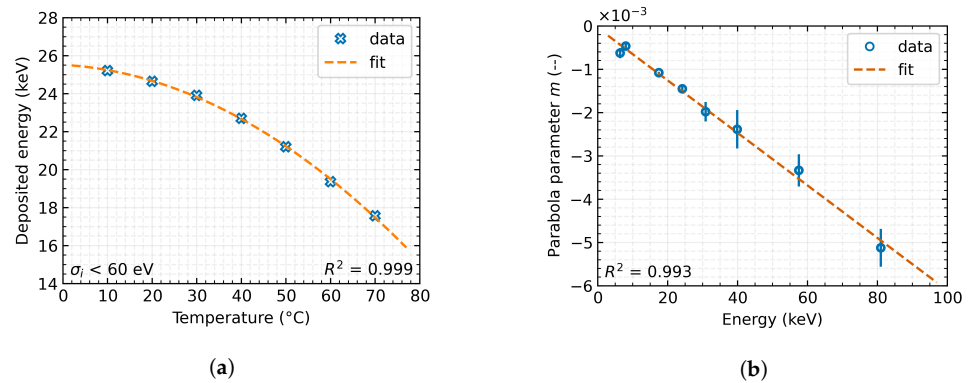
(a)

(b)

Figure 5. Model of temperature dependence distortion of measurement accuracy of radiation energy spectrum (Time-over-Threshold in Data-driven mode) with Timepix3 detector equipped with 500 μm Si sensor. The error bars indicate the inaccuracy of a given parameter obtained by the fitting function: (**a**) Temperature dependence; (**b**) Energy dependence.

Its application to the measured data yields the real energy of the incident radiation after correction for temperature distortion.

The evolution of absolute measurement accuracy and relative measurement error over the complete, tested range after applying the presented correction method is shown in Figure 6. The results are compiled over all tested detectors. A simple comparison with Figure 4 demonstrates the significant minimisation of the temperature dependence, the compensation of the thermal drift in the energy spectrum of the radiation, and the improvement of the obtained results. The plot shows that the absolute shift of the measured energy has been reduced by applying the correction from almost -30 keV to ± 0.5 keV over the entire tested energy and temperature range. The relative error of the measurements has thus also dropped from the original -30% (at 70 °C) to 1.5% thus staying within the $\pm 1.5\%$ tolerance interval over the whole range. For a more accurate representation, Table 4 gives specific values for the same selected radiation source types and detector temperatures as in Table 3.
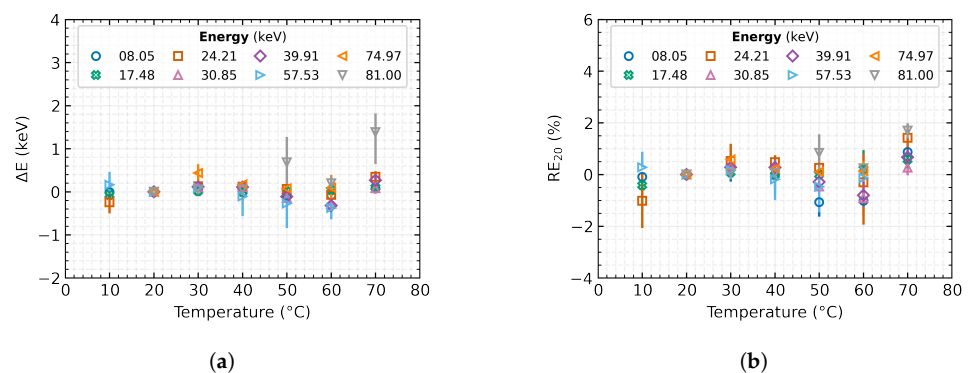

(a)

(b)

Figure 6. The change in absolute measurement accuracy and relative measurement error of the tested sources after applying the proposed correction. The plotted data represent the mean values over the tested detectors, and the error bars indicate their minimum and maximum value: (**a**) Absolute measurement accuracy; (**b**) Relative error of measurement.

Table 4. Temperature influence on radiation energy measurement with 500 µm silicon MiniPIX Timepix3 detectors in Time-over-Threshold mode after application of the proposed individual correction method. Where ΔE is the absolute measurement accuracy, RE is the relative error of measurement, and Res. is the relative energy resolution.

Energy	17.48 keV			24.21 keV			57.53 keV		
Param.	**ΔE (keV)**	**RE (%)**	**Res. (%)**	**ΔE (keV)**	**RE (%)**	**Res. (%)**	**ΔE (keV)**	**RE (%)**	**Res. (%)**
10 °C	−0.07	−0.42	14.99	−0.25	−1.02	14.01	−0.20	−0.35	8.67
10 °C	0.01	0.08	16.21	0.13	0.52	11.64	0.07	0.13	6.67
60 °C	0.04	0.21	22.56	−0.07	−0.31	18.80	−0.56	−0.97	12.52

5. Generalisation

As part of the potential expansion of the presented compensation method for a wide range of applications without the necessity to characterise individual detectors, the possibility of parameter generalisation was also tested. Based on the tested detectors' data, an average temperature dependence model was established and the necessary general parameters for the compensation were determined (see Table 5). One detector was removed from the modelling set for generalisation and has been used for final verification and applicability comparison.

Table 5. Generalised parameters to compensate for temperature distortion in energy spectrum measurement accuracy using Timepix3 detectors with 500 µm Silicon sensor.

Parameter	X_1	X_2
m	$-5.664\,27 \times 10^{-5}$	$-1.271\,01 \times 10^{-4}$
n	$-1.660\,14 \times 10^{-3}$	$2.767\,56 \times 10^{-2}$
o	$0.109\,11 \times 10^1$	$-0.100\,19 \times 10^1$

The characteristic X-ray fluorescence of the Lead target (energy 74.97 keV) was measured several times with detector *E* outside the modelling set at detector temperatures of 30 °C, 40 °C and 50 °C. The resulting measured spectrum after normalisation for comparison is shown in Figure 7a. As can be seen, the temperature effect significantly distorts the accuracy of the energy measurement by 19%.

Applying the above-proposed compensation method with the parameters obtained from the previous characterisation of the detector *E*, the energy spectrum shown in Figure 7b can be produced. It can be seen from the figure that the effect of temperature distortion on the absolute accuracy of the measurement was nearly minimised to the relative error of measurement of less than 0.7%. At the same time, there is a clear trend of increasing energy peak width, common to all measurements and methods, thus deteriorating the detector's energy resolution for high temperatures. This is due to the increasing thermal noise in the device.

Suppose the generalised parameters listed in Table 5 are used in the same correction method instead of using the individual parameters for a given detector. In that case, the spectra shown in Figure 7c are obtained. It should be noted that a more statistically significant number of detectors would need to be tested and characterised to produce a robust, generally valid, generalised model.

It is noticeable that the generalised compensation does not provide as satisfactory results as in the prior case. This result was expected because when using generalised parameters for the compensation model, there are always compromises regarding the specific parameters of the detectors included in the training set. Therefore, after applying the generalised parameters, the output cannot be as accurate as in the case of compensation parameters determined for a specific detector. Nevertheless, it is shown that the proposed compensation method can be successfully applied to correct the energy drift even with

generalised parameters based on several other detectors. The resulting relative error of the measurements does not exceed 1.5%, for the particular detector types. The detailed comparison of the fundamental parameters for several detector temperatures is given in Table 6 for the cases: raw measured, compensation based on parameters for specific detector and after compensation of thermal distortion based on generalised parameters.
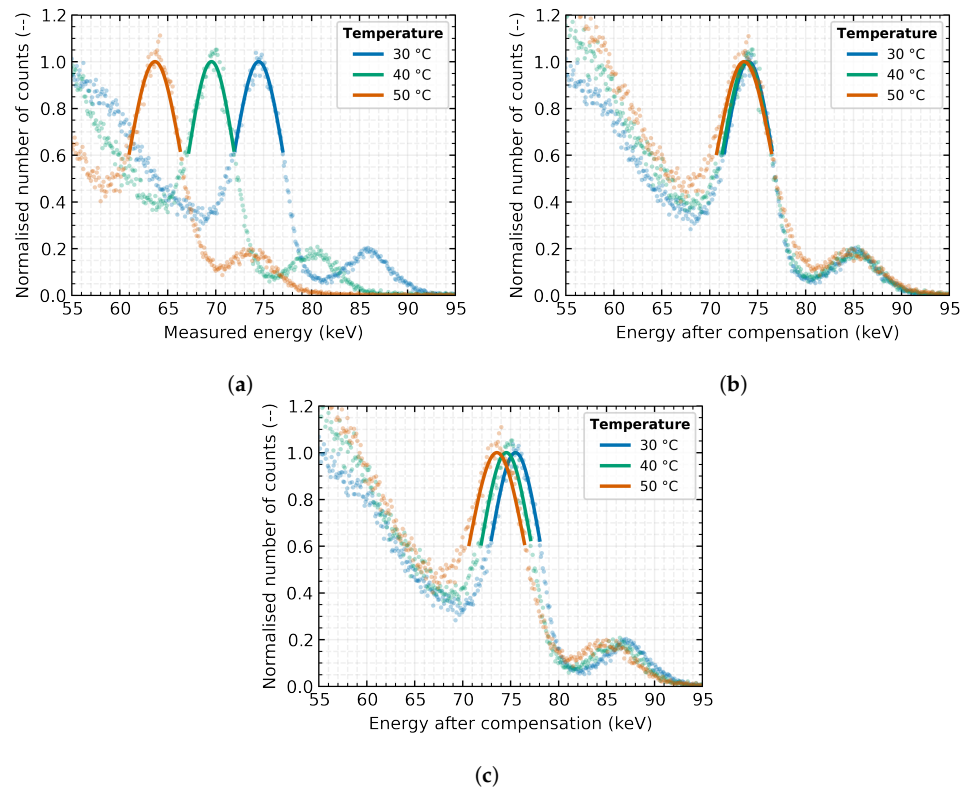

(**a**)   (**b**)

(**c**)

Figure 7. The comparison of the energy spectrum obtained by X-ray fluorescence with a Lead target and different compensation for thermal distortion. The measurements were performed with the detector *E* at three different sensor temperatures (30 °C, 40 °C and 50 °C): (**a**) Without compensation; (**b**) Individual compensation model; (**c**) Generalised compensation model.

Table 6. Comparison of the energy spectrum parameters obtained by X-ray fluorescence with a Lead target and different compensation for thermal distortion. Measurements were performed with detector *E* (which is outside the modelling set) at three different sensor temperatures (30 °C, 40 °C and 50 °C). Symbol ΔE represents the absolute measurement accuracy, RE is the relative error of measurement, and Res. is the relative energy resolution.

	Measured			Individual			Generalised		
Param.	ΔE (keV)	RE (%)	Res. (%)	ΔE (keV)	RE (%)	Res. (%)	ΔE (keV)	RE (%)	Res. (%)
30 °C	−3.45	−4.38	5.93	−0.41	−0.55	6.61	1.10	1.46	6.73
40 °C	−8.49	−10.79	6.06	−0.43	−0.57	6.78	0.27	0.37	6.87
50 °C	−14.87	−18.89	8.20	−0.52	−0.70	8.18	−0.56	−0.74	8.30

6. Validation and Extrapolation over a Wide Temperature Range

The validation of a model over a wide temperature range is a particularly important process that can significantly increase the applicability and versatility of a given model in engineering and scientific applications, such as aerospace, automotive, or outdoor environmental research. This reduces the risk of failure in safety-critical or mission-critical applications.

The extrapolation of measured data to temperatures below 0 °C can effectively reduce the need for complex and costly measurements in extreme temperature conditions, while still providing valuable insight into system behaviour. This approach can lead to more efficient and cost-effective product or system development/application without the need for a number of physical tests and additional calibrations. The utility of such extrapolation has been demonstrated in this paper, where the model has been validated over a temperature range including temperatures down to −40 °C.

A detector MiniPIX TPX3 with a 1 000 µm thick Silicon sensor, beyond the previously tested collection, was used to verify the proposed model and the extrapolation. It was operated at temperatures between −40 °C to 60 °C, requiring careful control of the test environment to prevent condensation and frosting on the detector because temperatures were deep below the dew point. Consequently, the device under test could have been short-circuited and irreversibly damaged. To mitigate this risk, the detector was placed in a vacuum chamber and thermally coupled and stabilised using a three-stage Peltier element (Figure 8). Waste heat was dissipated through a water cooling system outside the vacuum chamber. The temperature was stabilised for at least 10 min before each measurement and controlled with a feedback thermometer placed below the Timepix3 chip. An automatic carousel with multiple targets for generating XRF radiation at various energies was also placed inside the chamber.
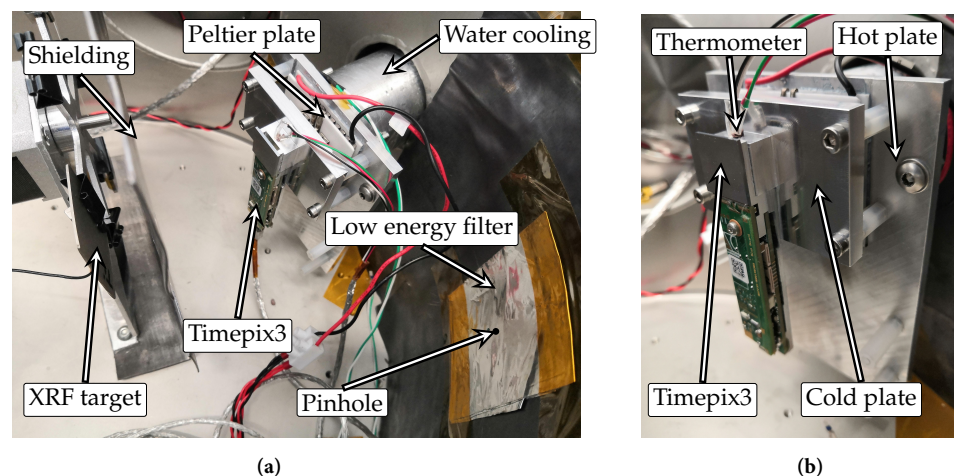

(a) (b)

Figure 8. Timepix3 detector arrangement for thermal testing of verification and extrapolation of the compensation model in the vacuum chamber: (**a**) arrangement configuration for X-ray fluorescence measurement; (**b**) details of the detector placement on the Peltier module with feedback thermometer.

Due to limitations in the vacuum system and safety measures, it was possible to generate characteristic fluorescence radiation with energies up to 30 keV. Considering these restrictions and with respect to the material and thickness of the detection layer, the following XRF targets were selected: Zircon (Zr) at 15.77 keV, Cadmium (Cd) at 23.11 keV and Tin (Sn) at 25.27 keV. Additional to the X-ray fluorescence targets, an Americium (^{241}Am) radionuclide with a spectral line at 59.54 keV has been selected for optimal results.

From Figure 9, it is clear that the described and presented model for compensating temperature distortion of the measured energy spectrum of the incident radiation and, thereby, the increasing error of energy measurement is not only effective for temperatures above 0 °C but has also been validated at temperatures below freezing point. The results of experiments verified that the superimposed parabolic model effectively reduces the relative measurement error at −40 °C from −11% to approximately 0.5% (for XRF energy of Sn; 25.27 keV) as can be clearly seen in the comparison of Figure 10a,b.
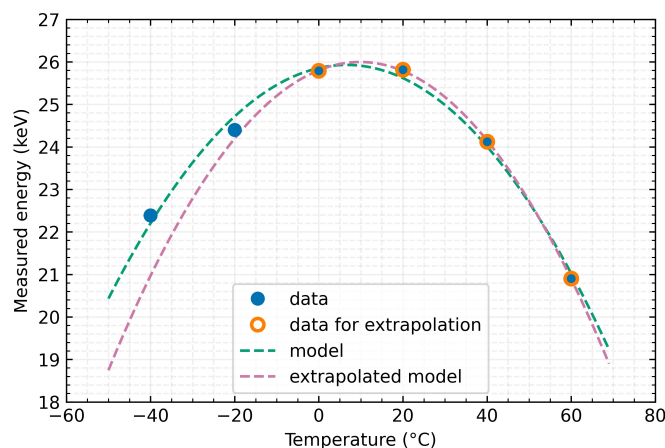
Figure 9. Model of temperature compensation of energy measurement (X-ray fluorescence with Tin target and detector in Time-over-Threshold mode of measurement and data-driven readout mode) distortion using Timepix3 detector with 1 000 µm Silicon sensor in the temperature range from −40 °C to 60 °C. Extrapolated model based on data measured in temperatures above 0 °C is shown as well.

Figure 10. The comparison of the energy spectrum obtained by X-ray fluorescence with a Tin target and different compensation for thermal distortion. The measurement results of a detector with a 1 000 µm Si sensor placed in a vacuum for different sensor temperatures (−40 °C, 0 °C and 60 °C) are shown: (**a**) Without compensation; (**b**) Individual compensation model; (**c**) Extrapolated compensation model.

The extrapolation of the above-mentioned model was tested with the same detector. A temperature compensation model was developed based on the data points that were above the freezing point (depicted as orange in Figure 9). Figure 10 reveals that as the tem-

perature decreased and moved away from the reference points, the extrapolated model showed an increased discrepancy from the model constructed using the entire dataset. However, even this extrapolated model provides a considerable improvement in the relative accuracy of the measurement for temperatures below 0 °C (as seen in Figure 10c). At a temperature of −40 °C, it reduces the error from the original by more than −11% to approximately 2% (as shown in Table 7). This compensation may be sufficient for some applications, and extrapolation would simplify and speed up the compression process when it is not necessary or practical to create suitable cooling conditions and it is difficult to undercool the detector for parameterisation.
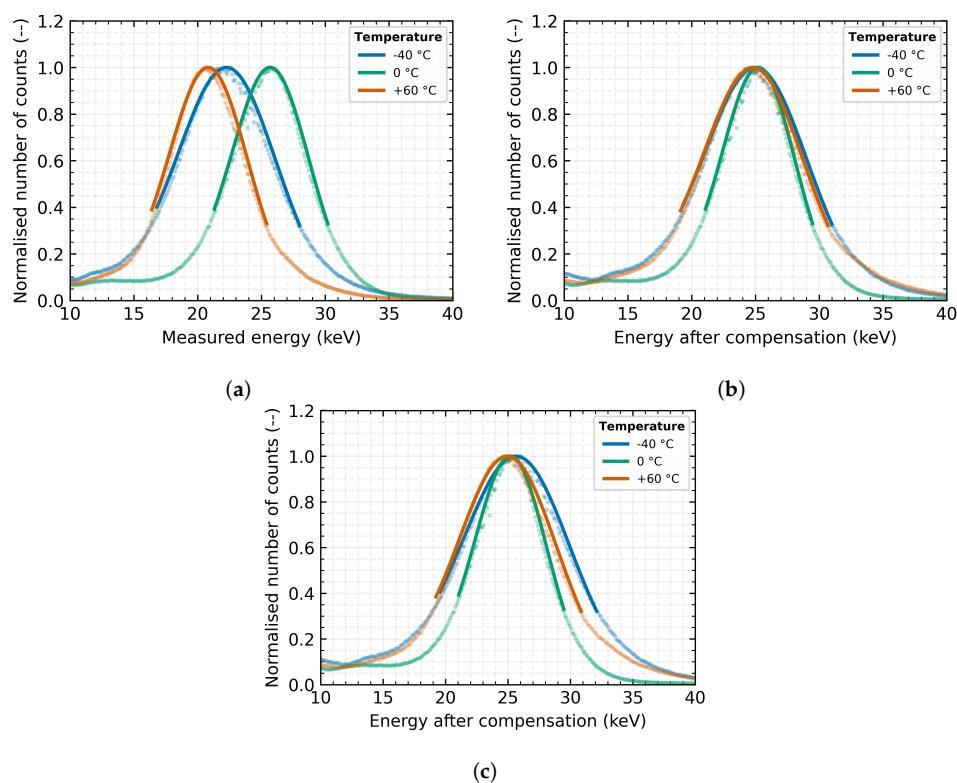
Table 7. Comparison of the energy spectrum parameters obtained by X-ray fluorescence with a Tin target and different compensation for thermal distortion. The measurement results of a detector with a 1 000 µm Silicon sensor placed in a vacuum for different sensor temperatures (−40 °C, 0 °C and 60 °C) are listed. Where ΔE is the absolute measurement accuracy, RE is the relative error of measurement, and Res. is the relative energy resolution.

Param.	Measured			Individual			Extrapolated		
	ΔE (keV)	RE (%)	Res. (%)	ΔE (keV)	RE (%)	Res. (%)	ΔE (keV)	RE (%)	Res. (%)
−40 °C	−2.88	−11.41	35.17	−0.13	−0.5	36.95	0.54	2.13	39.43
0 °C	0.31	2.03	27.95	0.04	0.14	26.38	0.02	0.09	26.48
60 °C	−4.36	17.27	28.29	−0.35	−1.39	36.09	−0.21	−0.84	36.26

7. Conclusions

This paper presents a solution to the problem of energy spectrum distortion due to temperature fluctuations in the Timepix3 detector with MiniPIX readout interface and Silicon sensor with a thickness of 500 µm and 1 000 µm. The study's results demonstrate that a relative measurement error of up to 35 % can occur in the tested temperature range from 10 °C to 70 °C. The study was carried out using different radiation sources (X-ray fluorescence and natural sources) in the field of up to 100 keV to investigate the detector's behaviour.

The first part of the paper also emphasises the issues of the potential usage of an internal thermometer built into the ASIC chip, which would significantly impact the measurement and compensation capabilities.

The authors propose a complex compensation method, which has been demonstrated to minimise the measurement error to no more than 1.5 % for all energies over the entire temperature range tested. The results show that the proposed compensation method and models significantly improve the accuracy of energy measurements in Time-over-Threshold mode.

The possibility of creating a general model for temperature distortion compensation was also discussed. It would require testing a statistically significant number of detectors. Nevertheless, the results of the study indicate that even when applied to a small set of five, detectors, the possibility of generalisation appears to be realistic. After applying the generalised model to a detector not included in the learning set, the relative error of energy measurement in the X-ray fluorescence spectrum of Lead (74.97 keV) was found to be reduced from the original 15 % to less than 1.5 % at a detector temperature of 50 °C.

The compensation method was further tested in temperatures up to −40 °C using a vacuum chamber and was also found to be valid in this range. The extrapolated model, based on measurements where the temperature did not drop below 0 °C, was verified for the correction of energy spectra measured when the detector temperature was below 0 °C. It was found that although the efficiency of the compensation of the measurement error of the incident energy is degraded, the extrapolated model can be used. During the tests with XRF of the Tin target (25.27 keV) and using at a detector temperature of −40 °C, the relative measurement error was reduced from the original 11.4% to 2.1% with extrapolated model (0.5 % in the case of the individual model based on all data points).

The presented results, methods, and models allow the use of the TPX3 detector to be extended to a wide range of applications where cooling or temperature stabilisation of the detector is not possible or economically viable. The compensation method provides a valuable solution to a common problem in space radiation measurement and has the potential to have a significant impact on various applications.

In conclusion, the authors have successfully demonstrated a solution to the problem of energy spectrum distortion due to temperature fluctuations in the Timepix3 detector with MiniPIX readout interface and Si sensor with a thickness of 500 μm and 1 000 μm. The proposed compensation method has been shown to significantly improve the accuracy of energy measurements, and the model's validity has been verified in both parts of the temperature range, below and above 0 °C. The findings of the study have the potential to impact a wide range of applications and industries, increase the application potential of this detector type in other fields and decrease workforce demands (series of calibrations) and power sources (thermal stabilisation/cooling).

References

1. Al Darwish, R.; Marcu, L.; Bezak, E. Overview of current applications of the Timepix detector in spectroscopy, radiation and medical physics. *Appl. Spectrosc. Rev.* **2020**, *55*, 243–261. [CrossRef]
2. Ávila, C.A.; Mendoza, L.M.; Roque, G.A.; Loaiza, L.; Racedo, J.; Rueda, R. Feasibility study of a TIMEPIX detector for mammography applications. In *Proceedings of the 13th International Conference on Medical Information Processing and Analysis*; Romero, E., Lepore, N., Brieva, J., García, J.D., Eds.; International Society for Optics and Photonics, SPIE: Bellingham, WA, USA, 2017; Volume 10572, p. 105720Z. [CrossRef]
3. Procz, S.; Avila, C.; Fey, J.; Roque, G.; Schuetz, M.; Hamann, E. X-ray and gamma imaging with Medipix and Timepix detectors in medical research. *Radiat. Meas.* **2019**, *127*, 106104. [CrossRef]
4. Zemlicka, J.; Jakubek, J.; Kroupa, M.; Hradil, D.; Hradilova, J.; Mislerova, H. Analysis of painted arts by energy sensitive radiographic techniques with the Pixel Detector Timepix. *J. Instrum.* **2011**, *6*, C01066. [CrossRef]

5. Rubovič, P.; Ekendahl, D.; Vykydal, Z.; Hůlka, J.; Bergmann, B.; Pospíšil, S.; Štekl, I. Dosimetry in mixed neutron-gamma fields with a Timepix detector. *Radiat. Meas.* **2018**, *119*, 22–26. [CrossRef]

6. Rubovič, P.; Bonasera, A.; Burian, P.; Cao, Z.; Fu, C.; Kong, D.; Lan, H.; Lou, Y.; Luo, W.; Lv, C.; et al. Measurements of D–D fusion neutrons generated in nanowire array laser plasma using Timepix3 detector. *Nucl. Instrum. Methods Phys. Res. Sect. A Accel. Spectrometers Detect. Assoc. Equip.* **2021**, *985*, 164680. [CrossRef]

7. Granja, C.; Uhlar, R.; Chuprakov, I.; Alexa, P.; Sansarbayar, E.; Gledenov, Y.; Poklop, D.; Olsansky, V.; Marek, L.; Vuolo, M.; et al. Detection of fast neutrons with the pixel detector Timepix3. *J. Instrum.* **2023**, *18*, P01003. [CrossRef]

8. Stibinger, P.; Baca, T.; Saska, M. Localization of Ionizing Radiation Sources by Cooperating Micro Aerial Vehicles with Pixel Detectors in Real-Time. *IEEE Robot. Autom. Lett.* **2020**, *5*, 3634–3641. [CrossRef]

9. Baca, T.; Stibinger, P.; Doubravova, D.; Turecek, D.; Solc, J.; Rusnak, J.; Saska, M.; Jakubek, J. Gamma Radiation Source Localization for Micro Aerial Vehicles with a Miniature Single-Detector Compton Event Camera. In Proceedings of the 2021 International Conference on Unmanned Aircraft Systems (ICUAS), Athens, Greece, 15–18 June 2021; pp. 338–346. [CrossRef]

10. Bergmann, B.; Billoud, T.; Leroy, C.; Pospisil, S. Characterization of the Radiation Field in the ATLAS Experiment With Timepix Detectors. *IEEE Trans. Nucl. Sci.* **2019**, *66*, 1861–1869. [CrossRef]

11. Dániel, V.; Inneman, A.; Pína, L.; Zadražil, V.; Báča, T.; Stehlíková, V.; Nentvich, O.; Urban, M.; Maršíková, V.; McEntaffer, R.; et al. X-ray Lobster Eye all-Sky Monitor for Rocket Experiment. In *EUV and X-ray Optics: Synergy between Laboratory and Space V*; SPIE: Prague, Czech Republic, 2017; p. 1023503. [CrossRef]

12. Urban, M.; Nentvich, O.; Báča, T.; Veřtát, I.; Maršíková, V.; Doubravová, D.; Dániel, V.; Inneman, A.; Pína, L.; Sieger, L.; et al. REX: X-ray experiment on the water recovery rocket. *Acta Astronaut.* **2021**, *184*, 1–10. [CrossRef]

13. Filgas, R. Space radiation monitoring with Timepix. *Astron. Nachrichten* **2018**, *339*, 386–390. [CrossRef]

14. Kroupa, M.; Bahadori, A.; Campbell-Ricketts, T.; Empl, A.; Hoang, S.M.; Idarraga-Munoz, J.; Rios, R.; Semones, E.; Stoffle, N.; Tlustos, L.; et al. A semiconductor radiation imaging pixel detector for space radiation dosimetry. *Life Sci. Space Res.* **2015**, *6*, 69–78. [CrossRef]

15. Stoffle, N.; Pinsky, L.; Kroupa, M.; Hoang, S.; Idarraga, J.; Amberboy, C.; Rios, R.; Hauss, J.; Keller, J.; Bahadori, A.; et al. Timepix-based radiation environment monitor measurements aboard the International Space Station. *Nucl. Instrum. Methods Phys. Res. Sect. A Accel. Spectrometers, Detect. Assoc. Equip.* **2015**, *782*, 143–148. [CrossRef]

16. Granja, C.; Polansky, S.; Vykydal, Z.; Pospisil, S.; Owens, A.; Kozacek, Z.; Mellab, K.; Simcak, M. The SATRAM Timepix spacecraft payload in open space on board the Proba-V satellite for wide range radiation monitoring in LEO orbit. *Planet. Space Sci.* **2016**, *125*, 114–129. [CrossRef]

17. Gohl, S.; Bergmann, B.; Evans, H.; Nieminen, P.; Owens, A.; Posipsil, S. Study of the radiation fields in LEO with the Space Application of Timepix Radiation Monitor (SATRAM). *Adv. Space Res.* **2019**, *63*, 1646–1660. [CrossRef]

18. Filgas, R.; Malich, M.; Kuwahara, T.; Broulím, J.; Holík, M.; Sakal, M.; Murata, Y.; Tomio, H.; Gohl, S.; Pineda T.J.M. RISEPix—A Timepix-based radiation monitor telescope onboard the RISESAT satellite. *Astron. Nachrichten* **2019**, *340*, 674–680. [CrossRef]

19. Urban, M.; Nentvich, O.; Stehlikova, V.; Baca, T.; Daniel, V.; Hudec, R. VZLUSAT-1: Nanosatellite with miniature lobster eye X-ray telescope and qualification of the radiation shielding composite for space application. *Acta Astronaut.* **2017**, *140*, 96–104. [CrossRef]

20. Baca, T.; Jilek, M.; Vertat, I.; Urban, M.; Nentvich, O.; Filgas, R.; Granja, C.; Inneman, A.; Daniel, V. Timepix in LEO Orbit onboard the VZLUSAT-1 Nanosatellite: 1-year of Space Radiation Dosimetry Measurements. *J. Instrum.* **2018**, *13*, C11010. [CrossRef]

21. Daniel, V.; Inneman, A.; Vertat, I.; Baca, T.; Nentvich, O.; Urban, M.; Stehlikova, V.; Sieger, L.; Skala, P.; Filgas, R.; et al. In-Orbit Commissioning of Czech Nanosatellite VZLUSAT-1 for the QB50 Mission with a Demonstrator of a Miniaturised Lobster-Eye X-Ray Telescope and Radiation Shielding Composite Materials. *Space Sci. Rev.* **2019**, *215*, 40. [CrossRef]

22. Furnell, W.; Shenoy, A.; Fox, E.; Hatfield, P. First results from the LUCID-Timepix spacecraft payload onboard the TechDemoSat-1 satellite in Low Earth Orbit. *Adv. Space Res.* **2019**, *63*, 1523–1540. [CrossRef]

23. Urban, O.; Vavroch, O.; Poláček, L.; Georgiev, V.; Burian, P.; Turjanica, P.; Fiala, P.; Broulím, P.; Bergmann, B. Hodoscope with Timepix detectors for PilsenCube2 cubesat. *Nucl. Instrum. Methods Phys. Res. Sect. A Accel. Spectrometers Detect. Assoc. Equip.* **2020**, *980*, 164462. [CrossRef]

24. Granja, C.; Hudec, R.; Maršíková, V.; Inneman, A.; Pína, L.; Doubravova, D.; Matej, Z.; Daniel, V.; Oberta, P. Directional-Sensitive X-ray/Gamma-ray Imager on Board the VZLUSAT-2 CubeSat for Wide Field-of-View Observation of GRBs in Low Earth Orbit. *Universe* **2022**, *8*, 241. [CrossRef]

25. Christe, S.; Glesener, L.; Buitrago-Casas, C.; Ishikawa, S.N.; Ramsey, B.; Gubarev, M.; Kilaru, K.; Kolodziejczak, J.J.; Watanabe, S.; Takahashi, T.; et al. FOXSI-2: Upgrades of the Focusing Optics X-ray Solar Imager for its Second Flight. *J. Astron. Instrum.* **2016**, *5*, 1640005. [CrossRef]

26. Krucker, S.; Christe, S.; Glesener, L.; McBride, S.; Turin, P.; Glaser, D.; Saint-Hilaire, P.; Delory, G.; Lin, R.P.; Gubarev, M.; et al. The Focusing Optics X-ray Solar Imager (FOXSI). In *Proceedings Volume 7437, Optics for EUV, X-ray, and Gamma-Ray Astronomy IV*; SPIE: San Diego, CA, USA, 2009; p. 743705. [CrossRef]

27. Urban, M.; Doubravová, D. Timepix3: Temperature influence on X-ray measurements in counting mode with Si sensor. *Radiat. Meas.* **2021**, *141*, 106535. [CrossRef]

28. Urban, M.; Nentvich, O.; Marek, L.; Hudec, R.; Sieger, L. Timepix3: Temperature Influence on Radiation Energy Measurement with Si Sensor. *Sensors* **2023**, *23*, 2201. [CrossRef] [PubMed]

29. Llopart, X.; Ballabriga, R.; Campbell, M.; Tlustos, L.; Wong, W. Timepix, a 65k programmable pixel readout chip for arrival time, energy and/or photon counting measurements. *Nucl. Instrum. Methods Phys. Res. Sect. A Accel. Spectrometers, Detect. Assoc. Equip.* **2007**, *581*, 485–494. [CrossRef]
30. Poikela, T.; Plosila, J.; Westerlund, T.; Campbell, M.; Gaspari, M.D.; Llopart, X.; Gromov, V.; Kluit, R.; Beuzekom, M.V.; Zappon, F.; et al. Timepix3: A 65K channel hybrid pixel readout chip with simultaneous ToA/ToT and sparse readout. *J. Instrum.* **2014**, *9*, C05013. [CrossRef]
31. Fiederle, M.; Procz, S.; Hamann, E.; Fauler, A.; Fröjdh, C. Overview of GaAs und CdTe Pixel Detectors Using Medipix Electronics. *Cryst. Res. Technol.* **2020**, *55*, 2000021. [CrossRef]
32. Turecek, D.; Jakubek, J.; Trojanova, E.; Sefc, L.; Kolarova, V. Application of Timepix3 based CdTe spectral sensitive photon counting detector for PET imaging. *Nucl. Instrum. Methods Phys. Res. Sect. A Accel. Spectrometers Detect. Assoc. Equip.* **2018**, *895*, 84–89. [CrossRef]
33. Frojdh, E.; Campbell, M.; Gaspari, M.D.; Kulis, S.; Llopart, X.; Poikela, T.; Tlustos, L. Timepix3: First measurements and characterization of a hybrid-pixel detector working in event driven mode. *J. Instrum.* **2015**, *10*, C01039. [CrossRef]

Chapter 4
Applications in space

The Timepix family of hybrid pixel detectors has found numerous applications in a wide range of scientific and industrial fields due to its high spatial and energy resolution, fast readout and radiation hardness. One of the most challenging and exciting areas where Timepix detectors have been used is space exploration and research. Space missions have unique technical and environmental constraints that require robust, versatile and radiation-hardened sensors which can operate under harsh conditions in order to measure different types of radiation. Timepix detectors have proven to be a reliable and flexible devices for numerous space applications [42], from their installation on the International Space Station (ISS) as an instrument for measuring the radiation environment [43], through several satellites with Timepix as a payload (ESA's Proba-V [14, 44], British TechDemoSat-1 [16], and Japanese RISESat [15]), to their exposure in open space on board one of the CubeSat missions, e.g. for measuring incoming radiation from the Sun, space or Earth's radiation background [7].

Their purpose is not only radiation monitoring, dosimetry and spectroscopy or observing of cosmic sources but also technology demonstration and validation of new concepts. This chapter summarises a brief overview of selected space applications of Timepix-based instruments and experiments, as well as the application of the results of this thesis in which I was involved.

4.1 VZLUSAT-1

The nanosatellite VZLUSAT-1 is a CubeSat mission developed by the Czech Aerospace Research Centre (VZLU) in the Czech Republic and was launched into low Earth orbit (LEO) orbit on 23rd June, 2017. The primary objective of the VZLUSAT-1 mission was to demonstrate the feasibility of using advanced materials and technologies for space applications and to achieve higher a Technology Readiness Level (TRL) for several materials [8]. The nanosatellite was designed and built by a team of researchers and engineers from VZLU, Czech Technical University in Prague (CTU), and University of West Bohemia (UWB). The nanosatellite was also developed in collaboration with other Czech universities and companies.

With dimensions of $10\,\mathrm{cm} \times 10\,\mathrm{cm} \times 34\,\mathrm{cm}$ and a weight of less than $2\,\mathrm{kg}$, VZLUSAT-1 is an example of a CubeSat, a standardised type of satellite that has become increasingly popular in recent years due to its low cost and relatively short development time. VZLUSAT-1 is equipped with several scientific instruments, including a radiation dosimeter and an X–ray telescope consisting of a combination of Lobster-Eye optics and the Timepix detector.

The detector interface has been modified for proper communication with the main computer and for placement on the CubeSat. An additional passive heat sink was attached to the detector itself (see Figure 4.9). During the thermal vacuum tests, it was shown that this heatsink allows the detector to operate in a continuous scanning mode, but its temperature rises up to $60\,°\mathrm{C}$.

Although the lifetime of this nanosatellite was initially estimated at one to two years, it is still operational in 2023 and providing valuable low Earth orbit data. For example,
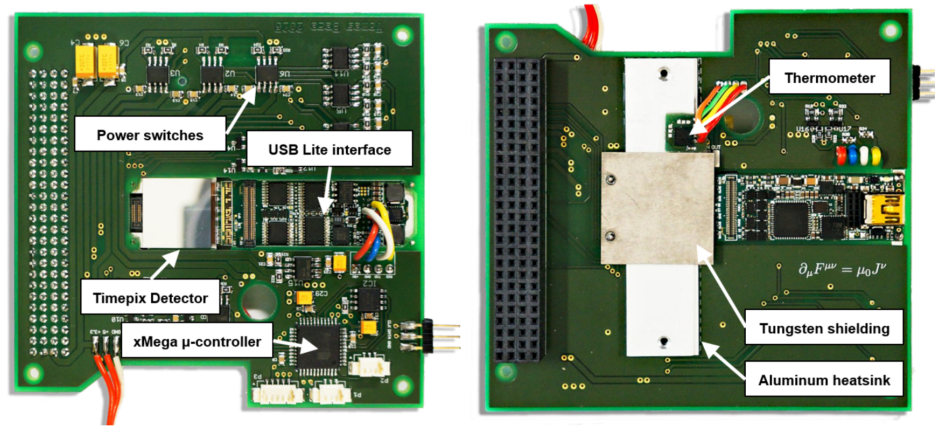
Fig. 4.9: Timepix detector as part of the VZLUSAT-1 payload board [45].

the long-term thermal data acquired on board the nanosatellite (orbiting at LEO) reveal that the thermal range inside the satellite is from $-5\,°C$ to $42\,°C$. It was measured by the Timepix detector, which also provides the long-term dosimetry map or solar flare data. It can therefore be expected that the measured energies, in this case, will also be affected by the distortion already described in this thesis. Since information about the temperature of the detector or its heat sink is known for each frame, this temperature distortion can be at least partially reduced, even retrospectively. In this case, it is necessary to use a generalised model based on a reasonable number of measurements with detectors in the same configuration, as demonstrated previously in this thesis.

However, the Timepix capabilities can also be used for space weather monitoring and dosimetric measurements, e.g. by filtering out individual events based on the track of a particle and its energy, the type of radiation can be determined, as shown in Figure 4.10.

(a) dots **(b)** blobs **(c)** straight tracks

(d) curly tracks **(e)** low resolution tracks **(f)** track examples

Fig. 4.10: Radiation map of the Earth based on the intensity of different particle types from the shape of their tracks [45].

CrossMark
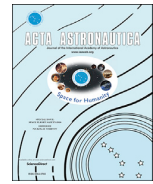
VZLUSAT-1: Nanosatellite with miniature lobster eye X-ray telescope and qualification of the radiation shielding composite for space application

Martin Urban [a], Ondrej Nentvich [a], Veronika Stehlikova [a,*], Tomas Baca [a], Vladimir Daniel [b,**], Rene Hudec [a]

[a] Faculty of Electrical Engineering, Czech Technical University, Prague, Czech Republic
[b] Aerospace Research and Test Establishment, Prague, Czech Republic

ABSTRACT

In the upcoming generation of small satellites there is a great potential for testing new sensors, processes and technologies for space and also for the creation of large in situ sensor networks. It plays a significant role in the more detailed examination, modelling and evaluation of the orbital environment. Scientific payloads based on the CubeSat technology are also feasible and the miniature X-ray telescope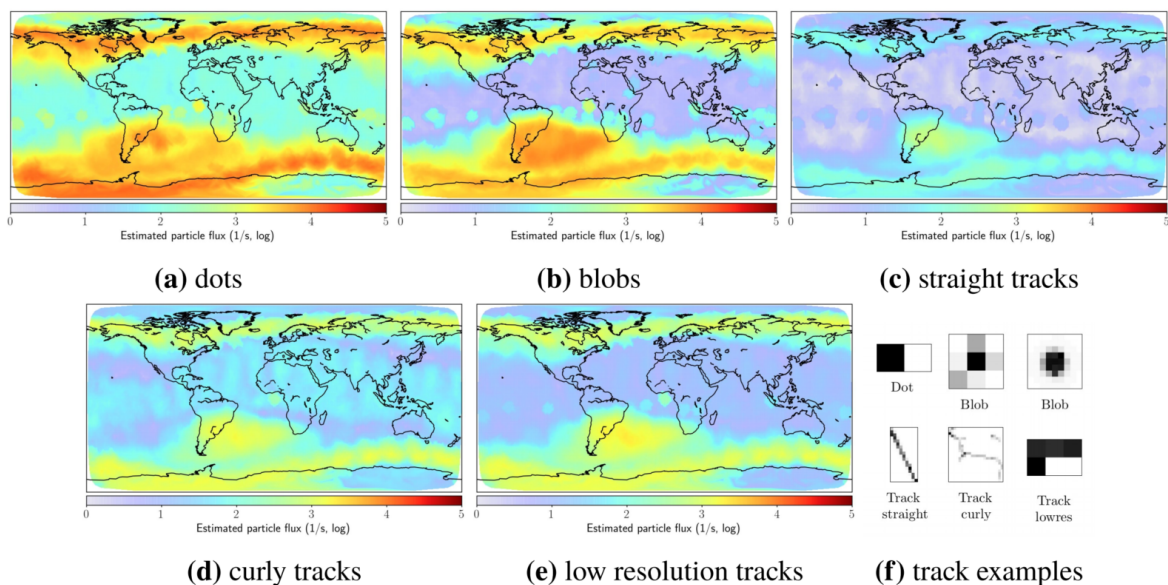 described in this paper may serve as an example. One of these small satellites from CubeSat family is a Czech CubeSat VZLUSAT-1, which is going to be launched during QB50 mission in 2017. This satellite has dimensions of 100 mm × 100 mm × 230 mm. The VZLUSAT-1 has three main payloads. The tested Radiation Hardened Composites Housing (RHCH) has ambitions to be used as a structural and shielding material to protect electronic devices in space or for constructions of future manned and unmanned spacecraft as well as Moon or Martian habitats. The novel miniaturized X-ray telescope with a Lobster Eye (LE) optics represents an example of CubeSat's scientific payload. The telescope has a wide field of view and such systems may be essential in detecting the X-ray sources of various physical origin. VZLUSAT-1 also carries the FIPEX payload which measures the molecular and atomic oxygen density among part of the satellite group in QB50 mission. The VZLUSAT-1 is one of the constellation in the QB50 mission that create a measuring network around the Earth and provide multipoint, in-situ measurements of the atmosphere.

1. Introduction

The main idea of QB50 mission is to demonstrate the possibility of launching CubeSats and scientific utilization. These satellites are designed as a part of a global sensor mesh to perform in-situ measurement in the largely unexplored lower thermosphere [1].

Due to the low orbit of the satellites, their orbital lifetime is limited. With respect to this fact, space agencies are not pursuing a satellite network from industrial satellites for an in situ measurement in the lower thermosphere, because creation of such a network would be very expensive. Measurements in low atmosphere can be nowadays conducted by sounding rockets, however that is a single-point measurement with a duration of only several minutes. One of the options is to use low-cost satellites i.e. CubeSats [2]. These small satellites can realize a network of satellites for in-situ measurements in the lower thermosphere and provide multipoint measurements for a longer time period [3]. Advan-

VZLUSAT-1 is a CubeSat type satellite. The idea of these small satellites is to prove a universal, cheap and lightweight platform mainly for universities and companies which want to test and verify new technologies on orbit or conduct scientific measurements [5] or create sensor networks.

Companies worldwide are manufacturing universal and compatible parts for CubeSats. Creation of a CubeSat can then be only assembling of construction kits. VZLUSAT-1 uses these prefabricated parts - On-board Computer (OBC), Electronic power system (EPS) as the most basic platform to manage power and radio board for communication with ground segment.

2. Scientific goals and motivation

The QB50 mission concept is predestined for swarm experiments. A constellation of satellites with the same experiment on-board will be created. VZLUSAT-1 is a technological satellite with three scientific experiments.

67/108

The first is a small X-ray telescope. X-ray observation of the sky is feasible by various devices, such as sounding rockets, high altitude balloons or X-ray telescopes placed on orbit. Nowadays, the Wolter type optics is commonly used in space experiments. These types of optics represent hollow mirrors, they consist of elliptical and parabolical or hyperbolical surfaces, work on total reflection principle and have approximately 0.5 deg wide field of view. Compared to this, VZLUSAT-1 carries wide-field Lobster Eye type X-ray optics, with parallel flat mirrors in Schmidt arrangement. Because this technology has never been used in orbit, an elementary, bright source of X-ray radiation - the Sun - was chosen for test imaging and technology demonstration (which is the main mission goal). The Lobster Eye optics is expected to focus X-ray images of the Sun in the energy band of 3–60 keV [6]. In the case the mission is successful, another telescope is expected to follow, with a larger optics, higher sensitivity and better angular resolution.

Another part of the VZLUSAT-1 mission is to examine a new material, which is Radiation Hardened Carbon Composite Housing (RHCH). This material is lightweight and due to its volumetric mass density it should be able to block low energy radiation and particles like protons and neutrons. The material slows down neutrons by elastic scattering. A detailed description can be found in chapter 5.3.2. There are several other missions and experiments focused on this problematic [7,8].

The last experiment is the FIPEX. This experiment is focused on the study of residual oxygen in incriminated layer of the atmosphere. Information about this element is interesting for scientific models of the atmosphere. Proportion of oxygen to other elements in the air changes during long-time periods, in the last period it was 10–35%. The amount of oxygen has an influence on the absorbed surface radiation in units of W m^{-2} and can show a connection with global warming [9,10]. It can also have relation to corrosion of spacecraft on orbit [5].

3. Concept of operations

The satellite will be stabilized in attitude tangential to the orbit, with FIPEX instrument on the prow. This placement is important for the best efficiency of the measurement. On the prow, FIPEX sensors have ideal circumstances for gathering oxygen particles. During the flight, position will be corrected by magneto-torquer coils, so this endpoint experiment orientation is guaranteed ±10 deg. Also the whole satellite can be oriented towards the Sun or other X-ray sources for taking pictures. Observation can be started by an automatic trigger, made of UV diodes. When irradiated, it gives a signal to make a picture. The satellite will be exposed to space radiation from far space as well as from the Sun. It will also receive doses from Van Allen belts while orbiting. These total doses are going to be measured by XRB diodes and by a CdTe detector. VZLUSAT-1 will carry RHCH as well. The RHCH is going to be tested for its properties and suitability for shielding radiation and for making construction parts for next space projects like spacecraft or habitats, where the protection of human crew against radiation is needed [11].

The data will be sent twice a day to the ground operational station in Pilsen (Czech Republic) for further processing. Because of limited downlink, basic operations with data will be done on orbit. For example, a picture from the X-ray payload is compressed by binning, from which an on-earth operator can consider whether the real image contains valuable data. During another connection with the satellite, a larger image format can be downloaded on demand.

4. Spacecraft

4.1. Overview

The science mission fits to a small spacecraft, the CubeSat's form factor suits well its requirements. All used payloads and subsystems comprising the satellite were tested in Aerospace Research and Test Establishment, Prague. VZLUSAT-1 includes all necessary submodules for standalone autonomous operations and meets the requirements
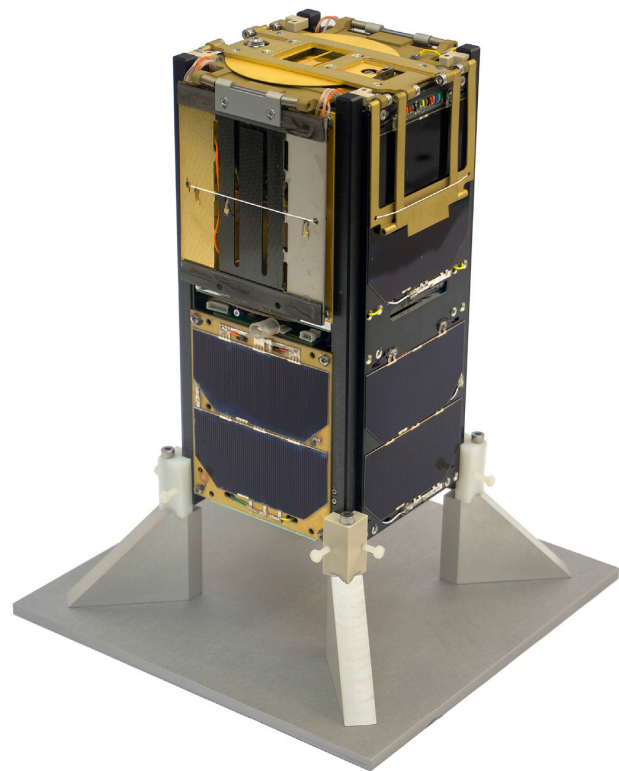
Fig. 1. Folded VZLUSAT-1 satellite placed in a stand.

imposed by the QB50 mission (see Fig. 1).

One of the systems for determining the exact position of VZLUSAT-1 is an array of retroreflectors. A network of ground stations is built around the Earth, capable of detecting satellites equipped with such mirrors. This localization principle was used for example for Chinese navigation satellite Compass-M1 and American-French Jason-2 [12,13]. The system allows to monitor the distance of the satellite with millimetre accuracy. The ground system consists of an ultra-short laser pulses generator and a single-photon detector with an extremely high time resolution and stability. The use of laser pulses provides a better position precision than radio waves. Precise position of the satellite is determined from the time shift and the elevation of a laser beam.

4.2. Structure

CubeSat units can be advantageously connected together as it is the case of VZLUSAT-1. This satellite consists of two units, its launch size is $100 \times 100 \times 230$ mm^3 and mass is 1.83 kg (see Table 1). VZLUSAT-1 has a deployable system which allows the satellite to expand its size up to three units in orbit. The number of units connected together depends on rules of the mission, financial possibilities of the project and requirements for experiments.

VZLUSAT-1 has three components, which are constructed to be situated at the end of the satellite - the LE optics, the FIPEX and antennas. For this reason, antennas were placed in the middle, on the joint between the two units, although it complicates the assembling. Deployable optics is placed on the top of the satellite, both sides are equipped with a deployable solar panel and a Health monitoring panel. The HM panel is made of a carbon fibre reinforced plastic (CFRP) material with additive manufacturing forming the RHCH. The retroreflector array is placed under the HM panel. A detailed description of the location of the individual parts is in Fig. 2.

This panel carries corner reflectors (retroreflectors) to determine the

Table 1
VZUSAT-1 properties.

Property	Value
Dimensions	$100 \times 100 \times 230 \text{ mm}^3$ folded (2U)
	$100 \times 100 \times 340 \text{ mm}^3$ deployed (3U)
Launch mass	1.83 kg
Power	2 W
Main experiments	Miniaturized X-ray telescope,
	RHCH, FIPEX
Type of orbit	Polar, circular
Orbit altitude	500 km $\pm$ 20 km
Repeat cycle	12 h
Mission lifetime	2 years

Fig. 2. Boards and payloads on VZUSAT-1.

position of the nanosatellite with high accuracy. The corner reflection consists of three mutually perpendicular mirrors, there are 16 corner reflectors placed on panel.

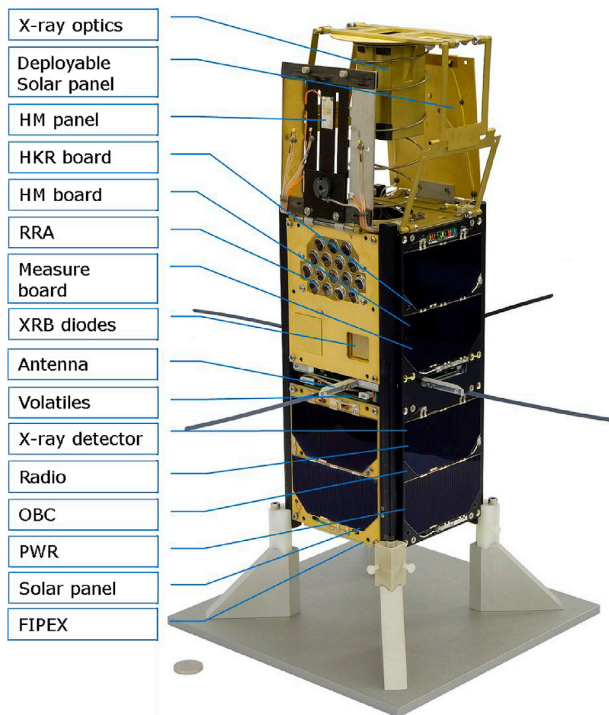Three X-ray sensitive XRB diodes are placed below the reflectors with different shielding for differential measurement of RHCH shielding effectivity. XRB diodes are placed on a board which is mounted perpendicular to a Measure board, providing radiation and temperature measurement. On the bottom side of the first unit there are antennas, which are curled inside the body of the CubeSat and are secured by wires during the launch. After achieving the orbit, the wires will be overburnt and antennas will protrude out. A Volatiles board is on the top of the second cube (in the middle of the CubeSat), it measures the evaporation of residual humidity from the whole body of the satellite with emphasis on RHCH material. The bottom Cube consists of the following parts: an X-ray board with a Timepix detector, an OBC controlling general functionality of the spacecraft, a Radio board providing communications with the ground station and the last one is an Electronic power system (EPS) with two backup rechargeable batteries and with an energetic manager.

The structure was designed to survive the launch without degradation or components loss. The completely assembled VZLUSAT-1 was tested on vibration plateau. All the tests were performed in compliance with the QB50 requirements.

4.3. Power system

The power system is an elementary board which provides power for all systems. The power system consists of solar panels for energy generation, Electronic Power System (EPS) board NanoPower P31u, and two Lithium-ion backup accumulator cells configured serial. There are two solar panels with 2 U format and one panel with 3 U format on the nanosatellite (more in Table 2). The biggest panel is assembled of two fixed and one deployable part. All solar panels have three layers - InGaP, GaAs and Ge layers on a Germanium underlay. Each of these layers absorbs different wavelengths, from UV to IR. The effectiveness in orbital conditions, that means a mean power density of 1367 W m^{-2}, is 30%. The solar panels will also receive the Earth albedo and the Earth infra-red radiation as illustrated in Fig. 3. The area of one solar panel is approximately 30 cm^2. Each of them can generate up to 2.4 V and 500 mA. Solar panels are connected to the EPS board. The board manages charging of accumulators, battery protection, generating the required voltages and power distribution.

The battery system is based on Lithium-Ion accumulators with under and over voltage protection, current limiter for shortcircuit case and battery heater as protection against capacitance loss at low temperatures. As the type of batteries used is sensitive to undervoltage, the board measures the voltage and if it drops below a critical value, the EPS gradually cuts off the power to all systems. Finally, it even cuts off the power to the OBC. After the accumulators are charged, it switches the satellite on again.

Average power income has been simulated in Matlab software based on $1 \times 1 \text{ U} + 2 \times 2 \text{ U} + 3 \text{ U}$ of solar panels placement and given the orbit inclination 98 deg. (Fig. 4 - green curve). For the Commissioning mode the situation with closed deployable panels was assumed $70\% \times 2 \text{ U} + 1$ U (Fig. 4, the magenta curve). The power from solar cells vs. time of year has been evaluated for different RAAN (right-ascension of ascending node) and plotted a diagram in Fig. 4.

Table 2
Main features of NanoPower P31u [14].

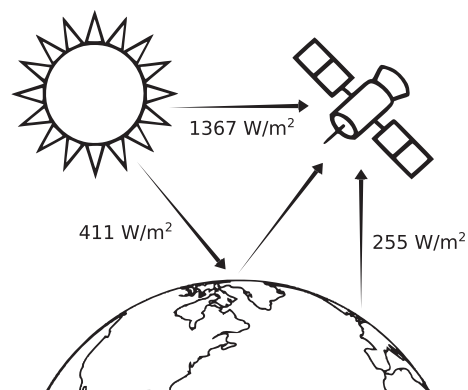| Property	Value
Type of Power Storage	Lithium-Ion Cell
Capacity	18 Wh
Battery Protection	under-voltage, over-voltage, current limiter,
	Watchdog, heater
Available Voltages and	3.3 V @ 5 A
Sustainable Currents	5 V @ 4 A
Type of Solar Panels	GaAs
Number of Solar Panels	2×2 U format on sides
	1×3 U format (2 fixed and 1 tilting) zenith
	1×1 U format nadir

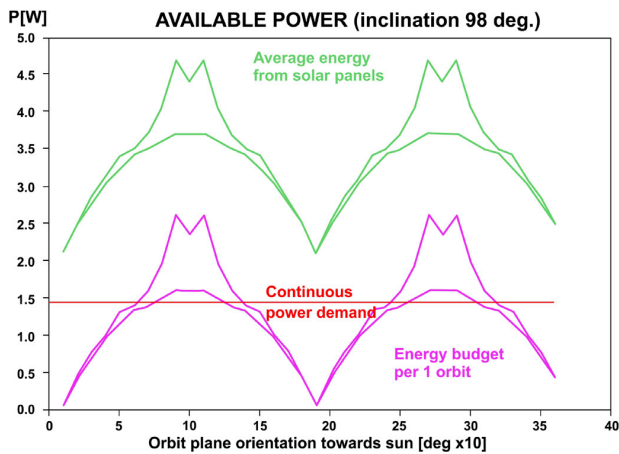**Fig. 3.** Power densities of different sources on the orbit.

Fig. 4. Solar power input base on RAAN.

4.4. Commands and data handling

There is a board dedicated to data handling and commands executing on VZLUSAT-1. All these operations are managed by the On-board computer NanoMind A712D. Main features are in Table 3 [15].

This board is responsible for commanding and monitoring of all subsystems and nanosatellite's payloads. They are connected to OBC according to a diagram in Fig. 5. Communication is based on CubeSat Space Protocol (CSP).

Main I²C bus as well as power for other boards is switched by OBC. The boards on the main I²C bus work in multimaster mode. One of the main OBC tasks is the Datakeeper task and has one of the most important functions, data storing and operations. There are two types of data storages on the OBC. The first is the 4 MB Flash memory and the second one is 512 MB microSD card which can be used as backup. The planner task is intended for managing other payloads such as powering on, parameter settings and measure commands. This managing can be divided into two types. The first type is one time actions, such as powering on of boards. Return messages of these commands are stored directly by the OBC without processing by Planner. The second type is Housekeeping collector (HKC) which performs periodic commands like cyclic measurements. The HKC has three parameters: Period of measurement, commands and time of start. Results of HKC are stored directly by OBC to the Datakeeper.

4.5. Attitude determination and control system

The attitude determination and control subsystem of VZLUSAT-1 consists of only magnetometer sensing and only magneto-torquer active control. A single 3-axis vector magnetometer on-chip instrument is included (Honeywell HMC5843). The reaction wheel is not used in the VZLUSAT-1 for stabilization but instead we used magneto-torquer coils. Four magneto-torquer coils are connected in two pairs, one for X and one for Y axis. For the Z axis only one coil is used, but it has double inductance. These coils are used as actuators. Hardware drivers of these coils are H-bridges that are integral part of the OBC board as well as the

Table 3
Main features of OBC board.

Property	Value
Processor	32-bits ARM7 - 8–40 MHz
RAM	2 MB of SRAM
Flash	4 MB for Code, 4 MB for data
Peripherals	CAN, I²C, aux I²C, SPI, USART
Other	RTC, magnetometer, microSD, GPIO

magnetometer (HMC5843).

The ADCS software is implemented directly on the OBC. It is a part of the on-board software which is predominantly of in-house design except for the FreeRTOS on which it is based. The in-house designed control algorithm is based on knowledge of the aerodynamic properties of the nanosatellite. The external surfaces of the nanosatellite together with properly positioned centre of mass of the deployed structure of the satellite assure that the desired flight attitude corresponds to the absolute minimum of potential energy of the aerodynamic interaction.

A key point of the control algorithm is that it monitors the energy of the rotational motion of aerodynamically modulated rotational or oscillatory motions of the nanosatellite by monitoring the magnitude and the direction of the instantaneous magnetic field vector of angular velocity.

This is accomplished by measuring the magnetic field of the Earth and by processing these measured data with the use of the model of the Earth's magnetic field together with model of the orbital trajectory of the nanosatellite using reduced Two-Line Element Sets uploaded to the satellite usually twice per a day. A key component of the subsystem is also a detailed enough map of the Earth's magnetic field. The map is computed from International Geomagnetic Reference Field (IGRF) model in the matrix of 9 deg longitude × 9 deg latitude. The map has 41 per 21 points (the first and the last point is doubled) and is in on-board software for the altitudes 450, 400, 350 and 300 km. The maximum vector error between map and the full IGRF model is 1.3 deg, the mean value is 0.4 deg.

The only magnetic field ADCS will be prone to the changes of the Earth magnetic field and geomagnetic storms. Due to geomagnetic storms, the value of the magnetic field intensity fluctuates. The Dst index (expressing the magnitude of geomagnetic storms) per the year 2000 was 20 nT on average. Some super-storm was measured with a Dst of about 600 nT [16]. This value covers about 3% of the total minimum intensity value of 22 000 nT of the Earth magnetic field in the South Atlantic anomaly. The mean Dst index value covers about 0.1% of the magnetic field intensity, so we expect about several percent influence of the mean geomagnetic storms to the orientation evaluation.

Stabilization is ensured by precise applying of actuators at appropriate times just to dissipate the rotational energy. Timing is very important in this action with respect to the effectiveness of the action. The highest efficiency is when the vectors of the Earth's magnetic field induction flux density and satellite angular velocity are perpendicular.

The attitude is calculated with the use of a regression model that fits the measured data of the magnetic field of Earth to the magnetic field of Earth calculated using the IGRF model at known position. Components of the regression model include the equations of rotational motion of solid body (Euler equations), aerodynamic torques and a tensor of inertia of the satellite (see Fig. 6). The components of the angular velocity are calculated by a separate algorithm that processes the measured magnetic field of the Earth.

4.6. Communications systems

Every payload requires commands and configuration for its measurement and it generates data which also have to be downloaded to the Earth's ground station. The VZLUSAT-1 has a UHF radio board with antennas which provides communication with the ground station. This system is able to transfer measured data to the ground station as well as the upload new commands and configurations for next measurement. The main features of the communication between the ground segment and VZLUSAT-1 are in Table 4.

The nanosatellite orbits at altitude around 500 km at polar orbit. The connection with the satellite is once per 12 h for 7–10 min. The connection time depends on altitude of the satellite. During this time it is necessary to transfer as much data as possible in both directions. The first downloaded data are Whole Orbit Data (WOD) which contain basic information about the satellite. These can reveal a problem, usually with low power. The WOD are also transmitted by beacon. The basic configuration is the first information that is required to be uploaded. After that
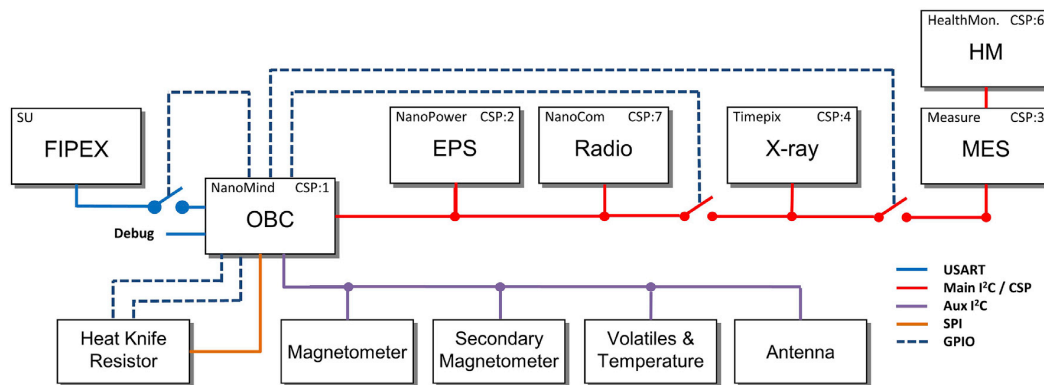
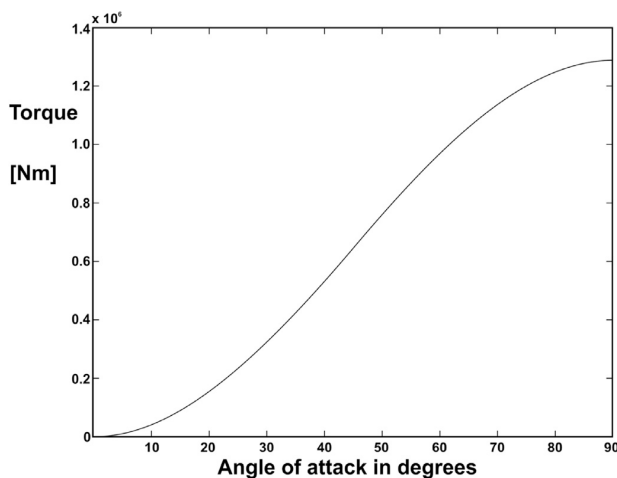**Fig. 5.** Schema of connection of all boards.

Fig. 6. Aerodynamic torque as function of angle of attack.

a planner script is uploaded which manages other payloads and measurements. This mission is limited by a very low uplink and downlink of commands, telemetry and data rate. It is caused by the usage of free non-licensed band and its widespread usage.

5. Scientific payloads

The payload objective of the VZLUSAT-1 project is the development, manufacturing, qualification and experimental verification of products and technologies in Earth's orbit (IOD In-Orbit Demonstration) and carrying the scientific payload FIPEX for the QB50 mission. There are two devices on the board: Radiation Hardened Composite Housing (RHCH) and a demonstrator of X-ray telescope, their functions and properties will be verified.

Table 4
Main feature of the Radio transmission.

Property	Value
Number of antennas	4× monopole antenna
Frequency of Connection	12 h
Connection Time	7-10 min
Carrier frequency	437.240 MHz
Downlink Data Rate	9600 Baud
Uplink Data Rate	9600 Baud
Polarization	Circular
Features	Morse, Beacon

5.1. Miniaturized X-ray telescope, the lobster-eye

Apart from technology in flight demonstration, this scientific experiment on VZUSAT-1 is mainly designed for all sky monitoring of bright sources in X-rays and detection of X-ray transients, due to a wide field of view. In the future, if LE type telescopes were used for all sky monitoring and the new transient was detected, more precise telescopes with a Wolter I type optics could be focused there and could study the event in more detail.

The miniature X-ray telescope/monitor on the VZUSAT-1 is based on the Lobster Eye (LE) optics with a non-cooled Timepix detector. The novel Lobster eye optics is a system of narrow shafts with right angles and straight walls. Unlike classic optical lenses, the picture is created by total reflection, not refraction [17].

The LE has a large field of view (FOV) of 3 deg compared to Wolter type optics which is usually used in X-ray astronomy. Wolter type optics has a field of view up to 1 deg and is used for detailed and sensitive observations of selected X-ray sources. The Timepix detector used as a focal image detector is sensitive to low energy radiation in the range 3–60 keV. In case a full two dimensional (2D) LE optics is used with a working spectral range up to 8 keV, there is an overlap of 3–8 keV for the overall spectral range of the miniature X-ray telescope. In case of one dimensional (1D) LE, the spectral overlap is 3–30 keV as there is only one reflection in the optical system.

The principle of LE optics is illustrated in Fig. 7. The special 1D LE was developed for this mission, in order to adjust the optics working spectral range with the Timepix focal detector. The focal length of the LE on VZUSAT-1 is 25 cm, the Timepix detector is located in this focal plane. In order to ensure this condition of transmission of X-ray to the Timepix detector there have to be holes in all boards, throughout almost the whole satellite, between tilted optics and the Timepix detector itself. The result of the 1D X-ray optics is line focus. Spacing of lines depends on the arrangement of coated foils. One example of a picture taken by the Timepix is in Fig. 8.

The Timepix is a Complementary MetalOxide Semiconductor (CMOS) silicon detector for low-energy X-rays, approximately 3–60 keV. Originally, it was developed for the Large Hadron Collider (LHC) of the European Organization for Nuclear Research (CERN). Nowadays it is also used as a radiation monitor for orbital missions [19] or as medical instrument for scanning soft tissues. This variant has limited number of modes and is called a Medipix.

X-ray board holding the Timepix sensor has several operation modes. One of them is a signal detection mode from Infrared (IR) and Ultraviolet (UV) sensors. The X-ray board has two UV sensors and one IR sensor. All sensors are used for determination of a more precise position of the Earth by IR sensor or the Sun by UV sensors. One of the UV diodes has a wide field of view and it is designated for the Sun. When the output signal is strong enough, the Timepix switches on. The second UV sensor has a
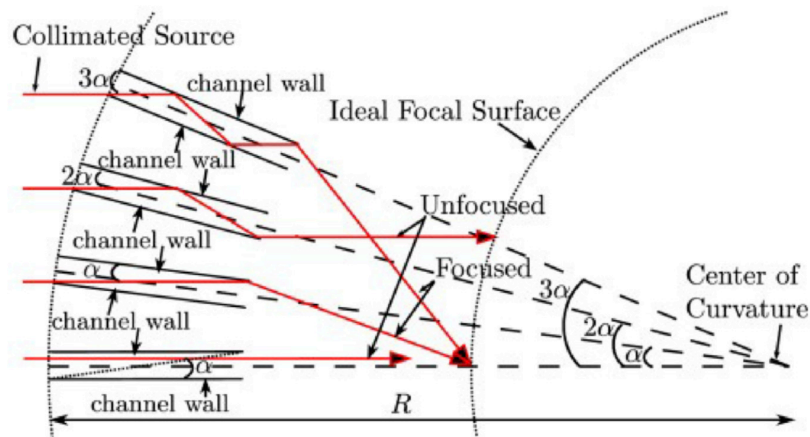
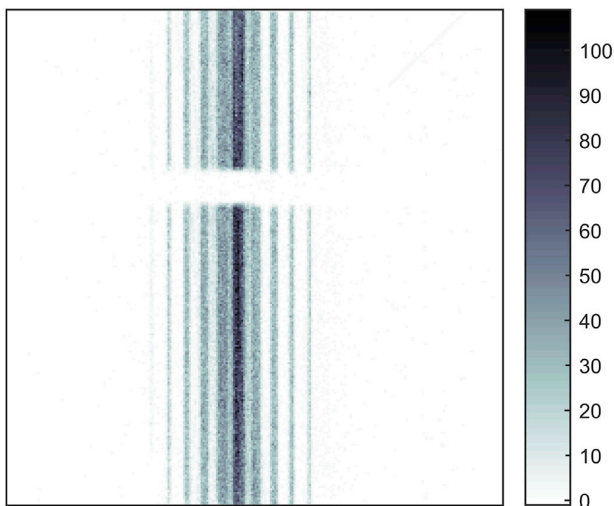**Fig. 7.** Schematic principle of the Lobster Eye optical device [18].

Fig. 8. Picture taken by the Timepix (14×14 mm^2 with resolution 256×256 px) with the 1D Lobster Eye optics during a protoflight testing procedure. Number of counts is presented in each pixel. Gold Mini-X X-ray 50 kV Tube with a set power at (40 kV/50 μA) and exposure of 10 000 ms at 3 m distance is used as an X-ray source.

narrower field of view and it gets more precise position of the Sun. When the signal from the second UV sensor is better than the preset trigger value, the Timepix takes a picture.

5.2. FIPEX

According to the main idea of the QB50 mission, a satellite network measurement will be created all around the orbit to perform in-situ measurements in lower thermosphere. This layer of atmosphere is not mapped well, because a solo mission for thermosphere has not been launched yet and atmosphere scientists have only data from single-point sounding rockets and similar experiments, not from a long time mission. The QB50 project has prescribed three sets of sensors, dedicated for different measurements in the thermosphere, and each CubeSat team had to choose one of these sets.

The teams could choose from an Ion-Neutral Mass Spectrometer, a Flux-Φ-Probe Experiment (FIPEX) and a multi-Needle Langmuir Probe. Each of them is accompanied by thermosensors and they are part of the future scientific network of sensors in the thermosphere layer. VZUSAT-1 has a Flux-Φ-Probe Experiment on board. This experiment studies the

behaviour of atomic oxygen (AO) and molecular oxygen O_2 in the lower thermosphere, compared to other missions [20] that measured nitrogen, hydrogen and carbon compounds. Oxygen is dominant in the incriminated region and its measurement is important for validation of atmospheric models. Another reason is to research influence of oxygen on material surfaces, such as coatings of the International Space Station (ISS) which orbits in this altitude [21]. The measurement principle is based on oxide electrolyte micro sensors. These sensors operate at high temperature of around 600–700 °C and they are heated by an electrical resistance. For this reason this measurement is one of those with the highest power consumption on the nanosatellite.

The FIPEX is oriented on the bottom side of the satellite when standing on the ground. During the flight, this part must be on the prow, so the sensors will be exposed to the rest of atmosphere directly and will get as many particles as possible.

5.3. Radiation Hardened Composite Housing

Technologically the RHCH is based on the use of hardened metal layers deposited on the composite panel with an improved thermal conductivity and radiation properties. With an original combination of thin films and composite, the new housing is lighter and also more durable than aluminium alloys.

The RHCH base is formed by carbon fibres. We created a composite with a higher radiation resistance than is usual by using LETOXIT Foil Technology which uses a special adhesive LFX foil. For this specific use, the composite is milled into the desired shape. Before a galvanization coating, the surface of the product is treated by an ion beam. It removes the majority of the remaining moisture and finishes the surfaces for galvanization in a bath. During the galvanization process nickel, which is ferromagnetic, is used. As the VZLUSAT-1 is using magneto-torquers and magnetometer for stabilization, a non-magnetic material is desirable for the correct function of the ADCS. To obtain a non-magnetic material, a combination of nickel and phosphorus is used. Galvanization creates a coating with a thickness of 50 μm.

To verify the properties of the developed RHCH the satellite is equipped with a Health Monitoring (HM) system. The HM system includes temperature, volatiles, radiation and mechanical properties sensors.

5.3.1. Mechanical properties of RHCH

Every material has few properties which are characteristic for them - material density, modulus of elasticity, radiation shielding quality and others. Mechanical properties of any material are characterized by Young's modulus of elasticity. It represents the stiffness of the material. For further usage of the RHCH i.e. for making construction parts for new
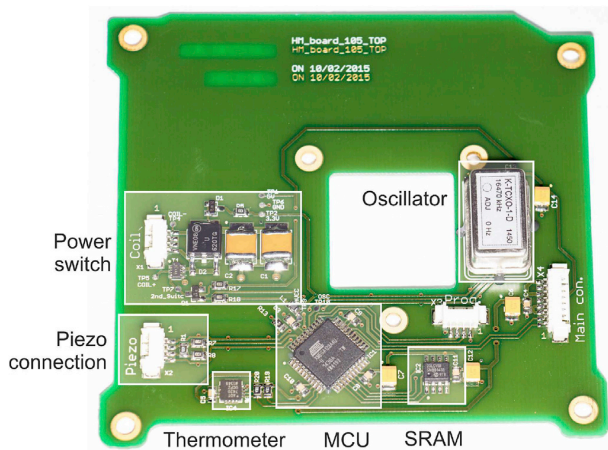
Fig. 9. Health monitoring board with labels.

satellites or Martian habitats it is required to know how these properties change in time during a longer period of exposure in space. Usual orbits of CubeSats are lower than the altitude where the VZLUSAT-1 will operate, their life-time is usually one year. The expected two years life-time promises to show at least the trends of material degradation, although even longer tests would be desirable. On the other hand, these tests will be performed in real, complete orbital environment, which is very complicated to simulate on Earth in the whole scale of its parameters.

The quality of the RHCH can be affected by radiation, low pressure or high and low temperatures. So for this purpose the VZLUSAT-1 is equipped with the payload for measuring of the Young's modulus and a damping coefficient of the RHCH by non-destructive testing, which is part of the HM system. The system for measuring mechanical properties has two parts. One is the HM panel, which is in Fig. 10 and the HM board in Fig. 9, which processes all results of this measurement.

The Young's modulus is calculated from the eigenfrequency of the free cantilever oscillations. The cantilever is made of the RHCH material with
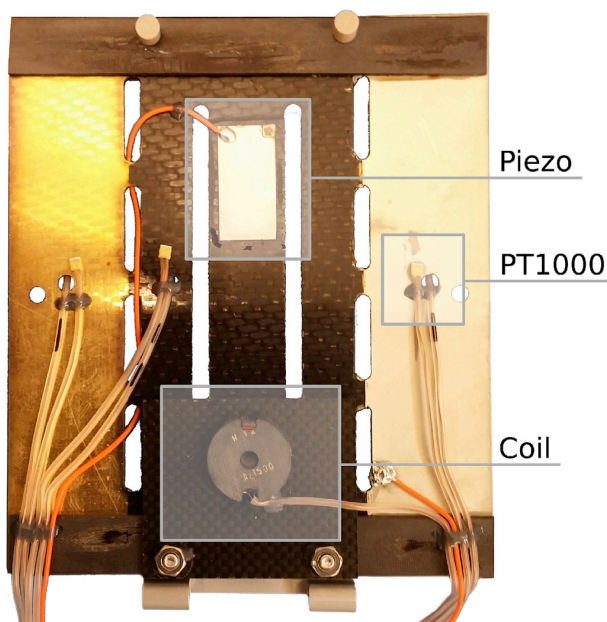

Fig. 10. HM panel with cantilever.

a small permalloy target on a free end in they centre of the HM panel [22]. The cantilever is excited by an electro-magnetic pulse by a coil located above the permalloy. This mechanism generates mechanical sine vibrations with an exponential damping. A piezo element which senses vibration is placed at the fixed end of the cantilever. To recognize ageing, a small frequency shift in RHCH's natural frequencies and the damping factor of the sensed signal have to be measured. Natural frequencies are calculated directly on board by a microcontroller. The microcontroller computes a Fast Fourier transform (FFT) with 8192 points at a sampling frequency of 4000 Hz. The resolution of this method is 0.5 Hz. The damping factor of the sampled signal also examines mechanical properties. The factor represents an envelope of the signal. Both factors determine the changes in mechanical properties (Young's modulus of elasticity) and ageing properties. The raw signal can also be saved and downloaded for ground recalculation. This data transfer is requested and will be only used occasionally.

5.3.2. Radiation properties measurement of RHCH

On the Earth's orbit, there are different types of radiation sources like the Sun, Galactic cosmic rays (GCR) and a trapped radiation (Van Allens radiation belts). The Sun is the source of protons, some types of ions, electrons, gamma rays and X-ray. Cosmic radiation at low intensity is due to protons and ions in the energy band of 10^8 eV–10^{20} eV. The main part of radiation in Van Allen radiation belts is created by trapped electrons with energies usually from 10^5 eV to 10^7 eV, that will be crossed by the CubeSat.

There are three uncooled XRB diodes on the VZLUSAT-1 used for radiation shielding measurement. XRB diodes are based on silicon with a high resistivity capable of detecting radiation with energies of 15 keV–60 keV (with the supply voltage of 70 V it reaches the absolute detection efficiency of 32% of the radiation energy of 20 keV).

Lower energy radiation is filtered by a radiation-resistant window, which together with a guard ring reduces detector's noise. XRB diodes are capable of measuring radiation even without power. Applied bias voltage improves the efficiency of detection of higher energies of X-ray radiation, but also increases the amount of the dark current.

Evaluation of the shielding quality of the RHCH is based on differential method. This arrangement of measurement is shown in Fig. 11 where there are three XBR diodes with different shielding. These results are based on the variance between them. We simulated the radiation background with an Americium-241 gamma source, which has two main peaks at 18 keV and 59.6 keV. This source cannot faithfully imitate the orbital environment, but this was not the goal. The goal was to evaluate the differences between diodes to get relevant data during the flight. During tests, results between composite and other materials (Aluminium, Tungsten, solar panels, circuit boards) were compared. The result is shown in Fig. 12.

The shielding abilities of the RHCH are similar to Aluminium. Compared to it, the composite is lighter and more stiff. The advantage of this combination is being applied in cases when the material is not used only as a shield, but also as a construction material which is the case of VZLUSAT-1.

5.3.3. Volatiles

Part of the properties verification of the new carbon fibre reinforced plastic (CFRP) used as the RHCH is, beside the study of radiation resistance effectivity, the measurement of mechanical properties and evaluation of changes and also an additive measurement of evaporation, water vapour and other gasses emissions from the material. The electric charge of water molecules has an asymmetrical distribution, and it means that they are easily absorbed on almost any surface like construction parts of the satellite, boards and so on. Vaporized water, or other gases, can cause considerable difficulties in space. Evaporated water molecules can condensate on other satellite parts for example on electronic devices, printed circuit boards or other and cause a short-circuit on the board and damage the whole device. Molecules can also condense on optical lens or
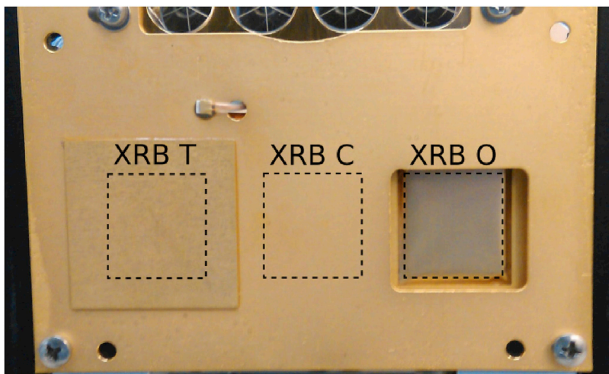
Fig. 11. XRB diodes on VZLUSAT-1, each one with different shielding - both tungsten and RHCH on the left (XRB T), only RHCH in the middle (XRB C), unshielded on the right (XRB O).
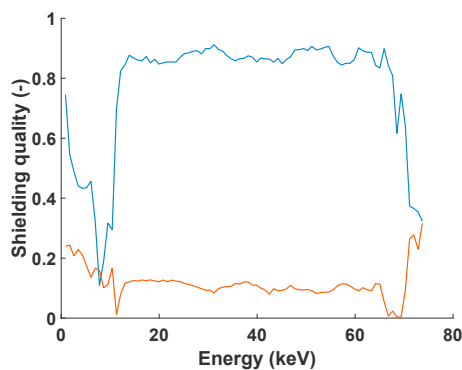

Fig. 12. Efficiency of radiation shielding - Tungsten (blue) and RHCH (orange) shielding are compared. (For interpretation of the references to colour in this figure legend, the reader is referred to the web version of this article.)

sensitive chips for image scanning and thus disable the whole process.

The volatiles board serves for the measurement of residual humidity and outgassing from the satellite, especially from tested CFRP. This humidity will evaporate in the vacuum, mainly in the first hours after launch. There are three types of sensors on board. Two pairs of organic polymer sensors the HYT 271 and the HYT 939 are situated on both sides of the Volatiles board. Results of these sensors are the relative humidity and temperature. The third type is represented by inorganic HAL2 sensors based on Al_2O_3 [23] which are sensitive not only to humidity, but to
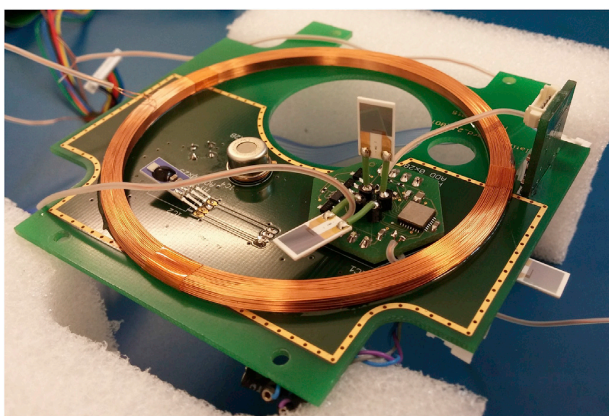
other gases as well. There are three pieces of these sensors located on the Volatiles board. One sensor is placed directly on the Volatiles board, the second one leads through to the neighbouring board on the satellite. Last of the HAL2 sensors is placed outside the VZLUSAT-1 and its active layer is directed in the flight direction. Placement of sensors on the board together with the magneto-torquer coil can be seen in Fig. 13. This unconventional placement allows measuring of the rest of water vapour directly in layers of the atmosphere. In the last years, volumes of different gases in the atmosphere were investigated during several missions [20] to consider the natural statement of the atmosphere as well as the influence and damages caused by artificial activity [24].

6. Conclusion

The VZLUSAT-1 nanosatellite will be launched in the year 2017 as a part of the QB50 mission. The altitude of the satellite will be 500 km at layers of the lower thermosphere. The research of the atmosphere suggested by Von Karman Institute (VKI) will be made by the scientific unit FIPEX and HAL2 volatiles sensors which are sensitive to vapour. The satellite carries several experiments with new materials and technologies, which will prove to be suitable for the use in space. One of the main payloads is the Timepix detector with the lobster eye optics, forming a miniature 1D LE X-ray telescope. This is a prototype of an astronomical LE X-ray telescope/monitor for X-ray all-sky monitoring of transient and variable X-ray sources. The complex health monitoring system is developed for measuring RHCH properties such as shielding quality, mechanical properties and its evaporation. In case this material is qualified for space use then it can be utilized as a shielding for further nano-satellites or for manned or unmanned structures and habitats.

Acknowledgements

References

[1] Project QB50-The von Karman Institute for Fluid Dynamics. URL https://qb50.eu/.
[2] D. Barnhart, T. Vladimirova, M. Sweeting, Very-small-satellite design for distributed space missions, J. Spacecr. Rockets 44 (6) (2007) 1294–1306, http://dx.doi.org/10.2514/1.28678.
[3] F. Santoni, F. Piergentili, F. Graziani, Broglio Drag Balance for neutral thermosphere density measurement on UNICubeSAT, Adv. Space Res. 45 (5) (2010) 651–660, http://dx.doi.org/10.1016/j.asr.2009.10.001.
[4] D.J. Barnhart, T. Vladimirova, A.M. Baker, M.N. Sweeting, A low-cost femtosatellite to enable distributed space missions, Acta Astronaut. 64 (11–12) (2009) 1123–1143, http://dx.doi.org/10.1016/j.actaastro.2009.01.025.
[5] D. Selva, D. Krejci, A survey and assessment of the capabilities of Cubesats for Earth observation, Acta Astronaut. 74 (2012) 50–68, http://dx.doi.org/10.1016/j.actaastro.2011.12.014.
[6] M. Blazek, P. Pata, A. Inneman, P. Skala, Astronomical tasks for tests of X-ray optics in VZLUSAT-1 nanosatellite, Adv. Astronomy 2017 (2017) 316289, http://dx.doi.org/10.1155/2017/3162892.
[7] B. Rievers, A. Milke, D. Salden, Cubesat in-situ degradation detector (CIDD), Acta Astronaut. 112 (2015) 69–76, http://dx.doi.org/10.1016/j.actaastro.2015.03.015.
[8] T. Berger, M. Hajek, L. Summerer, N. Vana, Y. Akatov, V. Shurshakov, V. Arkhangelsky, Austrian dose measurements onboard space station MIR and the International Space Station overview and comparison, Adv. Space Res. 34 (6) (2004) 1414–1419, http://dx.doi.org/10.1016/j.asr.2003.08.063.
[9] C.J. Poulsen, C. Tabor, J.D. White, Long-term climate forcing by atmospheric oxygen concentrations, Science 348 (6240) (2015) 1238–1241, http://dx.doi.org/10.1126/science.1260670.
[10] L.V. Berkner, L.C. Marshall, On the Origin and Rise of Oxygen Concentration in the Earth's Atmosphere, 1965, http://dx.doi.org/10.1175/1520-0469(1965)022<0225:OTOARO>2.0.CO;2.
[11] M. Durante, L. Manti, Human response to high-background radiation environments on Earth and in space, Adv. Space Res. 42 (6) (2008) 999–1007, http://dx.doi.org/10.1016/j.asr.2007.02.014.

Fig. 13. Volatiles board with double magneto-torquer coil for Z axis.

[12] J. Xiaolin, F. Laiping, R. Hongfei, S. Xiaoyong, Determining orbit of COMPASS-M1 using international laser ranging service data, in: CPGPS 2009: Global Navigation Satellite System: Technology Innovation and Application, Proceedings, 2009.

[13] J.P. Dumont, Jason-2: Product User Handbook, 2011. http://www.altimetry.info/radar-altimetry-tutorial/how-altimetry-works/basic-principle/.

[14] NanoPower P31u/P31us. URL http://gomspace.com/documents/ds/gs-ds-nanopower-p31u-9.1.pdf.

[15] NanoMind A712D.

[16] K. Tsobouchi, Y. Omura, Long-term occurrence probabilities of intense geomagnetic storm events, Space Weather Int. J. Res. Appl. 5(12). doi:10.1029/2007SW000329.

[17] L. Pina, D. Burrows, V. Tichy, W. Cash, D. Cerna, P. Gorenstein, R. Hudec, A. Inneman, J. Jakubek, V. Marsikova, L. Sieger, X-ray monitoring for astrophysical applications, in: Advances in X-Ray/EUV Optics and Components IX, 2014, http://dx.doi.org/10.1117/12.2064726.

[18] S. Barbour, D.A. Erwin, Comparison of focal properties of square-channel and meridional lobster-eye lenses, J. Opt. Soc. Am. A Opt. Image Sci. Vis. 31 (12) (2014) 2584–2592, http://dx.doi.org/10.1364/JOSAA.31.002584.

[19] C. Granja, S. Polansky, Z. Vykydal, S. Pospisil, A. Owens, Z. Kozacek, K. Mellab, M. Simcak, The SATRAM Timepix spacecraft payload in open space on board the Proba-V satellite for wide range radiation monitoring in LEO orbit, Planet. Space Sci. doi:10.1016/j.pss.2016.03.009.

[20] T. Nakazawa, S. Sugawara, G. Inoue, T. Machida, S. Makshyutov, H. Mukai, Aircraft measurements of the concentrations of CO_2, CH_4, N_2O, and CO and the carbon and oxygen isotopic ratios of CO2 in the troposphere over Russia, J. Geophys. Res. Atm. 102 (D3) (1997) 3843–3859, http://dx.doi.org/10.1029/96jd03131.

[21] S. Gorreta, J. Pons-Nin, G. López, E. Figueras, R. Jové-Casulleras, C. Araguz, P. Via, A. Camps, M. Domínguez-Pumar, A CubeSAT payload for in-situ monitoring of pentacene degradation due to atomic oxygen etching in LEO, Acta Astronaut. 126 (2016) 456–462, http://dx.doi.org/10.1016/j.actaastro.2016.06.028.

[22] P. Hana, A. Inneman, V. Daniel, L. Sieger, M. Petru, Mechanical properties of carbon fiber composites for applications in space, in: J. Kovačičinová, T. Vít (Eds.), Optics and Measurement Conference, 2015, p. 94420A, http://dx.doi.org/10.1117/12.2175925.

[23] Z. Chen, C. Lu, Humidity sensors: a review of materials and mechanisms, Sens. Lett. 3 (4) (2005) 274–295, http://dx.doi.org/10.1166/sl.2005.045.

[24] E.-S. Chung, B. Soden, B.J. Sohn, L. Shi, Upper-tropospheric moistening in response to anthropogenic warming, Proc. Natl. Acad. Sci. U. S. A. 111 (32) (2014) 11636–11641, http://dx.doi.org/10.1073/pnas.1409659111.

4.2   Rocket experiment

Two Timepix3 detectors were placed on board the Rocket Experiment as part of the Wide Field X–ray Telescope. This dual payload rocket campaign carried by NASA's Black Brant IX sounding rocket with water recovery technology was accomplished in collaboration with Pennsylvania State University. The Rocked Experiment was launched on 4th April, 2018 from Kwajalein Atoll in the Marshall Islands. The mission was designed to classify the TRL of on-board equipment designed for space applications. The observation target was the Vela supernova remnant, an X–ray source. The dual X–ray telescope consists of one one-dimensional and one two-dimensional Loster-Eye reflective optics combined with the Timepix detector. Since a significant effect of background radiation on the measured data was expected, the possibility of filtering this radiation was successfully tested in a verification measurement with a weak ^{55}Fe source in a vacuum tunnel (see Figure 4.11).

| (a) raw image | (b) filtered image | (c) energy spectrum |
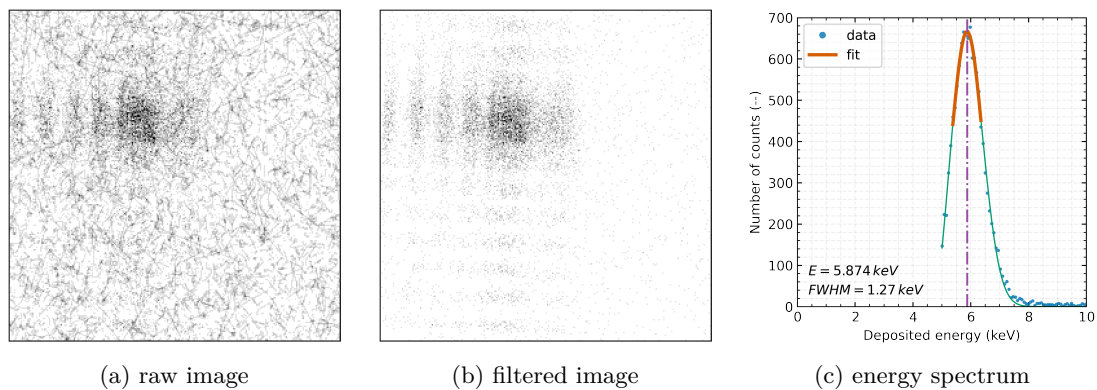
Fig. 4.11: Test of the X–ray telescope in a vacuum tunnel with a weak radiation source ^{55}Fe and long exposure time. The X–ray telescope combines a Timepix detector with a two-dimensional Lobster-Eye optic. The images show the out-of-focus test of the telescope during a measurement time of almost 17 h and the energy spectrum of the detected radiation from the same data/measurements. The background radiation was a significant contributor to the resulting image. Both raw and one-pixel filtered data are shown.

Unfortunately, the focus of both telescopes could not be verified due to the low intensity of the space X–ray source and the short observation time. As all instruments were in operation throughout the flight, valuable data were obtained to verify the technologies. In addition, certain scientific data were obtained, including the monitoring of thermal cycles spanning from 30 °C to 45 °C. In view of the previous findings, these temperature fluctuations may also have an influence on the accuracy of the energy measurements. It is, therefore, appropriate to apply the new methods presented in section 3.3 also in the context of this type of short rocket mission.

M. Urban, O. Nentvich, T. Báča, I. Veřtát, V. Maršíková, D. Doubravová, V. Dániel, *et al.*, "REX: X-ray experiment on the water recovery rockets," *Acta Astronautica*, vol. 184, pp. 1–10, Jul. 2021. DOI: `10.1016/j.actaastro.2021.03.019`
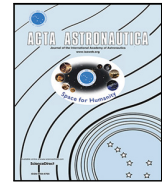
Research paper

REX: X-ray experiment on the water recovery rocket

Martin Urban [a,*], Ondřej Nentvich [a], Tomáš Báča [a], Ivo Veřtát [b], Veronika Maršíková [c],
Daniela Doubravová [c,d], Vladimír Dániel [e], Adolf Inneman [a,c], Ladislav Pína [a,c], Ladislav Sieger [a],
Randall L. McEntaffer [f], Ted B. Schultz [f], Drew M. Miles [f], James H. Tutt [f]

[a] *Czech Technical University in Prague, Czech Republic*
[b] *University of West Bohemia, Pilsen, Czech Republic*
[c] *Rigaku Innovative Technologies Europe, s.r.o., Prague, Czech Republic*
[d] *Advacam, s.r.o., Prague, Czech Republic*
[e] *Czech Aerospace Research Centre a.s., Prague, Czech Republic*
[f] *Pennsylvania State University, State College, PA, USA*

ARTICLE INFO

ABSTRACT

This paper presents Rocket Experiment (REX) that was part of a dual-payload rocket campaign for NASA's sounding rocket Black Brant IX with water recovery technology. This mission was a suborbital sounding rocket flight that was launched and recovered on April 4, 2018 and targeted the Vela supernova remnant. The purpose of REX was to classify the Technology Readiness Level of onboard devices designed for space applications. The devices were two wide-field X-ray telescopes consisting of a combination of Lobster-Eye (LE) optics with an uncooled Timepix detector ($256\,\text{px} \times 256\,\text{px}$ @ $55\,\mu\text{m}$), and additional sensors. The first telescope uses a two-dimensional combination of LE modules with a focal length of $1\,\text{m}$ and a Field of View (FOV) of $1.0° \times 1.2°$ and operates in the energy range of $3-60\,\text{keV}$. The second telescope was a one-dimensional LE with a focal length of $243\,\text{mm}$ and a FOV of $2.7° \times 8.0°$ for the energy range $3-40\,\text{keV}$. The X-ray telescopes were supplemented by a camera in the visible spectrum with $1.280\,\text{px} \times 1,024\,\text{px}$ resolution, which was used to obtain images of the observed sources and to verify the resulting pointing of the rocket carrier. Other devices also include infrared array sensors and inertial measurement units tested for future small satellite missions. The data handler and communication system were built using the Robot Operating System, and both the system and the electronics were deployed and operated in-flight. The hardware was successfully recovered after the launch and the data were extracted.

1. Introduction

Sounding rockets, a type of suborbital rockets, provide a low-cost observing platform for carrying instruments for scientific and educational purposes, as well as for rapid technology validation. The suborbital flights do not reach orbital velocity, therefore, can be smaller in size and less expensive in design. Thus, several systems like motors and telemetry systems can be cheaper, as can shields against harsh environments. Therefore, the price of the launch is lower than for satellite missions. One of the main disadvantages of using suborbital rockets is in the limited experiment time, which is usually $2-20\,\text{min}$. Nevertheless, they are still useful for verification of technologies in space which do not require a long experimental time. A major consideration for the Technology Readiness Level (TRL) of devices used in space is not only the capability of working under vacuum, extreme temperatures, temperature changes, and radiation, but also the ability to survive the violent conditions during launch and booster separation [1].

Several research centers around the world conduct sounding rocket experiments, e.g. the Wallops Flight Facility in Virginia (NASA), and the Esrange Space Center in Sweden (ESA). The sounding rocket can be used for the already mentioned verification or as a technological demonstrator of individual instruments and entire rocket carrier [2], but also for scientific missions or educational purposes. The combinations of these categories are possible as well.

As an example of geospace scientific missions can be mentioned the CHAMPS mission [3]. This mission consisted of two rockets which were used to measure the density and size distribution of meteoritic

(a) At the launch site.

(b) During the launch.

(c) Recovery at sea.

Fig. 1. Rocket carrier and its launch from Kwajalein Atoll in the Marshall Islands.

(a) The sensor and optic compartment of the rocket payload.

(b) Apertures at the front of the REX instrument.

Fig. 2. The final arrangement of the rocket vacuum segment with REX payload (1D and 2D LE telescopes) and WRXR payload (soft X-ray spectroscope).

smoke particles in the upper atmosphere. Another one is the HERSCHEL payload which was focused on the solar science and on the examination of the Sun's atmosphere [4]. Its goal was the research of the helium amount and how the solar wind originated and accelerated.

From the last category, education missions, a series of projects like *RockOn!*[1] and *REXUS*[2] can be mentioned. These programs are designed for students to learn and apply skills in building experiments for suborbital space flight and test their final design.

The suborbital mission described in this manuscript was a two-payload campaign carried by the NASA's sounding rocket with water recovery technology for science payloads, which was launched from the Kwajalein Atoll in the Marshall Islands on April 4, 2018. Fig. 1 shows photos from the launch and recovery dates.

The observation of the Vela Supernova Remnant (SNR) was the primary scientific astrophysical target of this sub-orbital experiment. The Vela SNR is a shell-type remnant located in the southern constellation Vela at a distance of approx. 250 pc [5]. This source is Type II and it exploded approximately 11,000–12,300 years ago. The center of the Vela SNR is formed by a neutron star with a strong magnetic field, with a mass close to our Sun and a diameter of approx. 20 km [6] (the apparent diameter of $\approx 8°$). Due to the apparent size of the object and high surface brightness [7], this SNR is a frequent source of observation and testing of equipment for both sounding rockets and space telescopes [8–11]. In addition to scientific observation, the mission aims at an important technological goal, namely the suborbital flight verification of scientific payloads.

Payloads for this rocket mission were prepared in cooperation with Pennsylvania State University (PSU) which was chosen with its main measuring instrument — a soft X-ray grating spectrometer (bandpass 0.25–0.75 keV) named the Water Recovery X-ray Rocket (WRXR) payload. The spectrometer consisted of a mechanical collimator, X-ray reflection gratings, grazing incidence mirrors, and a hybrid CMOS detector. In-depth description of the mission goals and the WRXR payload can be found in [12–15].

The second payload – the REX – was prepared by the Czech team and contained two sets of Multi-Foil Optics (MFO) in combination with the Timepix detector [16], which formed two separate X-ray telescopes. The first of the REX telescopes consists of two LE modules in the Schmid's arrangement [17,18] which covered a FOV of 1.0° × 1.22° in the energy range of 3–60 keV. The second telescope has a single one-dimensional (1D) LE module [19] with a field of view of 2.75° × 8.0° for the energy range 3–40 keV. Moreover, the payload was equipped with additional sensors: *Ximea* camera for visible spectrum with the resolution of 1,280 px × 1,024 px, an IR sensor array, and an Inertial Measurement Unit (IMU). A photo of the payload is shown in Fig. 2a with the WRXR on the top and the REX on the bottom.
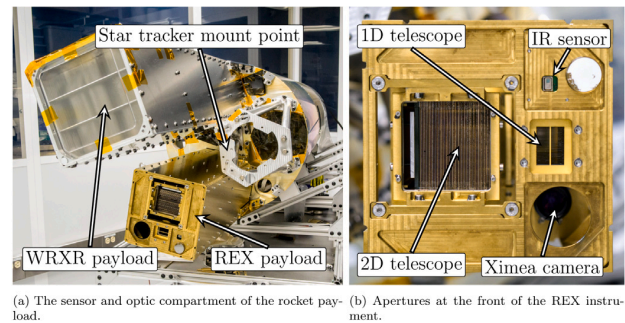
2. REX instrument description

The REX payload consisted of two main parts: the optics modules including sensors, and a hermetically sealed electronics box. An airtight bulkhead separated both parts and they were electrically connected via a vacuum feedthrough. The payload was also connected to a rocket interface panel via another vacuum feedthrough.

The optics and sensors section contained all sensors and detectors except for the IMU, which was placed in the hermetic box. The hermetic box was placed behind the air-tight valve in the bottom part of the rocket. The sensor section was designed as hermetically sealed to hold an artificial low-pressure atmosphere to prevent liquid condensation during launch. The visible-light camera was used alongside the X-ray telescopes as well as the IR sensor array. A carbon-fiber baffle covered the optical path between the optic modules and Timepix detectors to avoid side rays. A schematic of the optical system in the vacuum part of the rocket is shown in Fig. 3.
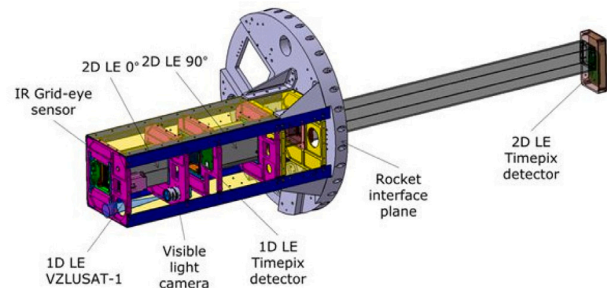
Fig. 3. 3D rendition of the vacuum part of the X-ray optical system REX.

The hermetic box contained NiCd batteries and switching power supply electronics with DC/DC converters for powering the devices during the entire duration of the experiment (approx. 2 h). Two on-board Odroid-XU4 ARM computers managed the sensors and miscellaneous electronics provided an interface with the rocket. Each of the computers controlled a single Timepix detector (one per telescope), and the rest of the sensors were evenly distributed between the computers. Mission software using Robot Operating System (ROS)[3] was developed to operate and control the entire experiment. ROS is a widely adopted open-source middleware for the integration of sensors and data processing algorithms for autonomous systems. Simultaneously, an operating interface for Timepix detectors in ROS was developed under the name *Rospix*[4] [20].

---

[1] https://spacegrant.colorado.edu/national-programs/rockon-home.
[2] http://rexusbexus.net.
[3] http://ros.org.
[4] http://github.com/rospix/rospix.

2

Fig. 4. An illustration of the arrangement of the 2D optical system. Two 1D modules were combined in series with 90° mutual rotation along their optical axes.

Fig. 5. Dependence of reflectivity on emitting energy for several angles of incidence, namely 0.10°, 0.25°, 0.50° and 1.00°. Golden surface material was used for mirrors with microroughness 0.2 nm. Data are based on online X-ray library CXRO.[5]

2.1. X-ray telescope based on Lobster-Eye optics and Timepix detector

The REX experiment consisted of two LE telescopes designed by Czech Technical University in Prague (CTU), manufactured by Rigaku Innovative Technologies (RITE), a two-dimensional (2D) in Schmidt's arrangement and a 1D Lobster-Eye optics. Table 1 presents all the parameters of the optics: the coating of the mirror layers, the focal length or FOV and the physical position of the module in the experiment. The 1D LE optics has the same parameters as an identical copy used in our previous successful mission on the nanosatellite VZLUSAT-1 [21, 22].

Table 1
Parameters of the 1D and 2D Lobster-Eye optics for rocket experiment.

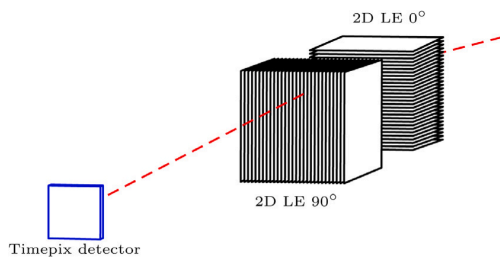|	1D	2D
Module center position (horizontal)	250 mm	1,363 mm
Module center position (vertical)	–	1,097 mm
Focal length (horizontal)	243 mm	1,345 mm
Focal length (vertical)	–	1,079 mm
Field of view (horizontal)	2.75°	1.04°
Field of view (vertical)	≈ 8°	1.29°
(limited by housing)		
Mirror thickness	0.145 mm	0.35 mm
Mirror spacing	0.3 mm	0.75 mm
Mirror dimension	60 × 25 mm²	150 × 75 mm²
Number of mirrors	56	2 × 47
Reflective surface	Au	Au
Angular resolution (horizontal)	6.12 arcmin	1.40 arcmin
Angular resolution (vertical)	–	1.59 arcmin

The position of both 1D and 2D telescopes are visualized in Fig. 3. The 2D telescope contained two 1D optical modules placed in series. The modules were mutually rotated by 90° along their optical axes to form a 2D optical system. Fig. 4 shows an illustration of the 2D system configuration. A Timepix detector was placed 1,438 mm from the front aperture in the focal plane of the 2D system. The 1D telescope was placed alongside the 2D, with another Timepix detector in the focal plane. The focal distance of the 1D was 243 mm and the system contains only one optical module and thus the values for vertical dimension are void.

The intended wide-field Lobster-Eye optics were designed for a telescope which can achieve a wide Field of View. The used mirrors were designed to have at least 50 % of total reflectivity, which is 50 % for a single reflection (1D module) or 70 % for double reflection (2D telescope). For both 1D and 2D optics the limit angle is approx. 0.25° and this condition is valid for a spectral range up to 17.7 keV for the 1D telescope according to Fig. 5. For 2D telescope and double reflection the spectral range is only up to 13.5 keV.

The LE optics were planned to use in combination with the visible camera (described in the chapter 2.2) to verify the star constellation in the Vela remnant. All telescopes were pointed to the same position in the sky. We expected to get several line focuses from the 1D Lobster-Eye optics and crosses from the 2D Lobster-Eye.
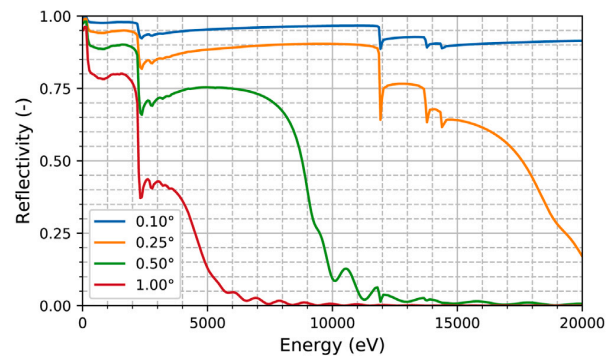
This REX mission carried both 1D and 2D LE telescopes to verify their TRL and based on the results, we will decide which telescope will be suitable for the next mission and which not. If the 1D telescope will pass it can be used for our other goal which is to develop a system for determining the position of point sources based on two 1D LE optics. This combination should have better efficiency for incoming radiation and lower attenuation as was proposed in [23].

2.1.1. Simulating the optical systems

The Vela nebula produces a flux of $3.0 \cdot 10^{-11} \text{ erg cm}^{-2} \text{ s}^{-1}$ in the energy range of $4-25 \text{ keV}$ [24] to the input aperture of each optic. For example, the Point Spread Function (PSF) can be used with a combination of two 1D Lobster-Eye optics for higher efficiency of the telescope, which leads to higher photon flux on the detector and thus in combination with a coded mask leads to a faster identification of events in the sky as is proposed in [23]. Figs. 6 and 7 show simulated results of detector images where the optics have 100 % reflectivity and the detector 100 % quantum efficiency.

2.1.2. Timepix detector

The Timepix detector [16] was used as an X-ray detector for the REX experiment. This hybrid silicon pixel detector developed at CERN consisted of a high-density matrix of 256×256 sensitive pixels with a pixel pitch of 55 μm, and the total sensitive area of the detector was $14.1 \times 14.1 \text{ mm}^2$. The Timepix sensor (see Fig. 8) consists of two parts: the first part is the semiconductor detection layer (300 μm silicon in this case used for the energy range of $3-60 \text{ keV}$), which is bump bonded to the second part, an Application-Specific Integrated Circuit (ASIC) readout chip containing preamplifier, Analog-to-Digital Converter (ADC), and a counter for each pixel. Data from the sensor can be read out as fast as 100 images per second (depending on the accompanying hardware interface [25–28]), which makes it ideal for particle tracking applications. On the other hand, long acquisition times on the order of minutes are possible, thanks to the sensor's noise-less output. The matrix of all 65,535 pixels can be equalized for a given energy threshold which makes the sensor filter out events with lower energy than the threshold. Thus it is possible to record even single-photon events while measuring their energy.

Timepix has already been extensively tested in space [29], e.g. onboard the International Space Station [30,31], the Proba-V satellite [32], CubeSat VZLUSAT-1 [22,33,34], TechDemoSat-1 [35,36], and RISESAT [37]. Two spare detectors from the RISESAT project were used for the REX payload.

---

[5] https://henke.lbl.gov/optical_constants/layer2.html.

(a) Simulating high flux.

(b) Simulating expected flux.
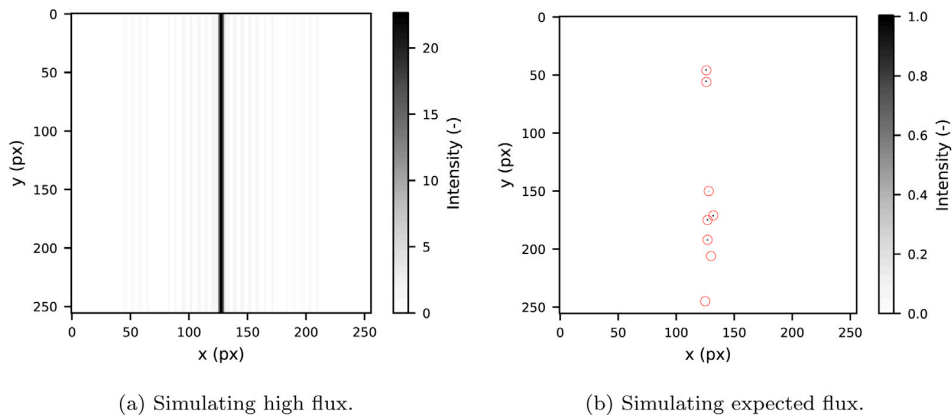
Fig. 6. (a) Simulated image with 100% mirror reflectivity for an energy of 8 keV and a uniform distribution of the photons on the input aperture and (b) calculated photons, which are encircled, during the observation time (282.5 s). Both (a) and (b) images use 1D Lobster-Eye optics with parameters listed in Table 1.

(a) Simulating high flux.

(b) Simulating expected flux.
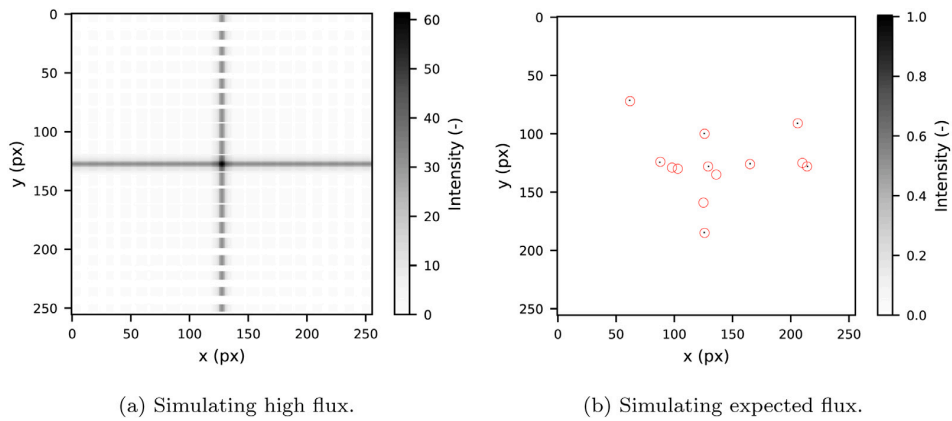
Fig. 7. (a) Simulated image with 100% mirror reflectivity for an energy of 8 keV and a uniform distribution of the photons on the input aperture and (b) calculated photons, which are encircled, during the observation time (282.5 s). Both (a) and (b) images use 2D Lobster-Eye optics with parameters listed in Table 1.

(a) Timepix sensor with Si detector.

(b) An image of particle tracks.
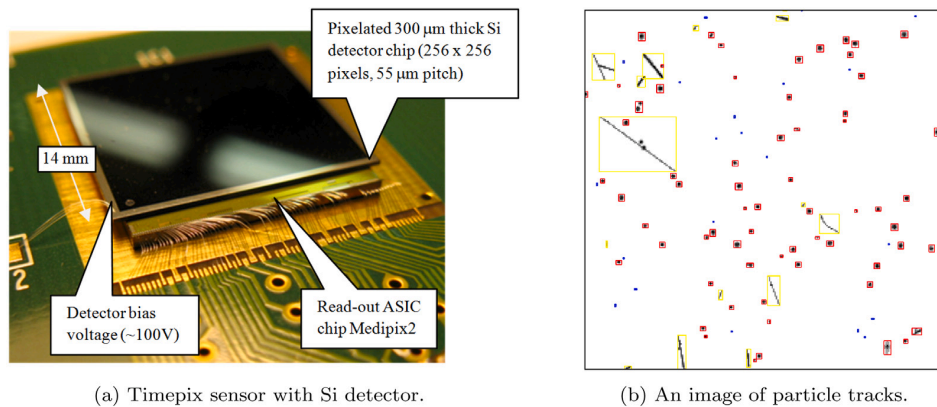
Fig. 8. Timepix (a) sensor consists of a 300 μm Si detector and an ASIC read-out chip. The sensor produces images with 256 × 256 px resolution. (b) Ionizing particles leave characteristic marks (yellow — electrons/muons, red — ions, blue — gamma), which can be processed by machine learning algorithms [20] to extract the particle type and its energy. (For interpretation of the references to color in this figure legend, the reader is referred to the web version of this article.)

2.2. Camera for the visible spectrum

The camera system for the visible spectrum was employed to verify the REX's target pointing in addition to the primary Attitude Determination and Control System (ADCS) of Black Brant IX rocket. Verification of the small, cheap, and uncooled industrial class CMOS camera was the secondary purpose of this system, as it is considered for the future CubeSat missions. The camera system was based on the Ximea MQ013CG-E2 module with a small size (26 × 26 × 26 mm³) and low weight (26 g). The camera has a 1/1.8" CMOS sensor with 1.3 Mpx

(a) Ximea camera. (b) ThorLabs lens.
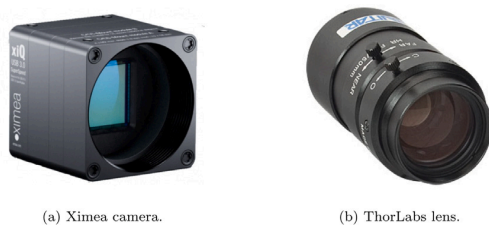
Fig. 9. Small CMOS camera module from Ximea with ThorLabs lens, used in the REX experiment as star tracker.

native resolution. The camera module was equipped with ThorLabs MVL50M23 lens, with a focal length of $50\,mm$, offering a field of view approximately 9.8°. Fig. 9 shows the camera module and the used lens. The low power consumption and the aluminum camera case attached to the massive rocket mechanical structure mitigated the possibility of the camera overheating in vacuum. An absence of plastic materials in the camera body avoided the pollution of the telescopes by material outgassing. The USB3 interface and the availability of drivers for the ROS made it easier to implement the camera control software in the Odroid on-board computer. The camera outputs uncompressed RAW images which allow post-processing of captured images after the rocket's recovery.

2.3. Additional sensors

The infrared array sensor *Grid-EYE* AMG88 ($8\,px \times 8\,px$ resolution) was added to the REX payload as a technology demonstrator of Earth horizon detection. It could be used as one of the inputs to ADCS algorithms of a small CubeSat satellites. Furthermore, we employed an off-the-shelf IMU, the MPU6000. It is a miniature low cost 3-axis Micro-electro-mechanical System (MEMS) accelerometer and gyroscope, widely used in commercial electronics and robotics.

As this class of electronics is not dedicated for space application, the main reason for using it in this mission was to test the capability of the sensor to survive the hard conditions of the rocket launch. The possibility of its future usage for recognition of flight phases and experiments triggering as well as future usage in attitude determination and control systems of small satellites will be examined.

3. Experimental results

3.1. Launch event and payload recovery

The Water Recovery X-ray Rocket was launched on April 4, 2018 from the Kwajalein Atoll in the Marshall Islands. Fig. 1 shows the rocket before, during and after the launch. The total experiment time was $919\,s$ with $282.5\,s$ while pointing on target. Both telescopes survived the launch, observation and impact when the rocket landed on the water. A damage to the rocket fuselage was caused during descend by uneven heat dissipation. However, despite a breach of the electronics compartment has caused a water leakage on our hermetic electronics box, the electronics inside of the box survived and data were recovered.

Analysis of the data shown that the internal pressure in the optics compartment has temporarily spiked during the launch [15]. This was presumably caused by a water vapor outgassing. The optics and electronics section of the payload were supposed to be isolated according to the original flight plan and the optics compartment was planned to be pumped out to high vacuum. Instead, the both sections were connected due to a last-moment failure of the ion pump for the optics section. It is suspected that water from the payload skins caused a rise in the compartment pressure [15] and could later condensed and formed ice on the instrumentation.

The goal of this mission was to verify the TRL of the devices which successfully worked during the REX mission.
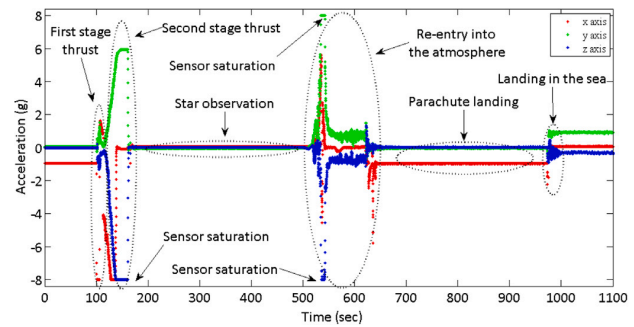
Fig. 10. Data from the onboard 3-axis MEMS accelerometer with recognized and marked key phases of the suborbital mission.

3.2. Inertial measurement unit

The recorded data show consistent values from the beginning of the mission until the rocket parachute landed into the ocean and stayed floating in the water. All of these facts indicate that the sensor survived the mission. The main phases of the flight are labeled in Fig. 10, and it shows the thrust phase of the first and the second rocket engine stage, fast rocket detumbling before observation of stars, zero gravity observing phase, reentry into the atmosphere, parachute descending, impact onto the water surface and free floating in water. The MPU6000 sensor was partly in saturation during the full engine thrust due to its higher sensitivity setting, but it survived an acceleration of almost $13.7\,g$ and an angular velocity of more than $3,000\,deg/s$. The achieved results are promising and, therefore, the MPU6000 will be used in the future mission of PilsenCUBE II satellite.

3.3. Visible camera and payload pointing

Reliable recognition of low brightness stars in the image required long exposure time and high gain of the image sensor due to its small pixel pitch. However, these parameters also increase the dark current and thermal noise which lead to the degradation of images, especially when the image sensor has a higher temperature. Since many aspects of the suborbital mission were not known during the payload preparation, we did not have simulations of the expected camera heating. We proposed a special camera capture mode with changing exposure settings in the loop and with idle intervals between the individual batches of image frames to overcome this issue of thermal uncertainty. The capture mode started recording a batch of image frames as soon as the rocket electronics were switched on shortly before the launch. Each batch of image frames consists of several different combinations
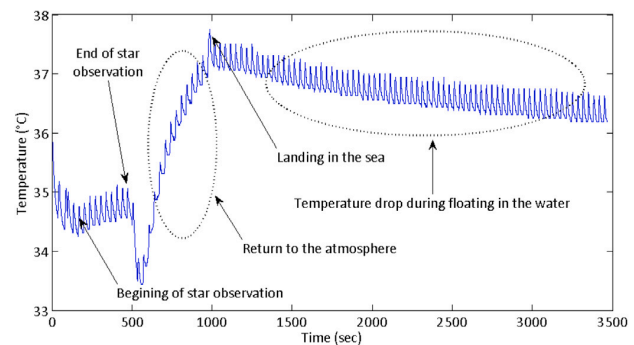
Fig. 11. Logged temperature profile of camera system during the whole mission.
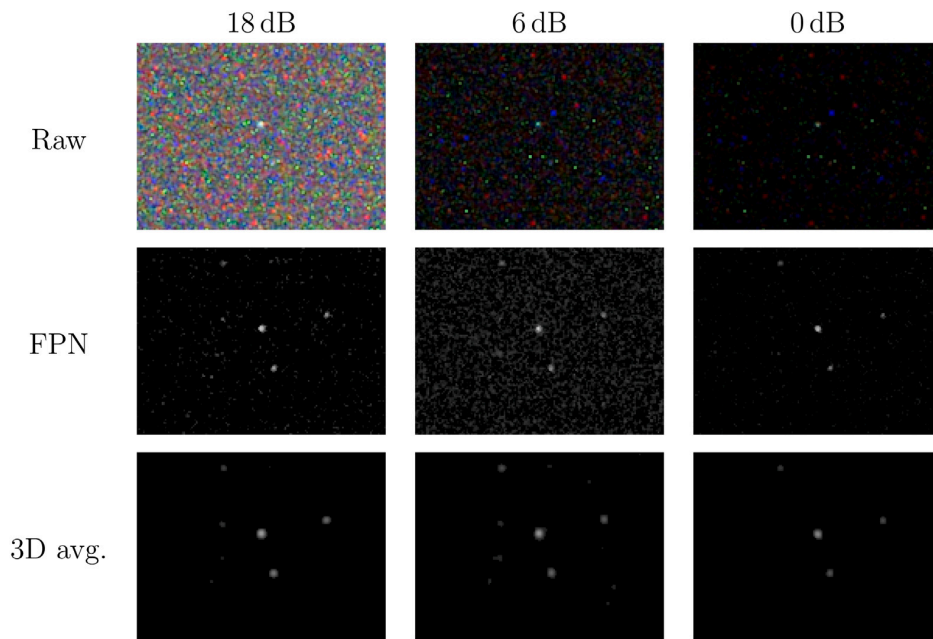
Fig. 12. Cutout of the captured images with the exposure time 500 ms. Images with different gains (18 dB, 6 dB and 0 dB) are shown in columns. First row (Raw) shows raw images captured during the sub-orbital flight. Second row (FPN) shows same cutouts after Fixed-pattern noise suppression by the subtraction of the dark images. The last row (3D avg.) represents results after applying a spatial and temporal averaging 3D filter.

of exposure time settings (from 100 ms up to 900 ms) and sensor gain settings (from 0 dB up to 18 dB). The low power mode was inserted for a short time between two batches to reduce heating of the camera. Several different exposure settings minimized the risk of inappropriate camera settings due to unforeseen temperature conditions and could also be used for the combination of images during the post-processing.

Camera temperature was almost constant near 34.7 °C during the observation part of the mission, as shown in Fig. 11. Small periodical increases and decreases of camera temperature were caused by the low power mode being switched on between batches of images to avoid overheating. However, the main temperature envelope was given

by the temperature of mechanical structures in the rocket and their changes during ascending, observation, descending and the landing phase of the mission.

The first row in Fig. 12 represents a sample of original images captured during the suborbital flight, which were strongly affected by fixed pattern noise and thermal noise. Only a few of the brightest stars can be recognized, but not clearly due to strong noise artifacts in the images.

Most of the fixed pattern noise was removed by the dark image subtraction, because it is almost constant for given exposure settings and camera temperature. Dark images were captured for all exposure
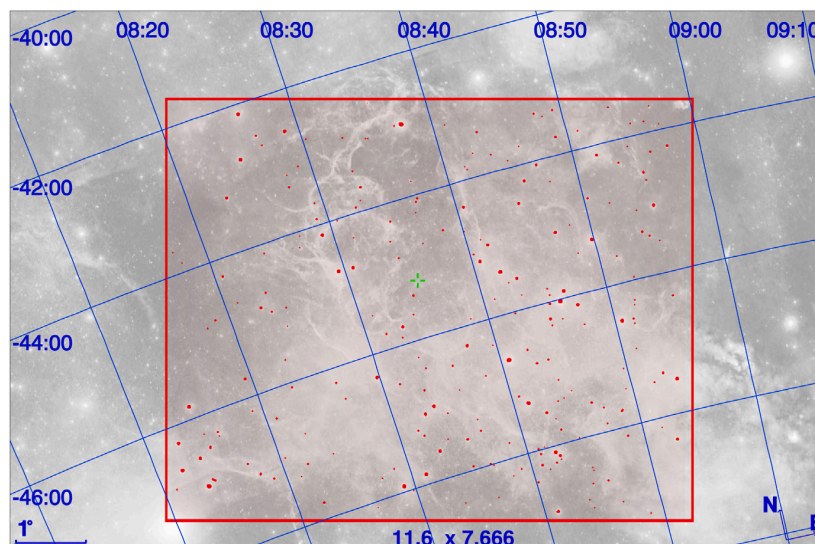
Fig. 13. Background image from DDS-II colored catalogue overlayed by our image with 500 ms exposure and 0 dB gain, after stacking and noise filtering process. Stars from our image are colored to red, red border marks Field of View, green reticle marks the position of the Vela Pulsar. (For interpretation of the references to color in this figure legend, the reader is referred to the web version of this article.)

settings when the rocket was in the ascending and descending phase of the mission in a closed instrumentation section. Results of dark image compensation are shown in the second row of Fig. 12. Nonlinear amplification and thresholding were also applied to increase the image clarity. Due to the gradual acquisition of dark images, there is no uniform representation for all combinations of camera settings and thermal fluctuations. Therefore, fixed pattern noise could not be completely suppressed, in some cases, as can be noticed in the exposition with the 6 dB gain.

Bright stars can be well recognized after removing the Fixed-pattern noise (FPN) artifacts, however the high amount of thermal noise is still present in the images, covering and masking the weak stars. The thermal noise was additionally suppressed by applying a spatial and temporal averaging filter on the series of images captured during the attitude stabilized phase of star observation. The results of averaging eight images in series and spatial averaging with 3×3 neighboring pixels are shown in the last row of the of Fig. 12.

Most of the thermal noise was suppressed by averaging filters and this enabled less bright stars to be recognized (apparent magnitude 8). Some residual fixed pattern and thermal noise is still present in the images, but stars can be successfully identified. A comparison of the processed image with the Digitized Sky Survey II (DDS-II)[6] catalogue map shows in Fig. 13.

The small and cheap camera successfully fulfilled the task in the suborbital mission and confirmed the targeting of the X-ray telescopes. Use of these cameras in small satellites like CubeSat requires capturing a dark image and having a long exposure time (which requires attitude stabilization).

3.4. Infrared sensor array

Unfortunately, the timing of the rocket stabilization and door opening and closing in the scientific section did not show the Earth to the FOV of the Grid-EYE sensor, but valuable data were nevertheless obtained. As this and similar IR arrays contain IR lenses, sensors should not have to experience high acceleration and the conditions during rocket launch are far behind the recommended operation limits.

However, the thermal image had sharp edges during the observation part of the mission so it indicates that the IR lenses survived the launch conditions. Whether the IR lenses also survived the conditions of the rocket's descent into the atmosphere cannot be stated with certainty because the implementation team had not the possibility to perform after flight laboratory tests of the sensor. During the descent, however, the sensor still showed reliable data, comparable to the thermal image during the ascending phase of flight.

During the ascending and descending phase of the mission, the sensor's FOV was the door and the mechanical structure of the rocket. The thermal data from the sensor (Fig. 14) indicated the heating of the inner rocket structure from the initial $25 - 30\,°C$ up to $80\,°C$, due to friction of the atmosphere during the ascending phase, followed by a fast decrease of temperature down to $-150\,°C$ (post-processed value), after the door opening for the phase of star observation. Closing the science section door and reentry into the atmosphere caused a short increase of temperature of the inner mechanical structure, followed by cooling during its slow parachute descent and landing into the ocean.

The most interesting data were expected after opening the science section and subsequent exposure of the sensor to the absence of heat from space, and to the heat of the rocket structure, both concurrently in the FOV of the sensor, where the sensor is exposed to a high dynamic range of measured temperatures. However, the sensor suffered from a software overflow or sensitivity switching in this situation and the sensor's pixels shift numeric representation of temperatures approximately one half of the numeric range, which leads to a false

6 https://archive.eso.org/dss/dss.
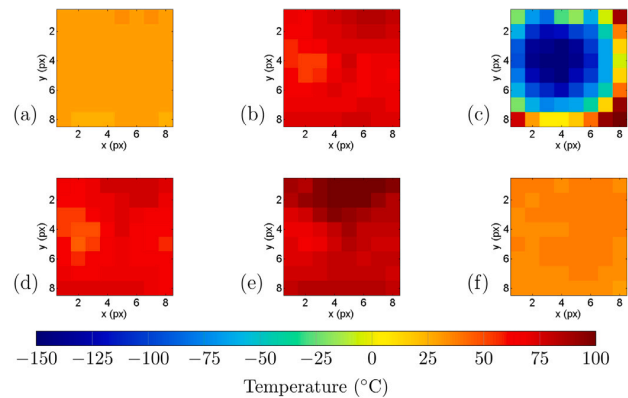
Fig. 14. Obtained thermal images from the AMG88 IR sensor; (a) before launch, (b) during ascending, (c) after science section door opening, (d) after science section door closing, (e) during descending, and (f) after landing.

interpretation of the measured temperatures from two complement binary representation. This can be seen in Fig. 15, where the readout temperature of the pixels alternates between high temperature and low temperature.
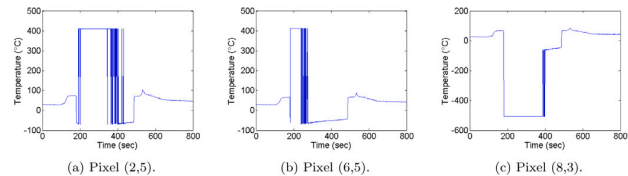
Fig. 15. Examples of acquired temperature measurements affected by a software overflow in numerical expression of temperatures; (a) in pixel position (2,5), (b) in pixel position (6,5), (c) in pixel position (8,3).

The overflow behavior was compensated in post-processing based on the numeric range of the temperature oscillations and knowing the expected temperature values for specific locations of the rocket structure in the sensor FOV. Compensated temperatures with the opened scientific section are shown in Fig. 16 as the mean value of four pixels in the middle of the AMG88 Grid-EYE sensor.

The tested IR array sensor AMG88 is usable for simple and non-critical application in similar missions, even with the instability of numeric representation of temperatures. The temperature changes in the FOV are detectable, only the absolute value of temperature is unreliable. The sensor can be used, for example, as a simple detector for the release of the deployable parts, covering the sensor in the stowed state and opening the sensor FOV to space in the deployed state. Using
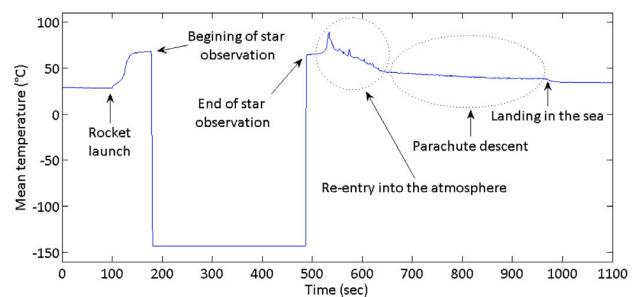
Fig. 16. Temperature in the Field of View after compensation of numeric representation overflow — plotted as mean value of four central pixels.

this sensor as an Earth horizon detector in the ADCS of small satellites is not suitable with this particular sensor due to its instability of numeric representation of temperatures.

3.5. X-ray telescopes

Both X-ray detectors were autonomously operated by a custom-built software [20] in ROS. Data from both detectors were acquired using as a continuous stream of $1\,\mathrm{s}$ acquisitions that started before launch.

(a) 1D LE integral image.

(b) 2D LE integral image.
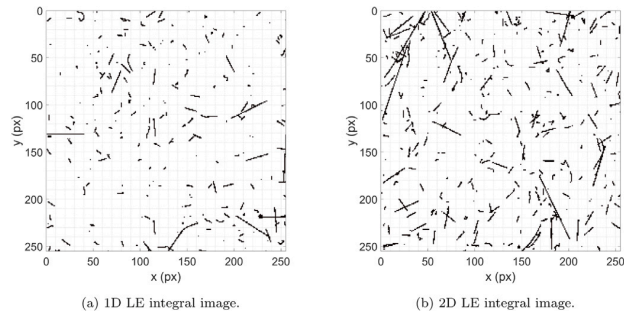
Fig. 17. Integral image during the entire duration rocket's flight; (a) 1D LE telescope, (b) 2D LE telescope.

Both X-ray telescopes (1D and 2D) took images during the entire duration of the rocket's flight (Fig. 17). Figs. 18a, and 19a represent filtered integral images from both telescopes while the rocket pointing at the Vela pulsar. Thanks to the data sensing system, it was possible to recognize and filter out individual events based on the size of their tracks or their dissipated energy in the detection layer. The results of track size classification are shown in color. The main areas of interest were gamma particles (photons with a range of energies between $3\,\mathrm{keV}$

(a) Integral image.

(b) Row sums.

(c) Column sums.

(d) Cluster size histogram.

Fig. 18. Data obtained from the 1D telescope taken while pointing at the Vela pulsar: (a) integral images with particle tracks labeled according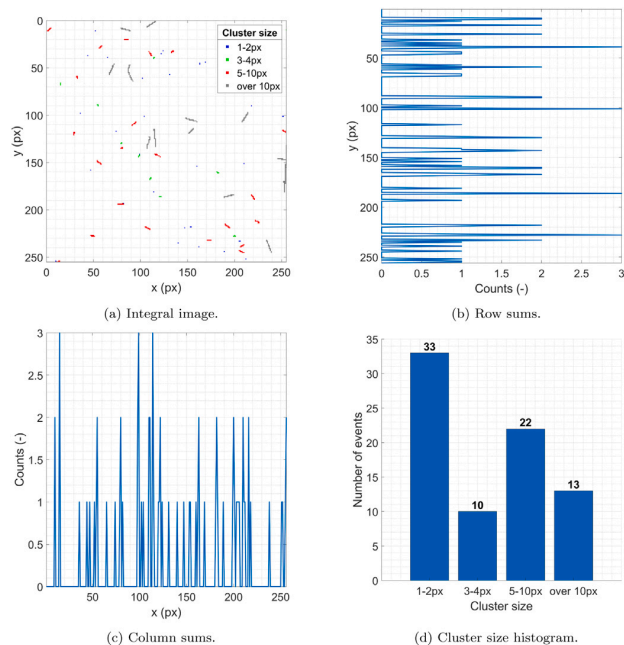 to their size (b) profile of summation of image rows $(1-4\,\mathrm{px})$ (c) profile of the summation of image columns $(1-4\,\mathrm{px})$ (d) bar graph representing the frequency of events according to their size.

(a) Integral image.

(b) Row sums.

(c) Column sums.

(d) Cluster size histogram.
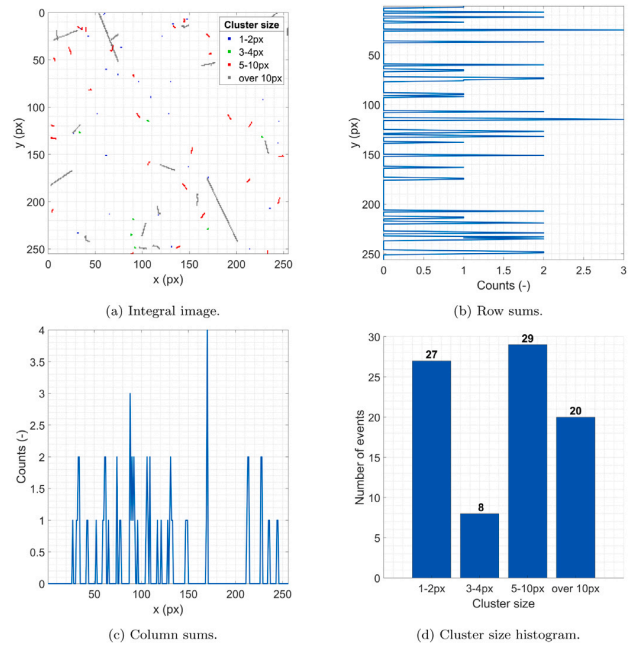
Fig. 19. Data obtained from the 2D telescope taken during the pointing time: (a) integral images with tracks labeled according to their size (b) profile of row summation of the image $(1-4\,\mathrm{px})$ (c) profile of the column summation of the image $(1-4\,\mathrm{px})$ (d) bar graph representing the frequency of events according to their size.

to $10\,\mathrm{keV}$), which in the case of the Si detector, leave mostly single-pixel events on the detector [38]. However, photons can strike multiple pixels due to charge-sharing among the neighboring pixels. During the evaluation of the measurement, we considered $1-4\,\mathrm{px}$ events as gamma photons.

The filtered images, formed only by impacts of gamma particles, were evaluated as horizontal and vertical projections. Sums of individual rows and columns were plotted as a line graphs, which effectively produces integral images of 256 line-detectors. This technique makes it easier to detect the position the focus line (1D) and cross (2D), since the focus is always aligned with the detector rows and columns. Fig. 18 shows the processed and filter data from the 1D telescope, Fig. 19 depicts the data from the 2D telescope.

As it can be seen in the images, a small number of particles was collected on both detectors. Despite the approx. 43 (1D) respectively 35 (2D) X-ray gamma events taken during the observation time, no apparent focal point/line or preferential event positions was observed. The total supposed X-ray counts during the whole observation were 5 photons for the 1D optics and 27 photons for the 2D optics. The results show no statistical tendency to form a focus line by the 1D telescope or focus point by the 2D telescope. In fact, majority of the measured signal originates from ambient background radiation, which was recorded equally by both detectors.

Another reasons for such a small photon count yield might be a water condensation on the optics surfaces, as suggested by [15]. Water vapor condensing on the surfaces of the LE optics foils would diminish the intensity, especially for soft X-rays. However, the real reason is unclear as not enough data supports this hypothesis for the REX payload. Importantly for the TRL evaluation, both the optics and the electronics have survived the experiment and all the subsystems were fully operational from the point of view detectors, sensors and software equipment.

4. Conclusion

The Rocket Experiment was one of two payloads on the suborbital rocket campaign launched from the Marshall Islands on April 4, 2018. The mission goal was to demonstrate the space performance of X-ray multifoil telescopes in combination with an uncooled pixel detector Timepix and the verification of the Technology Readiness Level. The payload contained a number of other sensors and devices, for observation in the visible, infrared, and X-ray spectra. The payload system was operated by the custom-made automatic software Rospix, developed specifically for this experiment which was subsequently published for free use by the general public and scientists. Due to the low intensity of the source, the measurements did not yield sufficient results for X-ray observations of the Vela Supernova Remnant. However, we can report that all instruments in the proposed system worked successfully and without problems during the experiment except the LE optics for which we cannot commit to their full functionality, due to low photon flux. Based on the obtained results, the functionality and the possibility of using the proposed system for similar upcoming experiments was confirmed. All devices used onboard the Rocket Experiment have in most cases proved their functionality at the Technology Readiness Level 7 (Tested in real environment). Unfortunately, several tests and many paperwork are still missing to obtain an official rating according to ESA standards (ECSS). However, based on this mission's results, some devices are used on or updated for the CubeSat VZLUSAT-2 (X-ray optical system, visible camera chip) or are planned for another mission PilsenCUBE II (IR, IMU) and rocket experiments REX II.

Declaration of competing interest

The authors declare that they have no known competing financial interests or personal relationships that could have appeared to influence the work reported in this paper.

Acknowledgments

References

[1] S. Christe, B. Zeiger, R. Pfaff, M. Garcia, Introduction to the special issue on sounding rockets and instrumentation, J. Astron. Instrum. (ISSN: 2251-1717) 05 (01) (2016) 1602001, http://dx.doi.org/10.1142/S2251171716020013.

[2] M. Kobald, U. Fischer, K. Tomilin, A. Petrarolo, C. Schmierer, Hybrid experimental rocket stuttgart: A low-cost technology demonstrator, J. Spacecr. Rockets 55 (2) (2018) 484–500, http://dx.doi.org/10.2514/1.A34035.

[3] S. Robertson, S. Dickson, M. Horányi, Z. Sternovsky, M. Friedrich, D. Janches, L. Megner, B. Williams, Detection of meteoric smoke particles in the mesosphere by a rocket-borne mass spectrometer, J. Atmos. Sol.-Terr. Phys. (ISSN: 13646826) 118 (2014) 161–179, http://dx.doi.org/10.1016/j.jastp.2013.07.007.

[4] J.D. Moses, E. Antonucci, J. Newmark, F. Auchère, S. Fineschi, M. Romoli, D. Telloni, G. Massone, L. Zangrilli, M. Focardi, F. Landini, M. Pancrazzi, G. Rossi, A.M. Malvezzi, D. Wang, J.-C. Leclec'h, J.-P. Moalic, F. Rouesnel, L. Abbo, A. Canou, N. Barbey, C. Guennou, J.M. Laming, J. Lemen, J.-P. Wuelser, J.L. Kohl, L.D. Gardner, Global helium abundance measurements in the solar corona, Nat. Astronomy (ISSN: 2397-3366) (2020) http://dx.doi.org/10.1038/s41550-020-1156-6.

[5] A.N. Cha, K.R. Sembach, A.C. Danks, The distance to the vela supernova remnant, Astrophys. J. 515 (1) (1999) L25–L28, http://dx.doi.org/10.1086/311968.

[6] V. Dániel, R. Hudec, T. Baca, L. Pina, A. Inneman, V. Marsikova, M. Urban, O. Nentvich, V. Stehlikova, J. Tutt, REX LE X-ray telescope experiment overview, in: R. Hudec, L. Pina (Eds.), EUV and X-Ray Optics: Synergy Between Laboratory and Space VI, SPIE, 2019, p. 5, http://dx.doi.org/10.1117/12.2527288.

[7] F.D. Seward, P.A. Charles, Exploring the X-ray Universe, Cambridge University Press, Cambridge, 2010, pp. 136–139, http://dx.doi.org/10.1017/CBO9780511781513.

[8] B. Zeiger, A. Shipley, W. Cash, T. Rogers, T. Schultz, R. McEntaffer, M. Kaiser, The CODEX sounding rocket payload, 2011, p. 80760S, http://dx.doi.org/10.1117/12.887058.

[9] T. Rogers, R. McEntaffer, T. Schultz, B. Zeiger, P. Oakley, W. Cash, The OGRESS sounding rocket payload, 2013, 885911, http://dx.doi.org/10.1117/12.2023762.

[10] S.M. Kahn, P. Gorenstein, J. Harnden, F. R., F.D. Seward, Einstein observations of the VELA supernova remnant - the spatial structure of the hot emitting gas, Astrophys. J. 299 (1985) 821, http://dx.doi.org/10.1086/163748.

[11] A. Bamba, R. Yamazaki, J.S. Hiraga, Chandra observations of galactic supernova remnant vela jr.: A new sample of thin filaments emitting synchrotron X-Rays, Astrophys. J. (2005) http://dx.doi.org/10.1086/432711.

[12] D.M. Miles, R.L. McEntaffer, T.B. Schultz, B.D. Donovan, J.H. Tutt, D. Yastishock, T. Steiner, C.R. Hillman, J.A. McCoy, M. Wages, S. Hull, A. Falcone, D.N. Burrows, T. Anderson, M. McQuaide, T. Chattopadhyay, An introduction to the water recovery x-ray rocket, in: O.H. Siegmund (Ed.), UV, X-Ray, and Gamma-Ray Space Instrumentation for Astronomy XX, SPIE, 2017, p. 28, http://dx.doi.org/10.1117/12.2274249.

[13] D.M. Miles, S.V. Hull, T.B. Schultz, J.H. Tutt, M. Wages, B.D. Donovan, R.L. McEntaffer, A.D. Falcone, T. Anderson, E. Bray, D.N. Burrows, T. Chattopadhyay, C.M. Eichfeld, N. Empson, F. Grisé, C.R. Hillman, J.A. McCoy, M. McQuaide, B.J. Myers, T. Steiner, M.A. Verschuuren, D. Yastishock, N. Zhang, Water recovery X-Ray rocket grating spectrometer, J. Astron. Telescopes Instrum. Syst. (ISSN: 2329-4124) 5 (04) (2019) 1, http://dx.doi.org/10.1117/1.JATIS.5.4.044006.

[14] J.H. Tutt, R.L. McEntaffer, D.M. Miles, B.D. Donovan, C. Hillman, Grating alignment for the water recovery X-Ray rocket (WRXR), J. Astron. Instrum. 08 (03) (2019) 1950090, http://dx.doi.org/10.1142/S2251171719500090.

[15] M. Wages, S.V. Hull, A.D. Falcone, T.B. Schultz, T. Anderson, M. McQuaide, E. Bray, T. Chattopadhyay, D.N. Burrows, L. Buntic, R.M. McEntaffer, D.M. Miles, J.H. Tutt, T.B. Schultz, B.D. Donovan, C.R. Hillman, D. Yastishock, Flight camera package design, calibration, and performance for the water recovery X-ray rocket mission, in: O.H. Siegmund (Ed.), UV, X-Ray, and Gamma-Ray Space Instrumentation for Astronomy XXI, SPIE, 2019, p. 12, http://dx.doi.org/10.1117/12.2529361.

[16] X. Llopart, R. Ballabriga, M. Campbell, L. Tlustos, W. Wong, Timepix, a 65k programmable pixel readout chip for arrival time, energy and/or photon counting measurements, Nucl. Instrum. Methods Phys. Res. A 581 (1–2) (2007) 485–494, http://dx.doi.org/10.1016/j.nima.2007.08.079.

[17] W. Schmidt, A proposed X-ray focusing device with wide field of view for use in X-ray astronomy, Nucl. Instrum. Methods 127 (2) (1975) 285–292, http://dx.doi.org/10.1016/0029-554X(75)90501-7.

[18] J.R.P. Angel, Lobster eyes as X-ray telescopes, Astrophys. J. 233 (1979) 364, http://dx.doi.org/10.1086/157397.

[19] R. Hudec, Kirkpatrick-Baez (KB) and lobster eye (LE) optics for astronomical and laboratory applications, X-Ray Optics Instrum. 2010 (2010) 1–39, http://dx.doi.org/10.1155/2010/139148.

[20] T. Baca, D. Turecek, R. McEntaffer, R. Filgas, Rospix: modular software tool for automated data acquisitions of timepix detectors on robot operating system, J. Instrum. 13 (11) (2018) C11008, http://dx.doi.org/10.1088/1748-0221/13/11/C11008.

[21] V. Daniel, A. Inneman, I. Vertat, T. Baca, O. Nentvich, M. Urban, V. Stehlikova, L. Sieger, P. Skala, R. Filgas, V. Zadrazil, R. Linhart, J. Masopust, T. Jamroz, L. Pina, V. Marsikova, L. Mikulickova, E. Belas, S. Pospisil, Z. Vykydal, Y. Mora, R. Pavlica, In-orbit commissioning of czech nanosatellite VZLUSAT-1 for the QB50 mission with a demonstrator of a miniaturised lobster-eye X-Ray telescope and radiation shielding composite materials, Space Sci. Rev. 215 (5) (2019) 40, http://dx.doi.org/10.1007/s11214-019-0589-7.

[22] M. Urban, O. Nentvich, V. Stehlikova, T. Baca, V. Daniel, R. Hudec, VZLUSAT-1: Nanosatellite with miniature lobster eye X-ray telescope and qualification of the radiation shielding composite for space application, Acta Astronaut. 140 (2017) 96–104, http://dx.doi.org/10.1016/j.actaastro.2017.08.004.

[23] O. Nentvich, M. Urban, M. Blažek, A. Inneman, R. Hudec, L. Sieger, Lobster eye optics: position determination based on 1D optics with simple code mask, in: C. Morawe, A.M. Khounsary, S. Goto (Eds.), Advances in X-Ray/EUV Optics and Components XIV, SPIE, 2019, p. 31, http://dx.doi.org/10.1117/12.2528505.

[24] A.P. Willmore, C.J. Eyles, G.K. Skinner, M.P. Watt, Hard X-ray emission from the vela supernova remnant, Mon. Not. R. Astron. Soc. 254 (1) (1992) 139–145, http://dx.doi.org/10.1093/mnras/254.1.139.

[25] Z. Vykydal, J. Jakubek, USB lite – miniaturized readout interface for medipix2 detector, Nucl. Instrum. Methods 633 (2011) S48–S49, http://dx.doi.org/10.1016/j.nima.2010.06.118.

[26] V. Kraus, M. Holik, J. Jakubek, M. Kroupa, P. Soukup, Z. Vykydal, FITPix—fast interface for timepix pixel detectors, J. Instrum. 6 (01) (2011) C01079, http://dx.doi.org/10.1088/1748-0221/6/01/C01079.

[27] C. Granja, K. Kudela, J. Jakubek, P. Krist, D. Chvatil, J. Stursa, S. Polansky, Directional detection of charged particles and cosmic rays with the miniaturized radiation camera minipix timepix, Nucl. Instrum. Methods Phys. Res. A 911 (2018) 142–152, http://dx.doi.org/10.1016/j.nima.2018.09.140.

[28] E. Trojanova, J. Jakubek, D. Turecek, V. Sykora, P. Francova, V. Kolarova, L. Sefc, Evaluation of timepix3 based cdte photon counting detector for fully spectroscopic small animal SPECT imaging, J. Instrum. 13 (01) (2018) C01001, http://dx.doi.org/10.1088/1748-0221/13/01/C01001.

[29] R. Filgas, Space radiation monitoring with timepix, Astron. Nach. 339 (5) (2018) 386–390, http://dx.doi.org/10.1002/asna.201813511.

[30] N. Stoffle, L. Pinsky, M. Kroupa, S. Hoang, J. Idarraga, C. Amberboy, R. Rios, J. Hauss, J. Keller, A. Bahadori, E. Semones, D. Turecek, J. Jakubek, Z. Vykydal, S. Pospisil, Timepix-based radiation environment monitor measurements aboard the international space station, Nucl. Instrum. Methods Phys. Res. Sect. A (2015) http://dx.doi.org/10.1016/j.nima.2015.02.016.

[31] D. Turecek, L. Pinsky, J. Jakubek, Z. Vykydal, N. Stoffle, S. Pospisil, Small dosimeter based on timepix device for international space station, J. Instrum. (ISSN: 1748-0221) 6 (12) (2011) C12037, http://dx.doi.org/10.1088/1748-0221/6/12/C12037.

[32] C. Granja, S. Polansky, Z. Vykydal, S. Pospisil, A. Owens, Z. Kozacek, K. Mellab, M. Simcak, The SATRAM timepix spacecraft payload in open space on board the proba-v satellite for wide range radiation monitoring in LEO orbit, Planet. Space Sci. 125 (2016) 114–129, http://dx.doi.org/10.1016/j.pss.2016.03.009.

[33] T. Baca, M. Platkevic, J. Jakubek, A. Inneman, V. Stehlikova, M. Urban, O. Nentvich, M. Blazek, R. McEntaffer, V. Daniel, Miniaturized X-ray telescope for VZLUSAT-1 nanosatellite with timepix detector, J. Instrum. 11 (10) (2016) C10007, http://dx.doi.org/10.1088/1748-0221/11/10/C10007.

[34] V. Dániel, A. Inneman, L. Pína, V. Zadražil, T. Báča, V. Stehlíková, O. Nentvich, M. Urban, V. Maršíková, R. McEntaffer, J. Tutt, T. Schulz, X-ray Lobster eye all-sky monitor for rocket experiment, in: EUV and X-Ray Optics: Synergy Between Laboratory and Space V, 2017, 1023503, http://dx.doi.org/10.1117/12.2277515.

[35] W. Furnell, A. Shenoy, E. Fox, P. Hatfield, First results from the LUCID-timepix spacecraft payload in low earth orbit, Adv. Space Res. (ISSN: 02731177) 63 (5) (2019) 1523–1540, http://dx.doi.org/10.1016/j.asr.2018.10.045.

[36] P. Hatfield, W. Furnell, A. Shenoy, E. Fox, R. Parker, L. Thomas, The LUCID-timepix spacecraft payload and the CERN@school educational programme, J. Instrum. 13 (10) (2018) C10004, http://dx.doi.org/10.1088/1748-0221/13/10/C10004.

[37] R. Filgas, M. Malich, T. Kuwahara, J. Broulím, M. Holík, M. Sakal, Y. Murata, H. Tomio, S. Gohl, J.M. Pineda T., RISEPix—A timepix-based radiation monitor telescope onboard the RISESAT satellite, Astron. Nach. 340 (7) (2019) 674–680, http://dx.doi.org/10.1002/asna.201913674.

[38] J. Jakubek, Precise energy calibration of pixel detector working in time-over-threshold mode, Nucl. Instrum. Methods Phys. Res. A 633 (2011) S262–S266, http://dx.doi.org/10.1016/j.nima.2010.06.183.

4.3 Nova-C lunar lander

Last but not least, Timepix3 is part of the Tiger Eye 1 radiation measurement instrument that will be deployed on Intuitive Machine's Nova-C lander as part of NASA's Commercial Lunar Payload Service. The instrument is designed to measure the radiation environment on the lunar surface, including both charged particles and gamma rays.

An important aspect of the mission will be to provide detailed information on the types and energies of particles in the lunar environment. This data can be useful in assessing the risk of radiation exposure to people and equipment on the Moon. Other measurements, such as XRF and XRD, can be used to study the lunar surface and its composition. The detectors designed for this mission (Figure 4.12a) have already been tested and calibrated with respect to the presented research results on temperature dependence and related energy drift (Figure 4.12c). Individual correction models have been developed for each detector based on the newly proposed method. In this way, it will be possible to compensate for distortions that may occur, as was proposed in this thesis.
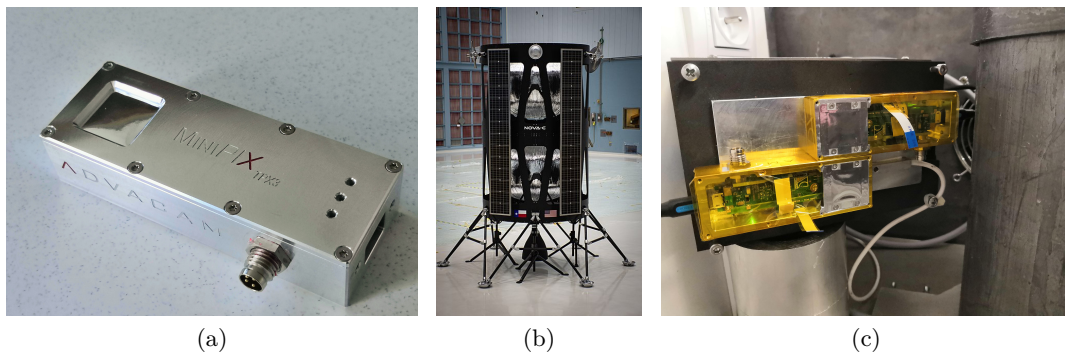
| (a) | (b) | (c) |

Fig. 4.12: Timepix3 detector designed for lunar lander mission and evaluation of its response to XRF radiation at different temperatures. (a) TPX3 detector, (b) Nova-C lunar lander[1], (c) temperature characterisation

---

[1]"NASA Selects First Commercial Moon Landing Services for Artemis Program" by *NASA/Goddard/Rebecca Roth* is licensed under CC BY 2.0

Chapter 5
Conclusion

This thesis deals with the detection of X–rays, with particular emphasis on hybrid pixel detectors and their suitability for use in harsh space environments characterised by extreme temperature changes, strong radiation and vacuum conditions. This type of detector is based on the positive experience of its use in such challenging environments, as we demonstrated by the Rocket Experiment and the VZLUSAT-1 nanosatellite, which is exceeding its expected operational lifetime. This initial technology mission also provides valuable scientific data, such as measurements of solar flares and material degradation.

The study also investigated the effects of hostile environments on detector accuracy, with particular attention paid to thermal cycling and vacuum testing. The sensing system has been extensively tested throughout the years and provided the means for other research to be conducted. The thesis details the extensive testing and validation of the detector system in various measurement modes irradiated by radionuclides as well as the characteristic X–ray fluorescence radiation over a wide temperature range ($-40\,^\circ$C to $70\,^\circ$C) covering a significant part of the range defined by ESA and many applications. Several issues in the field of radiation energy measurement have been addressed and the temperature influence on the measured energy of the incident radiation is described in detail.

One of the most significant contributions of this thesis is the detailed description and characterisation of the energy spectrum distortion caused by temperature variations. This can result in a shift of the measured energy of up to $30\,\%$ from the nominal spectral peak. Two novel correction methods that minimise the energy measurement error to less than about $1.5\,\%$ for the Timepix3 detectors are presented. The thesis proposes a complex correction method for both constant and variable temperature drifts based on detector characterisation. It provides experimental verification of the proposed compensation model also in the vacuum chamber and successfully demonstrates its possibilities of extrapolation and generalisation for common use with a variety of Timepix3 detectors with the same detection layer. To the best of our knowledge, this thesis and the accompanying publications are unique and the first to describe in detail the temperature dependence and correction methods of energy measurements using the Timepix3 detector.

In addition, the hybrid pixel detector has been used as an X–ray telescope in a unique combination with Lobster-Eye optics in a rocket experiment and a CubeSat mission. This study's results, methods and models have already been used to prepare and calibrate detectors for the Nova-C lunar lander. The implications of this research extend beyond space applications and are relevant to other applications in science and industries where there is a need to increase operational range and capability, reduce workforce (series of calibrations) and power requirements (thermal stabilisation/cooling).

Overall, this thesis presents significant advances in the field of X–ray measurements in space using hybrid pixel detectors from the Timepix3 family, providing new insights into the effects of the harsh space environment on detector accuracy and presenting novel correction methods to address these effects. These results have implications for a wide range of applications and industries, not only in space where changing operating conditions are most significant. The proposed compensation on the Timepix3 detector can be used, for example, on vehicles carrying GRB alert systems, for materials science or the localisation of compact gamma-ray sources (Compton camera).

References

[1] J. P. Grotzinger, J. Crisp, A. R. Vasavada, R. C. Anderson, C. J. Baker, R. Barry, D. F. Blake, *et al.*, "Mars science laboratory mission and science investigation," *Space Science Reviews*, vol. 170, no. 1-4, pp. 5–56, Jul. 2012. DOI: `10.1007/s11214-012-9892-2`.

[2] D. M. Hassler, C. Zeitlin, R. F. Wimmer-Schweingruber, B. Ehresmann, S. Rafkin, J. L. Eigenbrode, D. E. Brinza, *et al.*, "Mars' surface radiation environment measured with the mars science laboratory's curiosity rover," *Science*, vol. 343, no. 6169, Jan. 2014. DOI: `10.1126/science.1244797`.

[3] D. L. Bish, D. F. Blake, D. T. Vaniman, S. J. Chipera, R. V. Morris, D. W. Ming, A. H. Treiman, *et al.*, "X-ray diffraction results from mars science laboratory: Mineralogy of rocknest at gale crater," *Science*, vol. 341, no. 6153, Sep. 2013. DOI: `10.1126/science.1238932`.

[4] P. Predehl, R. Andritschke, V. Arefiev, V. Babyshkin, O. Batanov, W. Becker, H. Böhringer, *et al.*, "The eROSITA x-ray telescope on SRG," *Astronomy &amp Astrophysics*, vol. 647, A1, Feb. 2021. DOI: `10.1051/0004-6361/202039313`.

[5] D. N. Burrows, J. E. Hill, J. A. Nousek, J. A. Kennea, A. Wells, J. P. Osborne, A. F. Abbey, *et al.*, "The swift x-ray telescope," *Space Science Reviews*, vol. 120, no. 3-4, pp. 165–195, Oct. 2005. DOI: `10.1007/s11214-005-5097-2`.

[6] S. D. Barthelmy, L. M. Barbier, J. R. Cummings, E. E. Fenimore, N. Gehrels, D. Hullinger, H. A. Krimm, *et al.*, "The burst alert telescope (BAT) on the SWIFT midex mission," *Space Science Reviews*, vol. 120, no. 3-4, pp. 143–164, Oct. 2005. DOI: `10.1007/s11214-005-5096-3`.

[7] V. Daniel, A. Inneman, I. Vertat, T. Baca, O. Nentvich, M. Urban, V. Stehlikova, *et al.*, "In-Orbit Commissioning of Czech Nanosatellite VZLUSAT-1 for the QB50 Mission with a Demonstrator of a Miniaturised Lobster-Eye X-Ray Telescope and Radiation Shielding Composite Materials," *Space Science Reviews*, vol. 215, no. 5, Jul. 2019. DOI: `10.1007/s11214-019-0589-7`.

[8] M. Urban, O. Nentvich, V. Stehlikova, T. Baca, V. Daniel, and R. Hudec, "VZLUSAT-1: Nanosatellite with miniature lobster eye X-ray telescope and qualification of the radiation shielding composite for space application," *Acta Astronautica*, vol. 140, pp. 96–104, Nov. 2017. DOI: `10.1016/j.actaastro.2017.08.004`.

[9] M. Urban, O. Nentvich, D. Doubravova, O. Petr, A. J. Inneman, R. Hudec, and L. Sieger, "Timepix: Influence of temperature and vacuum on equalisation of X-ray detector and its verification," in *SPIE Proceedings: UV, X-Ray, and Gamma-Ray Space Instrumentation for Astronomy XXI*, O. H. Siegmund, Ed., SPIE, Sep. 2019. DOI: `10.1117/12.2528503`.

[10] M. Urban, D. Doubravova, and O. Nentvich, "Thermal vacuum testing of Timepix3 detector," *Journal of Instrumentation*, vol. 15, no. 03, pp. C03040–C03040, Mar. 2020. DOI: `10.1088/1748-0221/15/03/c03040`.

[11] M. Urban and D. Doubravová, "Timepix3: Temperature influence on X-ray measurements in counting mode with Si sensor," *Radiation Measurements*, vol. 141, p. 106 535, Feb. 2021. DOI: `10.1016/j.radmeas.2021.106535`.

[12] M. Urban, O. Nentvich, L. Marek, R. Hudec, and L. Sieger, "Timepix3: Temperature Influence on Radiation Energy Measurement with Si Sensor," *Sensors*, vol. 23, no. 4, p. 2201, Feb. 2023. DOI: `10.3390/s23042201`.

[13] M. Urban, O. Nentvich, L. Marek, D. Hladik, R. Hudec, and L. Sieger, "Timepix3: Compensation of Thermal Distortion of Energy Measurement," *Sensors*, vol. 23, no. 6, p. 3362, Mar. 2023. DOI: `10.3390/s23063362`.

[14] C. Granja, S. Polansky, Z. Vykydal, S. Pospisil, A. Owens, Z. Kozacek, K. Mellab, *et al.*, "The SATRAM timepix spacecraft payload in open space on board the proba-v satellite for wide range radiation monitoring in LEO orbit," *Planetary and Space Science*, vol. 125, pp. 114–129, Jun. 2016. DOI: `10.1016/j.pss.2016.03.009`.

[15] R. Filgas, M. Malich, T. Kuwahara, J. Broulím, M. Holík, M. Sakal, Y. Murata, *et al.*, "RISEPix—a timepix-based radiation monitor telescope onboard the RISESAT satellite," *Astronomische Nachrichten*, vol. 340, no. 7, pp. 674–680, Aug. 2019. DOI: `10.1002/asna.201913674`.

[16] W. Furnell, A. Shenoy, E. Fox, and P. Hatfield, "First results from the LUCID-timepix spacecraft payload onboard the TechDemoSat-1 satellite in low earth orbit," *Advances in Space Research*, vol. 63, no. 5, pp. 1523–1540, Mar. 2019. DOI: `10.1016/j.asr.2018.10.045`.

[17] M. J. Berger and J. H. Hubbell, "XCOM: Photon cross sections on a personal computer," Tech. Rep., Jul. 1987. DOI: `10.2172/6016002`.

[18] G. F. Knoll, *Radiation detection and measurement, Glenn F. Knoll.* Wiley, 2000, p. 802, ISBN: 0471073385.

[19] M. Platkevič, "Signal processing and data read-out from position sensitive pixel detectors," Ph.D. dissertation, Faculty of Nuclear Sciences and Physical Engineering, Czech Technical University in Prague, Czech Republic, 2014.

[20] R. Ballabriga, M. Campbell, and X. Llopart, "Asic developments for radiation imaging applications: The medipix and timepix family," *Nuclear Instruments and Methods in Physics Research Section A: Accelerators, Spectrometers, Detectors and Associated Equipment*, vol. 878, pp. 10–23, Jan. 2018. DOI: `10.1016/j.nima.2017.07.029`.

[21] B. Bergmann, T. Billoud, C. Leroy, and S. Pospisil, "Characterization of the radiation field in the ATLAS experiment with timepix detectors," *IEEE Transactions on Nuclear Science*, vol. 66, no. 7, pp. 1861–1869, Jul. 2019. DOI: `10.1109/tns.2019.2918365`.

[22] J. Jakubek, A. Cejnarova, T. Holy, S. Pospisil, J. Uher, and Z. Vykydal, "Pixel detectors for imaging with heavy charged particles," *Nuclear Instruments and Methods in Physics Research Section A: Accelerators, Spectrometers, Detectors and Associated Equipment*, vol. 591, no. 1, pp. 155–158, Jun. 2008. DOI: `10.1016/j.nima.2008.03.091`.

[23] J. Dudak, "High-resolution x-ray imaging applications of hybrid-pixel photon counting detectors timepix," *Radiation Measurements*, vol. 137, p. 106 409, Sep. 2020. DOI: `10.1016/j.radmeas.2020.106409`.

[24] R. A. Darwish, L. Marcu, and E. Bezak, "Overview of current applications of the timepix detector in spectroscopy, radiation and medical physics," *Applied Spectroscopy Reviews*, vol. 55, no. 3, pp. 243–261, Mar. 2019. DOI: `10.1080/05704928.2019.1580202`.

[25] L. Loaiza, G. A. Roque, C. A. Avila, L. M. Mendoza, R. J. Rueda, and J. M. Racedo, "Feasibility study of a TIMEPIX detector for mammography applications," in *13th International Conference on Medical Information Processing and Analysis*, J. Brieva, J. D. García, N. Lepore, and E. Romero, Eds., SPIE, Nov. 2017. DOI: `10.1117/12.2285910`.

[26] S. Procz, C. Avila, J. Fey, G. Roque, M. Schuetz, and E. Hamann, "X-ray and gamma imaging with medipix and timepix detectors in medical research," *Radiation Measurements*, vol. 127, p. 106 104, Aug. 2019. DOI: `10.1016/j.radmeas.2019.04.007`.

[27] J. Watt, D. W. Davidson, C. Johnston, C. Smith, L. Tlustos, B. Mikulec, K. M. Smith, *et al.*, "Dose reductions in dental x-ray imaging using medipix," *Nuclear Instruments and Methods in Physics Research Section A: Accelerators, Spectrometers, Detectors and Associated Equipment*, vol. 513, no. 1-2, pp. 65–69, Nov. 2003. DOI: `10.1016/j.nima.2003.08.003`.

[28] J. Zemlicka, J. Jakubek, M. Kroupa, D. Hradil, J. Hradilova, and H. Mislerova, "Analysis of painted arts by energy sensitive radiographic techniques with the pixel detector timepix," *Journal of Instrumentation*, vol. 6, no. 01, pp. C01066–C01066, Jan. 2011. DOI: `10.1088/1748-0221/6/01/c01066`.

[29] T. Baca, P. Stibinger, D. Doubravova, D. Turecek, J. Solc, J. Rusnak, M. Saska, *et al.*, "Gamma radiation source localization for micro aerial vehicles with a miniature single-detector compton event camera," in *2021 International Conference on Unmanned Aircraft Systems (ICUAS)*, IEEE, Jun. 2021. DOI: `10.1109/icuas51884.2021.9476766`.

[30] P. Stibinger, T. Baca, and M. Saska, "Localization of ionizing radiation sources by cooperating micro aerial vehicles with pixel detectors in real-time," *IEEE Robotics and Automation Letters*, vol. 5, no. 2, pp. 3634–3641, Apr. 2020. DOI: `10.1109/lra.2020.2978456`.

[31] X. Llopart, R. Ballabriga, M. Campbell, L. Tlustos, and W. Wong, "Timepix, a 65k programmable pixel readout chip for arrival time, energy and/or photon counting measurements," vol. 581, pp. 485–494, 2007, ISSN: 0168-9002. DOI: `10.1016/j.nima.2007.08.079`.

[32] T. Poikela, J. Plosila, T. Westerlund, M. Campbell, M. D. Gaspari, X. Llopart, V. Gromov, *et al.*, "Timepix3: A 65k channel hybrid pixel readout chip with simultaneous ToA/ToT and sparse readout," *Journal of Instrumentation*, vol. 9, no. 05, pp. C05013–C05013, May 2014. DOI: `10.1088/1748-0221/9/05/c05013`.

[33] D. Kozhevnikov and P. Smolyanskiy, "Equalization of medipix family detector energy thresholds using x-ray tube spectrum high energy cut-off," *Journal of Instrumentation*, vol. 14, no. 01, T01006–T01006, Jan. 2019. DOI: `10.1088/1748-0221/14/01/t01006`.

[34] J. Jakubek, "Precise energy calibration of pixel detector working in time-over-threshold mode," *Nuclear Instruments and Methods in Physics Research Section A: Accelerators, Spectrometers, Detectors and Associated Equipment*, vol. 633, S262–S266, May 2011. DOI: `10.1016/j.nima.2010.06.183`.

[35] D. Turecek, J. Jakubek, M. Kroupa, and P. Soukup, "Energy calibration of pixel detector working in time-over-threshold mode using test pulses," in *2011 IEEE Nuclear Science Symposium Conference Record*, IEEE, Oct. 2011. DOI: `10.1109/nssmic.2011.6154668`.

[36] M. Kroupa, J. Jakubek, and P. Soukup, "Optimization of the spectroscopic response of the timepix detector," *Journal of Instrumentation*, vol. 7, no. 02, pp. C02058–C02058, Feb. 2012. DOI: `10.1088/1748-0221/7/02/c02058`.

[37] M. Kroupa, T. Campbell-Ricketts, A. Bahadori, and A. Empl, "Techniques for precise energy calibration of particle pixel detectors," *Review of Scientific Instruments*, vol. 88, no. 3, p. 033 301, Mar. 2017. DOI: `10.1063/1.4978281`.

[38] S. P. George, M. Kroupa, S. Wheeler, S. Kodaira, H. Kitamura, L. Tlustos, T. Campbell-Ricketts, *et al.*, "Very high energy calibration of silicon timepix detectors," *Journal of Instrumentation*, vol. 13, no. 11, P11014–P11014, Nov. 2018. DOI: `10.1088/1748-0221/13/11/p11014`.

[39] C. Leroy and C. Papadatos, "A proposed energy calibration procedure taking into account high per pixel energies using a silicon TPX3 detector," *Nuclear Instruments and Methods in Physics Research Section A: Accelerators, Spectrometers, Detectors and Associated Equipment*, vol. 1045, p. 167 567, Jan. 2023. DOI: `10.1016/j.nima.2022.167567`.

[40] M. Holik, G. Ahmadov, J. Broulim, J. Zich, D. Berikov, Y. Mora, Y. Kopatch, *et al.*, "Alpha calibration of the timepix pixel detector exploiting energy information gained from a common electrode signal," *Journal of Instrumentation*, vol. 14, no. 06, pp. C06022–C06022, Jun. 2019. DOI: `10.1088/1748-0221/14/06/c06022`.

[41] M. Sommer, C. Granja, S. Kodaira, and O. Ploc, "High-energy per-pixel calibration of timepix pixel detector with laboratory alpha source," *Nuclear Instruments and Methods in Physics Research Section A: Accelerators, Spectrometers, Detectors and Associated Equipment*, vol. 1022, p. 165 957, Jan. 2022. DOI: `10.1016/j.nima.2021.165957`.

[42] R. Filgas, "Space radiation monitoring with timepix," *Astronomische Nachrichten*, vol. 339, no. 5, pp. 386–390, Jun. 2018. DOI: `10.1002/asna.201813511`.

[43] N. Stoffle, L. Pinsky, M. Kroupa, S. Hoang, J. Idarraga, C. Amberboy, R. Rios, *et al.*, "Timepix-based radiation environment monitor measurements aboard the international space station," *Nuclear Instruments and Methods in Physics Research Section A: Accelerators, Spectrometers, Detectors and Associated Equipment*, vol. 782, pp. 143–148, May 2015. DOI: `10.1016/j.nima.2015.02.016`.

[44] S. Gohl, B. Bergmann, H. Evans, P. Nieminen, A. Owens, and S. Posipsil, "Study of the radiation fields in LEO with the space application of timepix radiation monitor (SATRAM)," *Advances in Space Research*, vol. 63, no. 5, pp. 1646–1660, Mar. 2019. DOI: `10.1016/j.asr.2018.11.016`.

[45] T. Baca, M. Jilek, I. Vertat, M. Urban, O. Nentvich, R. Filgas, C. Granja, *et al.*, "Timepix in LEO Orbit onboard the VZLUSAT-1 Nanosatellite: 1-year of Space Radiation Dosimetry Measurements," *Journal of Instrumentation*, vol. 13, no. 11, pp. C11010–C11010, Nov. 2018. DOI: `10.1088/1748-0221/13/11/c11010`.

Appendix A
Author's scientific research activities

This chapter is divided into several sections. Section A.1 provides a list of the author's publications according to their relevance to this thesis. The second section A.2 includes a summary of the activities of the author within the scientific community. The final section A.3 is a list of citations to the author's publications.

A.1 Publications

The list of the author's publications is divided into several sections based on the classification into papers related to the topic of the doctoral thesis and unrelated papers, respectively articles in peer-reviewed journals and conference articles.

◼ A.1.1 Thesis directly related author's publications

Thesis directly related articles in peer-reviewed journals

1. **M. Urban**, O. Nentvich, L. Marek, D. Hladik, R. Hudec, and L. Sieger, "Timepix3: Compensation of Thermal Distortion of Energy Measurement," *Sensors*, vol. 23, no. 6, p. 3362, Mar. 2023. DOI: `10.3390/s23063362`.

2. **M. Urban**, O. Nentvich, L. Marek, R. Hudec, and L. Sieger, "Timepix3: Temperature Influence on Radiation Energy Measurement with Si Sensor," *Sensors*, vol. 23, no. 4, p. 2201, Feb. 2023. DOI: `10.3390/s23042201`.

3. **M. Urban** and D. Doubravová, "Timepix3: Temperature influence on X-ray measurements in counting mode with Si sensor," *Radiation Measurements*, vol. 141, p. 106 535, Feb. 2021. DOI: `10.1016/j.radmeas.2021.106535`.

4. **M. Urban**, O. Nentvich, T. Báča, I. Veřtát, V. Maršíková, D. Doubravová, V. Dániel, *et al.*, "REX: X-ray experiment on the water recovery rockets," *Acta Astronautica*, vol. 184, pp. 1–10, Jul. 2021. DOI: `10.1016/j.actaastro.2021.03.019`.

5. **M. Urban**, D. Doubravova, and O. Nentvich, "Thermal vacuum testing of Timepix3 detector," *Journal of Instrumentation*, vol. 15, no. 03, pp. C03040–C03040, Mar. 2020. DOI: `10.1088/1748-0221/15/03/c03040`.

6. V. Daniel, A. Inneman, I. Vertat, T. Baca, O. Nentvich, **M. Urban**, V. Stehlikova, *et al.*, "In-Orbit Commissioning of Czech Nanosatellite VZLUSAT-1 for the QB50 Mission with a Demonstrator of a Miniaturised Lobster-Eye X-Ray Telescope and Radiation Shielding Composite Materials," *Space Science Reviews*, vol. 215, no. 5, Jul. 2019. DOI: `10.1007/s11214-019-0589-7`.

7. T. Baca, M. Jilek, I. Vertat, **M. Urban**, O. Nentvich, R. Filgas, C. Granja, *et al.*, "Timepix in LEO Orbit onboard the VZLUSAT-1 Nanosatellite: 1-year of Space Radiation Dosimetry Measurements," *Journal of Instrumentation*, vol. 13, no. 11, pp. C11010–C11010, Nov. 2018. DOI: 10.1088/1748-0221/13/11/c11010.

8. **M. Urban**, O. Nentvich, V. Stehlikova, T. Baca, V. Daniel, and R. Hudec, "VZLUSAT-1: Nanosatellite with miniature lobster eye X-ray telescope and qualification of the radiation shielding composite for space application," *Acta Astronautica*, vol. 140, pp. 96–104, Nov. 2017. DOI: 10.1016/j.actaastro.2017.08.004.

9. **M. Urban**, O. Nentvich, V. Stehlikova, and L. Sieger, "Detection of X-ray spectra and images by Timepix," *Contributions of the Astronomical Observatory Skalnate Pleso*, vol. 47, pp. 151–156, 2 2017, ISSN: 1335-1842.

10. V. Stehlikova, **M. Urban**, O. Nentvich, V. Daniel, L. Sieger, and J. Tutt, "Hard X-ray Vela supernova observation on rocket experiment WRX-R," *Contributions of the Astronomical Observatory Skalnate Pleso*, vol. 47, pp. 165–169, 2 2017, ISSN: 1335-1842.

11. T. Baca, M. Platkevic, J. Jakubek, A. Inneman, V. Stehlikova, **M. Urban**, O. Nentvich, *et al.*, "Miniaturized X-ray telescope for VZLUSAT-1 nanosatellite with Timepix detector," *Journal of Instrumentation*, vol. 11, no. 10, pp. C10007–C10007, Oct. 2016. DOI: 10.1088/1748-0221/11/10/c10007.

Thesis directly related conference articles

1. V. Dániel, R. Hudec, T. Baca, L. Pina, A. Inneman, V. Marsikova, **M. Urban**, *et al.*, "REX LE X-ray telescope experiment overview," in *SPIE Proceedings: EUV and X-Ray Optics: Synergy between Laboratory and Space VI*, R. Hudec and L. Pina, Eds., SPIE, Apr. 2019. DOI: 10.1117/12.2527288.

2. **M. Urban**, O. Nentvich, D. Doubravova, O. Petr, A. J. Inneman, R. Hudec, and L. Sieger, "Timepix: Influence of temperature and vacuum on equalisation of X-ray detector and its verification," in *SPIE Proceedings: UV, X-Ray, and Gamma-Ray Space Instrumentation for Astronomy XXI*, O. H. Siegmund, Ed., SPIE, Sep. 2019. DOI: 10.1117/12.2528503.

3. **M. Urban**, O. Nentvich, V. Stehlikova, and L. Sieger, "Uncooled spectrometer for X-ray astrophysics," in *SPIE Proceedings: EUV and X-Ray Optics: Synergy between Laboratory and Space V*, R. Hudec and L. Pina, Eds., SPIE, May 2017. DOI: 10.1117/12.2265744.

4. V. Dániel, A. Inneman, L. Pína, V. Zadražil, T. Báča, V. Stehlíková, O. Nentvich, *et al.*, "X-ray Lobster Eye all-sky monitor for rocket experiment," in *SPIE Proceedings: EUV and X-Ray Optics: Synergy between Laboratory and Space V*, R. Hudec and L. Pina, Eds., SPIE, May 2017. DOI: 10.1117/12.2277515.

5. V. Dániel, L. Pína, A. Inneman, V. Zadražil, T. Báča, M. Platkevič, V. Stehlíková, *et al.*, "Terrestrial gamma-ray flashes monitor demonstrator on CubeSat," in *SPIE Proceedings: CubeSats and NanoSats for Remote Sensing*, T. S. Pagano, Ed., SPIE, Sep. 2016. DOI: 10.1117/12.2240299.

■ **A.1.2 Other author's publications**

Other articles in peer-reviewed journals

1. O. Nentvich, **M. Urban**, and R. Hudec, "PyXLA: Python X-ray-tracing for Lobster-Eye Application," *Journal of Optics*, Mar. 2023. DOI: `10.1088/2040-8986/acc2cc`.

2. L. Sieger, O. Nentvich, and **M. Urban**, "Satellite temperature measurement in LEO and improvement method of temperature sensors calibration based on the measured data," *Astronomische Nachrichten*, vol. 340, no. 7, pp. 652–657, Aug. 2019. DOI: `10.1002/asna.201913671`.

3. R. Hudec, L. Pina, V. Marsikova, O. Nentvich, **M. Urban**, and A. Inneman, "Kirkpatrick Baez X-ray optics for astrophysics: Recent status," *Contributions of the Astronomical Observatory Skalnate Pleso*, vol. 48, pp. 437–445, 3 2018, ISSN: 1335-1842.

4. R. Hudec, L. Pina, V. Marsikova, O. Nentvich, **M. Urban**, and A. Inneman, "Lobster Eye X-ray optics for astrophysics: Recent status," *Contributions of the Astronomical Observatory Skalnate Pleso*, vol. 48, pp. 456–465, 3 2018, ISSN: 1335-1842.

5. L. Pina, R. Hudec, A. Inneman, O. Nentvich, **M. Urban**, V. Marsikova, V. Stehlikova, *et al.*, "Multi-Foil X-ray optics tests at PANTER: Preliminary results," *Contributions of the Astronomical Observatory Skalnate Pleso*, vol. 48, pp. 466–475, 3 2018, ISSN: 1335-1842.

6. V. Stehlikova, A. C. Probst, O. Nentvich, **M. Urban**, L. Sieger, T. Doehring, and R. Hudec, "Study of multiple layers coatings for x-ray mirrors," *Contributions of the Astronomical Observatory Skalnate Pleso*, vol. 48, pp. 488–497, 3 2018, ISSN: 1335-1842.

7. **M. Urban**, O. Nentvich, V. Stehlikova, L. Sieger, and L. Mikulickova, "Outgassing monitor on VZLUSAT-1: Preliminary results," *Astronomische Nachrichten*, vol. 339, no. 5, pp. 367–370, Jun. 2018. DOI: `10.1002/asna.201813507`.

8. O. Nentvich, **M. Urban**, V. Stehlikova, L. Sieger, and A. Inneman, "VZLUSAT-1: Health monitoring system, preliminary results," *Astronomische Nachrichten*, vol. 339, no. 5, pp. 397–402, Jun. 2018. DOI: `10.1002/asna.201813513`.

9. V. Stehlikova, **M. Urban**, O. Nentvich, and L. Sieger, "Radiation resistance monitor on VZLUSAT-1: Preliminary results," *Astronomische Nachrichten*, vol. 339, no. 5, pp. 382–385, Jun. 2018. DOI: `10.1002/asna.201813510`.

10. O. Nentvich, **M. Urban**, V. Stehlikova, L. Sieger, and R. Hudec, "Lobster eye X-ray optics: Data processing from two 1D modules," *Contributions of the Astronomical Observatory Skalnate Pleso*, vol. 47, pp. 178–183, 2 2017, ISSN: 1335-1842.

Other conference articles

1. O. Nentvich, **M. Urban**, M. Blažek, A. Inneman, R. Hudec, and L. Sieger, "Lobster eye optics: position determination based on 1D optics with simple code mask," in *SPIE Proceedings: Advances in X-Ray/EUV Optics and Components XIV*, C. Morawe, A. M. Khounsary, and S. Goto, Eds., SPIE, Sep. 2019. DOI: 10.1117/12.2528505.

2. O. Nentvich, V. Stehlikova, **M. Urban**, R. Hudec, and L. Sieger, "Data processing from lobster eye type optics," in *SPIE Proceedings: EUV and X-Ray Optics: Synergy between Laboratory and Space V*, R. Hudec and L. Pina, Eds., SPIE, May 2017. DOI: 10.1117/12.2265724.

3. L. Mikulickova, L. Pina, A. Inneman, D. Doubravova, V. Marsikova, L. Sieger, **M. Urban**, *et al.*, "Optimization of microroughness of replicated X-ray optics," in *SPIE Proceedings: EUV and X-Ray Optics: Synergy between Laboratory and Space V*, R. Hudec and L. Pina, Eds., SPIE, May 2017. DOI: 10.1117/12.2265810.

4. V. Stehlikova, **M. Urban**, O. Nentvich, A. Inneman, T. Döhring, and A.-C. Probst, "Study of lobster eye optics with iridium coated X-ray mirrors for a rocket experiment," in *SPIE Proceedings: EUV and X-Ray Optics: Synergy between Laboratory and Space V*, R. Hudec and L. Pina, Eds., SPIE, May 2017. DOI: 10.1117/12.2265769.

5. V. Daniel, **M. Urban**, O. Nentvich, and V. Stehlikova, "VZLUSAT-1: verification of new materials and technologies for space," in *SPIE Proceedings: CubeSats and NanoSats for Remote Sensing*, T. S. Pagano, Ed., SPIE, Sep. 2016. DOI: 10.1117/12.2244035.

A.2 Recognition by the scientific community

A.2.1 Editorship of a special issue of the WoS excerpted journal

1. R. Hudec, **M. Urban**, O. Nentvich, "Special Issue: Integral/Bart Workshop (IBWS)", *Astronomische Nachrichten*, vol.340, no 7, Aug. 2019

2. R. Hudec, **M. Urban**, O. Nentvich, "Special Issue: 15th INTEGRAL / BART Workshop", *Astronomische Nachrichten*, vol.339, no 5, Jun. 2018

3. R. Hudec, **M. Urban**, O. Nentvich, "Special Issue: 10th International Workshop on Astronomical X—Ray Optics", *Contributions Of The Astronomical Observatory Skalnate Pleso*, vol.48, no 3, Aug. 2018

4. **M. Urban**, O. Nentvich, R. Hudec, "Special Issue: 14th INTEGRAL/BART Workshop", *Contributions Of The Astronomical Observatory Skalnate Pleso*, vol.47, no 2, Aug. 2017

A.2.2 Member of organising committee of international conference

1. 17th INTEGRAL/BART Workshop 2023
2. 16th INTEGRAL/BART Workshop 2019
3. 15th INTEGRAL/BART Workshop 2018
4. 14th INTEGRAL/BART Workshop 2017
5. 13th INTEGRAL/BART Workshop 2016
6. 13th International Workshop on Astronomical X-Ray Optics 2022
7. 12th International Workshop on Astronomical X-Ray Optics 2019
8. 11th International Workshop on Astronomical X-Ray Optics 2018
9. 10th International Workshop on Astronomical X-Ray Optics 2017
10. 09th International Workshop on Astronomical X-Ray Optics 2016

A.3 Citations of author's publications

Citations of the author's work were extracted from the Web of Science database. First- and second-order self-citations are excluded. The author has reached h-index 5. The data were gathered on March 14th, 2023.

> T. Baca, M. Platkevic, J. Jakubek, A. Inneman, V. Stehlikova, **M. Urban**, O. Nentvich, *et al.*, "Miniaturized X-ray telescope for VZLUSAT-1 nanosatellite with Timepix detector," *Journal of Instrumentation*, vol. 11, no. 10, pp. C10007–C10007, Oct. 2016. DOI: `10.1088/1748-0221/11/10/c10007`

1. V. Simon and R. Hudec, "Perspectives of the LOBSTER-EYE monitor in the soft X-ray observing the Galactic center region," *Journal of High Energy Astrophysics*, vol. 35, pp. 69–76, Jan. 2022. DOI: `10.1016/j.jheap.2022.06.001`.

2. V. V. Lider, "Grazing-Incidence Focusing Optics for X-ray Telescopes (Review)," *Instruments and Experimental Techniques*, vol. 65, no. 2, pp. 191–217, Jan. 2022. DOI: `10.1134/S002044122202004X`.

3. M. Ruffenach, S. Bourdarie, B. Bergmann, S. Gohl, J. Mekki, and J. Vaille, "A New Technique Based on Convolutional Neural Networks to Measure the Energy of Protons and Electrons With a Single Timepix Detector," *IEEE Transactions on Nuclear Science*, vol. 68, no. 8, 1-3, pp. 1746–1753, Jan. 2021. DOI: `10.1109/TNS.2021.3071583`.

4. O. Urban, O. Vavroch, L. Polacek, V. Georgiev, P. Burian, P. Turjanica, P. Fiala, *et al.*, "Hodoscope with Timepix detectors for PilsenCube2 cubesat," *Nuclear Instruments & Methods in Physics Research Section A-Accelerators Spectrometers Detectors and Associated Equipment*, vol. 980, Nov. 2020, ISSN: 0168-9002. DOI: `10.1016/j.nima.2020.164462`.

5. R. Filgas, M. Malich, T. Kuwahara, J. Broulim, M. Holik, M. Sakal, Y. Murata, *et al.*, "RISEPix-A Timepix-based radiation monitor telescope onboard the RISESAT satellite," *Astronomische Nachrichten*, vol. 340, no. 7, SI, pp. 674–680, Jan. 2019. DOI: `10.1002/asna.201913674`.

6. V. Tichy, M. Barbera, R. Hudec, and R. Willingale, "Effective collecting area of lobster eye optics and optimal value of effective angle," *Experimental Astronomy*, vol. 47, no. 1-2, pp. 161–175, Jan. 2019. DOI: `10.1007/s10686-019-09622-2`.

7. W. Furnell, A. Shenoy, E. Fox, and P. Hatfield, "First results from the LUCID-Timepix spacecraft payload onboard the TechDemoSat-1 satellite in Low Earth Orbit," *Advances in Space Research*, vol. 63, no. 5, pp. 1523–1540, Jan. 2019. DOI: `10.1016/j.asr.2018.10.045`.

8. P. Hatfield, W. Furnell, A. Shenoy, E. Fox, B. Parker, L. Thomas, and E. A. C. Rushton, "IRIS opens pupils' eyes to real space research," *Astronomy & Geophysics*, vol. 60, no. 1, pp. 22–24, Jan. 2019. DOI: `10.1093/astrogeo/atz046`.

9. R. Hudec, "X/EUV and UV optics for miniature cube satellites payloads," in *EUV and X-ray Optics: Synergy between Laboratory and Space VI*, vol. 11032, 2019. DOI: `10.1117/12.2525542`.

10. P. Hatfield, W. Furnell, A. Shenoy, E. Fox, R. Parker, and L. Thomas, "The LUCID-Timepix spacecraft payload and the CERN School educational programme," *Journal of Instrumentation*, vol. 13, Jan. 2018. DOI: `10.1088/1748-0221/13/10/C10004`.

11. R. Filgas, "Space radiation monitoring with Timepix," *Astronomische Nachrichten*, vol. 339, no. 5, SI, pp. 386–390, Jan. 2018. DOI: `10.1002/asna.201813511`.

12. R. Hudec, "Low-dispersion spectroscopy with cubesats and photographic plates," *Astronomische Nachrichten*, vol. 339, no. 5, SI, pp. 416–419, Jan. 2018. DOI: `10.1002/asna.201813517`.

13. V. Tichy and R. Willingale, "Optimization of mirror spacing or pore width of lobster eye optics," *Astronomische Nachrichten*, vol. 339, no. 5, SI, pp. 363–366, Jan. 2018. DOI: `10.1002/asna.201813506`.

14. R. Hudec, "AXRO introduction and historical background," *Contributions of the Astronomical Observatory Skalnate Pleso*, vol. 48, no. 3, pp. 396–404, 2018.

15. R. Hudec and K. Remisova, "Biomimetics and astronomical X-ray optics," *Contributions of the Astronomical Observatory Skalnate Pleso*, vol. 47, no. 2, pp. 67–75, 2017.

16. R. Hudec and S. Michalova, "Fish eye optics," *Contributions of the Astronomical Observatory Skalnate Pleso*, vol. 47, no. 2, pp. 94–99, 2017.

17. R. Hudec, "Astrophysical payloads for picosatellites," *Contributions of the Astronomical Observatory Skalnate Pleso*, vol. 47, no. 2, pp. 143–150, 2017.

18. V. Simon, "Perspectives of the lobster-eye telescope: the promising types of cosmic X-ray sources," *Contributions of the Astronomical Observatory Skalnate Pleso*, vol. 47, no. 2, pp. 184–191, 2017.

19. I. Vertat, R. Linhart, J. Masopust, A. Vobornik, and L. Dudacek, "Earth's thermal radiation sensors for attitude determination systems of small satellites," *Contributions of the Astronomical Observatory Skalnate Pleso*, vol. 47, no. 2, pp. 157–164, 2017.

V. Dániel, L. Pína, A. Inneman, V. Zadražil, T. Báča, M. Platkevič, V. Stehlíková, *et al.*, "Terrestrial gamma-ray flashes monitor demonstrator on CubeSat," in *SPIE Proceedings: CubeSats and NanoSats for Remote Sensing*, T. S. Pagano, Ed., SPIE, Sep. 2016. DOI: `10.1117/12.2240299`

1. A. Alanazi and J. Straub, "Engineering Methodology for Student-Driven CubeSats," *Aerospace*, vol. 6, no. 5, Jan. 2019. DOI: `10.3390/aerospace6050054`.

2. W. Furnell, A. Shenoy, E. Fox, and P. Hatfield, "First results from the LUCID-timepix spacecraft payload onboard the TechDemoSat-1 satellite in low earth orbit," *Advances in Space Research*, vol. 63, no. 5, pp. 1523–1540, Mar. 2019. DOI: `10.1016/j.asr.2018.10.045`.

3. A. Alanazi, A. B. Jones, and J. Straub, "Requirements Modeling Language and Automated Testing for CubeSats," in *2019 IEEE Autotestcon*, 2019.

4. R. Hudec, "X/EUV and UV optics for miniature cube satellites payloads," in *EUV and X-ray Optics: Synergy between Laboratory and Space VI*, vol. 11032, 2019. DOI: `10.1117/12.2525542`.

5. P. Hatfield, W. Furnell, A. Shenoy, E. Fox, R. Parker, and L. Thomas, "The LUCID-Timepix spacecraft payload and the CERN School educational programme," *Journal of Instrumentation*, vol. 13, Jan. 2018. DOI: `10.1088/1748-0221/13/10/C10004`.

6. R. Hudec, "AXRO introduction and historical background," *Contributions of the Astronomical Observatory Skalnate Pleso*, vol. 48, no. 3, pp. 396–404, 2018.

7. R. Hudec and K. Remisova, "Biomimetics and astronomical X-ray optics," *Contributions of the Astronomical Observatory Skalnate Pleso*, vol. 47, no. 2, pp. 67–75, 2017.

8. R. Hudec and S. Michalova, "Fish eye optics," *Contributions of the Astronomical Observatory Skalnate Pleso*, vol. 47, no. 2, pp. 94–99, 2017.

9. R. Hudec, "Astrophysical payloads for picosatellites," *Contributions of the Astronomical Observatory Skalnate Pleso*, vol. 47, no. 2, pp. 143–150, 2017.

M. Urban, O. Nentvich, V. Stehlikova, T. Baca, V. Daniel, and R. Hudec, "VZLUSAT-1: Nanosatellite with miniature lobster eye X-ray telescope and qualification of the radiation shielding composite for space application," *Acta Astronautica*, vol. 140, pp. 96–104, Nov. 2017. DOI: `10.1016/j.actaastro.2017.08.004`

1. V. V. Lider, "Grazing-Incidence Focusing Optics for X-ray Telescopes (Review)," *Instruments and Experimental Techniques*, vol. 65, no. 2, pp. 191–217, Jan. 2022. DOI: `10.1134/S002044122202004X`.

2. D. Panek, T. Orosz, P. Karban, D. C. D. Gnawa, and H. K. Neghab, "Performance Comparison of Quantized Control Synthesis Methods of Antenna Arrays," *Electronics*, vol. 11, no. 7, Jan. 2022. DOI: `10.3390/electronics11070994`.

3. M. May, G. D. Rupakula, and P. Matura, "Non-polymer-matrix composite materials for space applications," *Composites Part C: Open Access*, vol. 3, Jan. 2020. DOI: `10.1016/j.jcomc.2020.100057`.

4. J. J. Lopez-Salamanca, L. O. Seman, M. D. Berejuck, and E. A. Bezerra, "Finite-State Markov Chains Channel Model for CubeSats Communication Uplink," *IEEE Transactions on Aerospace and Electronic Systems*, vol. 56, no. 1, pp. 142–154, Jan. 2020. DOI: `10.1109/TAES.2019.2911769`.

5. R. Filgas, M. Malich, T. Kuwahara, J. Broulim, M. Holik, M. Sakal, Y. Murata, *et al.*, "RISEPix-A Timepix-based radiation monitor telescope onboard the RISESAT satellite," *Astronomische Nachrichten*, vol. 340, no. 7, SI, pp. 674–680, Jan. 2019. DOI: `10.1002/asna.201913674`.

6. W. Furnell, A. Shenoy, E. Fox, and P. Hatfield, "First results from the LUCID-Timepix spacecraft payload onboard the TechDemoSat-1 satellite in Low Earth Orbit," *Advances in Space Research*, vol. 63, no. 5, pp. 1523–1540, Jan. 2019. DOI: `10.1016/j.asr.2018.10.045`.

7. P. Hatfield, W. Furnell, A. Shenoy, E. Fox, R. Parker, and L. Thomas, "The LUCID-Timepix spacecraft payload and the CERN School educational programme," *Journal of Instrumentation*, vol. 13, Jan. 2018. DOI: `10.1088/1748-0221/13/10/C10004`.

8. R. Filgas, "Space radiation monitoring with Timepix," *Astronomische Nachrichten*, vol. 339, no. 5, SI, pp. 386–390, Jan. 2018. DOI: 10.1002/asna.201813511.

> V. Dániel, A. Inneman, L. Pína, V. Zadražil, T. Báča, V. Stehlíková, O. Nentvich, *et al.*, "X-ray Lobster Eye all-sky monitor for rocket experiment," in *SPIE Proceedings: EUV and X-Ray Optics: Synergy between Laboratory and Space V*, R. Hudec and L. Pina, Eds., SPIE, May 2017. DOI: 10.1117/12.2277515

1. M. Ouyang, X. Zhao, W. He, L. Yang, Y. Hu, Y. Han, S. Ma, *et al.*, "Structural design method of the meridional lobster-eye lens with optimal efficiency," *Applied Optics*, vol. 58, no. 33, pp. 9033–9038, Jan. 2019. DOI: 10.1364/AO.58.009033.

2. R. Filgas, M. Malich, T. Kuwahara, J. Broulim, M. Holik, M. Sakal, Y. Murata, *et al.*, "RISEPix-A Timepix-based radiation monitor telescope onboard the RISESAT satellite," *Astronomische Nachrichten*, vol. 340, no. 7, SI, pp. 674–680, Jan. 2019. DOI: 10.1002/asna.201913674.

3. R. Filgas, "Space radiation monitoring with Timepix," *Astronomische Nachrichten*, vol. 339, no. 5, SI, pp. 386–390, Jan. 2018. DOI: 10.1002/asna.201813511.

4. R. Hudec, "Low-dispersion spectroscopy with cubesats and photographic plates," *Astronomische Nachrichten*, vol. 339, no. 5, SI, pp. 416–419, Jan. 2018. DOI: 10.1002/asna.201813517.

5. R. Hudec, "AXRO introduction and historical background," *Contributions of the Astronomical Observatory Skalnate Pleso*, vol. 48, no. 3, pp. 396–404, 2018.

6. R. Hudec, "Astrophysical payloads for picosatellites," *Contributions of the Astronomical Observatory Skalnate Pleso*, vol. 47, no. 2, pp. 143–150, 2017.

> R. Hudec, L. Pina, V. Marsikova, O. Nentvich, **M. Urban**, and A. Inneman, "Kirkpatrick Baez X-ray optics for astrophysics: Recent status," *Contributions of the Astronomical Observatory Skalnate Pleso*, vol. 48, pp. 437–445, 3 2018, ISSN: 1335-1842

1. V. V. Lider, "Grazing-Incidence Focusing Optics for X-ray Telescopes (Review)," *Instruments and Experimental Techniques*, vol. 65, no. 2, pp. 191–217, Jan. 2022. DOI: 10.1134/S002044122202004X.

2. S. Rukdee, V. Burwitz, G. Hartner, T. Mueller, T. Schmidt, A. Langmeier, and M. Bradshaw, "X-ray Ray Tracing with Zemax for the PANTER testing facility," in *Optics for EUV, X-ray, and Gamma-Ray Astronomy X*, vol. 11822, 2021. DOI: 10.1117/12.2595711.

3. J. Shen, N. An, W. Zhang, X. Du, and Q. Wang, "Monochromatic Kirkpatrick-Baez microscope using two spherically bent crystals," in *International Conference on Optoelectronic and Microelectronic Technology and Application*, vol. 11617, 2020. DOI: 10.1117/12.2584587.

4. V. V. Lider, "Kirkpatrick-Baez and Wolter X-ray Focusing Optics (Review)," *Journal of Surface Investigation*, vol. 13, no. 4, pp. 670–682, Jan. 2019. DOI: 10.1134/S102745101904027X.

5. D. Longcope, L. Acton, and C. Kankelborg, "Practical, corrected Kirkpatrick-Baez telescope for X-ray astronomy," *Applied Optics*, vol. 58, no. 18, pp. 4969–4980, Jan. 2019. DOI: `10.1364/AO.58.004969`.

6. V. Burwitz, R. Willingale, G. Pareschi, R. Hudec, D. Spiga, C. Pelliciari, V. Tichy, *et al.*, "AHEAD Joint Research Activity on X-ray optics," in *Space Telescopes and Instrumentation 2018: Ultraviolet to Gamma Ray*, vol. 10699, 2018. DOI: `10.1117/12.2314109`.

M. Urban, O. Nentvich, V. Stehlikova, and L. Sieger, "Uncooled spectrometer for X-ray astrophysics," in *SPIE Proceedings: EUV and X-Ray Optics: Synergy between Laboratory and Space V*, R. Hudec and L. Pina, Eds., SPIE, May 2017. DOI: `10.1117/12.2265744`

1. R. Hudec, "AXRO introduction and historical background," *Contributions of the Astronomical Observatory Skalnate Pleso*, vol. 48, no. 3, pp. 396–404, 2018.

2. R. Hudec and K. Remisova, "Biomimetics and astronomical X-ray optics," *Contributions of the Astronomical Observatory Skalnate Pleso*, vol. 47, no. 2, pp. 67–75, 2017.

3. R. Hudec and S. Michalova, "Fish eye optics," *Contributions of the Astronomical Observatory Skalnate Pleso*, vol. 47, no. 2, pp. 94–99, 2017.

4. R. Hudec, "Astrophysical payloads for picosatellites," *Contributions of the Astronomical Observatory Skalnate Pleso*, vol. 47, no. 2, pp. 143–150, 2017.

5. R. Hudec and T. Doehring, "JEUMICO: Czech-Bavarian astronomical X-ray optics project," *Contributions of the Astronomical Observatory Skalnate Pleso*, vol. 47, no. 2, pp. 170–177, 2017.

V. Stehlikova, **M. Urban**, O. Nentvich, V. Daniel, L. Sieger, and J. Tutt, "Hard X-ray Vela supernova observation on rocket experiment WRX-R," *Contributions of the Astronomical Observatory Skalnate Pleso*, vol. 47, pp. 165–169, 2 2017, ISSN: 1335-1842

1. M. Ouyang, Y. Fu, J. Zhou, W. He, L. Yang, Y. Han, and C. Wang, "Comprehensive understanding of the focal property of lobster-eye optics," *Applied Optics*, vol. 59, no. 14, pp. 4263–4270, Jan. 2020. DOI: `10.1364/AO.390101`.

2. R. Hudec, L. Amati, F. Frontera, E. Bozzo, P. T. O'Brien, D. Goetz, and V. Simon, "ESA THESEUS and Czech participation," *Astronomische Nachrichten*, vol. 341, no. 3, pp. 348–355, Jan. 2020. DOI: `10.1002/asna.202013787`.

3. T. Baca, D. Turecek, R. McEntaffer, and R. Filgas, "Rospix: modular software tool for automated data acquisitions of Timepix detectors on Robot Operating System," *Journal of Instrumentation*, vol. 13, Jan. 2018. DOI: `10.1088/1748-0221/13/11/C11008`.

4. R. Hudec, "AXRO introduction and historical background," *Contributions of the Astronomical Observatory Skalnate Pleso*, vol. 48, no. 3, pp. 396–404, 2018.

5. I. Vertat and P. Fiala, "Compensation of Industrial CMOS Camera and Image Enhancement for Sounding Rocket Astrophysical Experiments," in *2018 23rd International Conference on Applied Electronics (AE)*, 2018, pp. 149–153.

V. Daniel, **M. Urban**, O. Nentvich, and V. Stehlikova, "VZLUSAT-1: verification of new materials and technologies for space," in *SPIE Proceedings: CubeSats and NanoSats for Remote Sensing*, T. S. Pagano, Ed., SPIE, Sep. 2016. DOI: `10.1117/12.2244035`

1. R. Hudec, "AXRO introduction and historical background," *Contributions of the Astronomical Observatory Skalnate Pleso*, vol. 48, no. 3, pp. 396–404, 2018.

2. I. Vertat, R. Llnhart, M. Pokorny, J. Masopust, P. Fiala, and J. Mraz, "Small Satellite Ground Station in Pilsen - Experiences with VZLUSAT-1 Commanding and Future Modifications Toward Open Reference Ground Station Solution," in *2018 28th International Conference Radioelektronika (radioelektronika)*, 2018.

3. R. Hudec, "Astrophysical payloads for picosatellites," *Contributions of the Astronomical Observatory Skalnate Pleso*, vol. 47, no. 2, pp. 143–150, 2017.

4. I. Vertat, R. Linhart, L. Dudacek, V. Daniel, and P. Svoboda, "Autonomous and Semi-autonomous Radio Commanding of VZLUSAT-1 Nanosatellite from Ground Control Station in Pilsen," in *2017 International Conference on Applied Electronics (AE)*, 2017, pp. 263–268. DOI: `10.23919/AE.2017.8053627`.

V. Daniel, A. Inneman, I. Vertat, T. Baca, O. Nentvich, **M. Urban**, V. Stehlikova, *et al.*, "In-Orbit Commissioning of Czech Nanosatellite VZLUSAT-1 for the QB50 Mission with a Demonstrator of a Miniaturised Lobster-Eye X-Ray Telescope and Radiation Shielding Composite Materials," *Space Science Reviews*, vol. 215, no. 5, Jul. 2019. DOI: `10.1007/s11214-019-0589-7`

1. J. Chen, L. Liu, W. Xu, X. Huang, and H. Sheng, "Design and Analysis of a Hollow Metallic Microlattice Active Cooling System for Microsatellites," *Nanomaterials*, vol. 12, no. 9, Jan. 2022. DOI: `10.3390/nano12091485`.

2. E. Banken, V. E. Schneider, M. K. Ben-Larbi, L. Pambaguian, and J. Oeffner, "Biomimetic space debris removal: conceptual design of bio-inspired active debris removal scenarios," *Ceas Space Journal*, vol. 15, no. 1, SI, pp. 237–252, Jan. 2023. DOI: `10.1007/s12567-022-00438-z`.

3. M. M. Hassan and G. M. Rather, "Innovative relay selection and optimize power allocation for free space optical communication," *Optical and Quantum Electronics*, vol. 53, no. 12, Jan. 2021. DOI: `10.1007/s11082-021-03313-z`.

4. A. Kear and S. L. Folkes, "A Solution to the Hyper Complex, Cross Domain Reality of Artificial Intelligence: the Hierarchy of Ai," *International Journal of Advanced Computer Science and Applications*, vol. 11, no. 3, pp. 49–59, Jan. 2020.

V. Stehlikova, **M. Urban**, O. Nentvich, A. Inneman, T. Döhring, and A.-C. Probst, "Study of lobster eye optics with iridium coated X-ray mirrors for a rocket experiment," in *SPIE Proceedings: EUV and X-Ray Optics: Synergy between Laboratory and Space V*, R. Hudec and L. Pina, Eds., SPIE, May 2017. DOI: 10.1117/12.2265769

1. T. Baca, M. Jilek, P. Manek, P. Stibinger, V. Linhart, J. Jakubek, and M. Saska, "Timepix Radiation Detector for Autonomous Radiation Localization and Mapping by Micro Unmanned Vehicles," in *2019 IEEE/RSJ International Conference on Intelligent Robots and Systems (IROS)*, 2019, pp. 1129–1136.

2. M. Holynska, A. Tighe, and C. Semprimoschnig, "Coatings and Thin Films for Spacecraft Thermo-Optical and Related Functional Applications," *Advanced Materials Interfaces*, vol. 5, no. 11, Jan. 2018. DOI: 10.1002/admi.201701644.

3. R. Hudec, "AXRO introduction and historical background," *Contributions of the Astronomical Observatory Skalnate Pleso*, vol. 48, no. 3, pp. 396–404, 2018.

4. I. Vertat and P. Fiala, "Compensation of Industrial CMOS Camera and Image Enhancement for Sounding Rocket Astrophysical Experiments," in *2018 23rd International Conference on Applied Electronics (AE)*, 2018, pp. 149–153.

M. Urban and D. Doubravová, "Timepix3: Temperature influence on X-ray measurements in counting mode with Si sensor," *Radiation Measurements*, vol. 141, p. 106 535, Feb. 2021. DOI: 10.1016/j.radmeas.2021.106535

1. D. Jannis, C. Hofer, C. Gao, X. Xie, A. Beche, T. J. Pennycook, and J. Verbeeck, "Event driven 4D STEM acquisition with a Timepix3 detector: Microsecond dwell time and faster scans for high precision and low dose applications," *Ultramicroscopy*, vol. 233, Jan. 2022. DOI: 10.1016/j.ultramic.2021.113423.

2. C. Leroy, C. Papadatos, M. Usman, and M. Boussa, "Temperature effects on clustering in TPX3-Si pixel detectors," *Journal of Instrumentation*, vol. 16, no. 9, Jan. 2021. DOI: 10.1088/1748-0221/16/09/P09007.

M. Urban, O. Nentvich, T. Báča, I. Veřtát, V. Maršíková, D. Doubravová, V. Dániel, *et al.*, "REX: X-ray experiment on the water recovery rockets," *Acta Astronautica*, vol. 184, pp. 1–10, Jul. 2021. DOI: 10.1016/j.actaastro.2021.03.019

1. V. Simon and R. Hudec, "Perspectives of the LOBSTER-EYE monitor in the soft X-ray observing the Galactic center region," *Journal of High Energy Astrophysics*, vol. 35, pp. 69–76, Jan. 2022. DOI: 10.1016/j.jheap.2022.06.001.

R. Hudec, L. Pina, V. Marsikova, O. Nentvich, **M. Urban**, and A. Inneman, "Lobster Eye X-ray optics for astrophysics: Recent status," *Contributions of the Astronomical Observatory Skalnate Pleso*, vol. 48, pp. 456–465, 3 2018, ISSN: 1335-1842

1. V. V. Lider, "Grazing-Incidence Focusing Optics for X-ray Telescopes (Review)," *Instruments and Experimental Techniques*, vol. 65, no. 2, pp. 191–217, Jan. 2022. DOI: `10.1134/S002044122202004X`.

V. Stehlikova, **M. Urban**, O. Nentvich, and L. Sieger, "Radiation resistance monitor on VZLUSAT-1: Preliminary results," *Astronomische Nachrichten*, vol. 339, no. 5, pp. 382–385, Jun. 2018. DOI: `10.1002/asna.201813510`

1. T. Blachowicz and A. Ehrmann, "Shielding of Cosmic Radiation by Fibrous Materials," *Fibers*, vol. 9, no. 10, Jan. 2021. DOI: `10.3390/fib9100060`.

T. Baca, M. Jilek, I. Vertat, **M. Urban**, O. Nentvich, R. Filgas, C. Granja, *et al.*, "Timepix in LEO Orbit onboard the VZLUSAT-1 Nanosatellite: 1-year of Space Radiation Dosimetry Measurements," *Journal of Instrumentation*, vol. 13, no. 11, pp. C11010–C11010, Nov. 2018. DOI: `10.1088/1748-0221/13/11/c11010`

1. R. Hudec, "X/EUV and UV optics for miniature cube satellites payloads," in *EUV and X-ray Optics: Synergy between Laboratory and Space VI*, vol. 11032, 2019. DOI: `10.1117/12.2525542`.

L. Pina, R. Hudec, A. Inneman, O. Nentvich, **M. Urban**, V. Marsikova, V. Stehlikova, *et al.*, "Multi-Foil X-ray optics tests at PANTER: Preliminary results," *Contributions of the Astronomical Observatory Skalnate Pleso*, vol. 48, pp. 466–475, 3 2018, ISSN: 1335-1842

1. M. Ouyang, Y. Fu, J. Zhou, W. He, L. Yang, Y. Han, and C. Wang, "Comprehensive understanding of the focal property of lobster-eye optics," *Applied Optics*, vol. 59, no. 14, pp. 4263–4270, Jan. 2020. DOI: `10.1364/AO.390101`.

O. Nentvich, **M. Urban**, M. Blažek, A. Inneman, R. Hudec, and L. Sieger, "Lobster eye optics: position determination based on 1D optics with simple code mask," in *SPIE Proceedings: Advances in X-Ray/EUV Optics and Components XIV*, C. Morawe, A. M. Khounsary, and S. Goto, Eds., SPIE, Sep. 2019. DOI: `10.1117/12.2528505`

1. A. Kear and S. L. Folkes, "A Solution to the Hyper Complex, Cross Domain Reality of Artificial Intelligence: the Hierarchy of Ai," *International Journal of Advanced Computer Science and Applications*, vol. 11, no. 3, pp. 49–59, Jan. 2020.

L. Mikulickova, L. Pina, A. Inneman, D. Doubravova, V. Marsikova, L. Sieger, **M. Urban**, *et al.*, "Optimization of microroughness of replicated X-ray optics," in *SPIE Proceedings: EUV and X-Ray Optics: Synergy between Laboratory and Space V*, R. Hudec and L. Pina, Eds., SPIE, May 2017. DOI: `10.1117/12.2265810`

1. M. Holynska, A. Tighe, and C. Semprimoschnig, "Coatings and Thin Films for Spacecraft Thermo-Optical and Related Functional Applications," *Advanced Materials Interfaces*, vol. 5, no. 11, Jan. 2018. DOI: `10.1002/admi.201701644`.